Wing deformation measurements of the DelFly II in different flight conditions

Dorian N.W.M. Heitzig

Wing deformation measurements of the DelFly II in different flight conditions

by

Dorian N.W.M. Heitzig

to obtain the degree of Master of Science
at the Delft University of Technology,
to be defended publicly on Friday August 30, 2019 at 9:15.

Student number: 4633725
Project duration: August 1, 2018 – August 30, 2019
Thesis committee: Dr. ir. Bas W. van Oudheusden,   TU Delft, supervisor and chair
                    Dr. ir. Roeland de Breuker,   TU Delft
                    Ir. Christophe de Wagter,   TU Delft
                    M.Sc. Diana Olejnik,   TU Delft, supervisor

An electronic version of this thesis is available at `http://repository.tudelft.nl/`.

Acknowledgements

This thesis would not have been possible without the guidance and support of many different people.

I want to thank my supervisors for the countless hours guiding my project over the last year. Bas, you were a large help with the scientific approach and gave me great confidence in my work. Diana, thanks for being always available and allowing me to work on this minuscule detail while knowing so little about the general working. Matej, thank you for always thinking one step ahead.

All the people working around me on their theses also deserve a big thank you. By distance, this are Jan, Francesco, Maria, Carlos, Lucas, Niels, Jaime, Mart and Jorge, as well as many others. You were a great company during all this time, always up to for a joke keeping my spirits high and were a great incentive to strive for the highest quality of work. Also, I want to thank Roberto, Blanca, Victor, Kevin and Stelios for accompanying me during my master studies.

Of course, my family at home was always a huge support. Thanks for allowing me to focus so much on my studies.

Dorian N.W.M. Heitzig
Delft, August 2019

Abstract

This study investigates the wing deformation of the flapping-wing micro air vehicle (MAV) DelFly II in various flight conditions.

Experiments were carried out with the MAV tethered in a windtunnel test section. To determine the best suited measurement approach, a trade-off study was carried out which showed that a point tracking approach with background illumination is most suitable. The therefore used high-speed camera pair and illumination were mounted on the same rotating frame with the DelFly, which allowed adequate viewing axes of the wings at for all pitch angles. Processing was done a purpose-build algorithm, allowing 136 points per wing to be measured simultaneously with an average lost point ratio of 3.4 % and an estimated accuracy of 0.25 mm.

Results of hovering flight show some previously unnoticed behaviors. First, it was noted that the upper and lower wing on each side do not deform purely symmetric but show some considerable asymmetric behavior like heave and camber production. Furthermore, the upper wing shows a torsional wave and recoil behavior at faster flapping frequencies, which was shown to be beneficial in insect flight. Lastly, it was found that an air-buffer remains present between the wing surfaces at all times of the clap-and-peel motion (apart from the root trailing edge).

This air-buffer increases once freestream velocity is added, which is investigated during the climbing flight study. Here, the reduced angle of attack of the wing is assumed to reduce the wing loading at faster climb, resulting in lower deformations outside the clap-and-peel motion.

The isolated effect of a body pitch angle is also studied. Here, the asymmetrical freestream direction results in larger asymmetries such as wing alignment with the freestream direction and reduced camber and even camber reversal during the upstroke.

In forward flight the pitch angle is changed simultaneously with the flapping frequency and freestream velocity. Due to the non-linear properties the wing deforms not directly as a superposition of the individual effects. Deviations are mostly present in increased asymmetry in incidence angle, while the camber behaves more linear and the clap-and-peel motion also remains relatively unchanged. The torsional wave and recoil are here however reduced.

Descending flight was also tested. Velocities below $1\,\mathrm{m\,s^{-1}}$ result in relatively minor deformation changes, while faster descent leads to large flapping frequency fluctuations, making interpretation of the results impossible.

Contents

Nomenclature

Symbols of result section are leading, symbols of the literature review section may be incomplete as uses may be different.

Latin symbols

a	Flapping amplitude	[m]
c_{mean}	Mean chord	[m]
f	Flapping frequency	[Hz]
$f\#$	f-number, ratio of focal length to aperture diameter	[-]
g	Gravitational acceleration	[m s^{-2}]
it	Point number	$-$
it	Timestep	$-$
k	Reduced frequency	[-]
q	Dynamic pressure	[N m^{-2}]
R	Specific gas constant	[J kg^{-1} K^{-1}]
r_w	Spanwise location measured from wing root	[m]
r_{tip}	Spanwise tip location or half span	[m]
Re	Reynolds number	[-]
St	Struohal number	[-]
T	Temperature	[K]
t	Time	[s]
t^*	Non-dimensionalized time or phase	[-]
T_f	Flapping period	[s]
U_∞	Freestream velocity	[m s^{-1}]
$U_{\infty,z}$	Freestream velocity component in z_b direction	[m s^{-1}]
U_{LE}	Leading edge velocity	[m s^{-1}]
U_{tot}	Combined inflow velocity	[m s^{-1}]
x, y, z	Position in 3D space	[m]
x_b, y_b, z_b	Position in body coordinate system	[m]
x_w, y_w, z_w	Position in local wing coordinate system	[m]
$x_{d,r}, y_{d,r}, z_{d,r}$	Position in right wing dihedral coordinate system	[m]

Greek symbols

α	Angle of attack	[°]
$\ddot{\phi}$	Stroke angle acceleration	[° s^{-2}]

ϕ	Stroke angle	[°]
ρ	Air density	[$\mathrm{kg\,m^{-3}}$]
θ_b	Body pitch angle	[°]
θ_w	Local wing incidence angle	[°]
ε	Camber ratio	[-]

Acronyms

2D	Two-dimensional
3D	Three-dimensional
CHT	Circular Hough Transform
CMOS	Complementary Metal Oxide Semiconductor
DHI	Digital Holographic Interference
DIC	Digital Image Correlation
DLT	Direct Linear Transformation
DMD	Digital Micromirror Device
DOF	Degrees-of-freedom
FPP	Fringe Pattern Projector
FTP	Fourier Transform Profilometry
LED	Light Emitting Diode
LEV	Leading Edge Vortex
MAV	Micro Air Vehicle
MFTP	Modified Fourier Transform Profilometry
MPE	Mean Pixel Error
PCF	Projected Comb Fringe
PIV	Particle Image Velocimetry
PROPAC	Projected Pattern Correlation Technique
RBF	Radial Basis Function
s.d.	Standard deviation
TOF	Time-of-Flight

List of Figures

List of Tables

Introduction

Recent years show an increasing interest and need for micro air vehicles (MAV) for various new fields of applications. While current commercial solutions typically use modifications of well known, conventional airplane and helicopter configurations, research done over the past decades on flight and propulsion mechanisms in biology show great efficiency of the natural flapping-wing mechanisms for very low flight speeds or hover. Compared to the conventional configurations, their maximum effectiveness and efficiency is not as affected by the low Reynolds number regime. Especially hovering insects, which commonly make use of dynamic effects such as leading edge vortices (LEV), are able create lift coefficients similar to those otherwise only achievable in higher Reynolds numbers [36].

A propulsion mechanism which shows to be especially efficient is the 'clap-and-fling' mechanism illustrated in Figure 1.1, first described for the wasp encarsia formosa by Weis-Fogh [52]. Here, the left and right wing leading edge make contact at the end of the instroke (B), then the entire wing surfaces 'clap' together and become parallel (C) and lastly rigidly rotate apart around the trailing edge and 'fling' apart (E). During the opening a LEV is created between the wings and once the wings loose contact an air-jet between the wings resulting in additional thrust production. Later research showed that many other insects also use this motion, however deform thereby in chordwise direction and 'peel' apart [17].
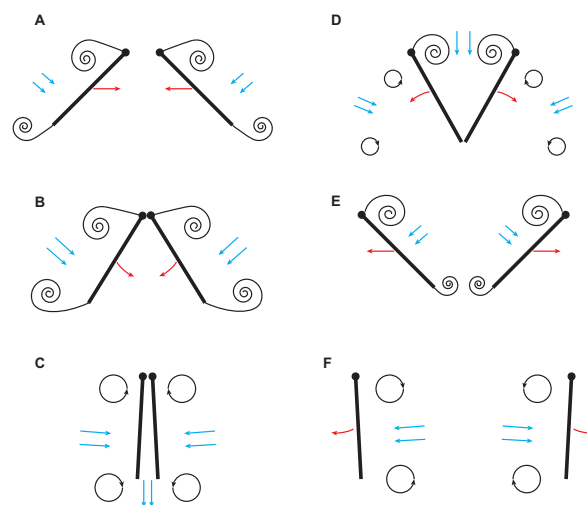
Figure 1.1: Rigid 'clap-and-fling' motion. [36]

1.1. Importance of wing deformation in flapping-wing flight

Wing flexibility does not only play a central role during this process, but directly impacts the creation of all aerodynamic forces due to flow accelerations and creation of pressure differentials, while also defining the orientations in which these forces act. It was shown that the deformations typically result in increased efficiency and larger operating ranges compared to rigid wings [20, 42, 50]. Figure 1.2 shows this on the example of the dragonfly, which would have 35 % reduced lift power economy if the wings were fully rigid [60]. A clear description of the wing deformation is therefore essential in any study of flapping-wing flight and will improve the understanding of the occurring phenomena that result in such high efficiency and effectiveness.
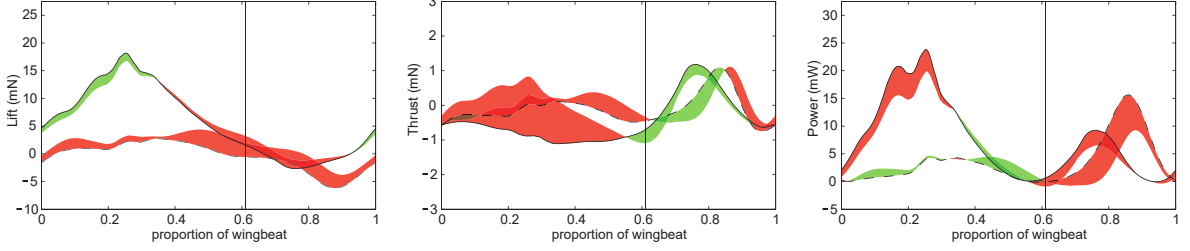
Figure 1.2: Lift, thrust and aerodynamic power values of rigid dragonfly wings, solid and dashed lines denote the hind-, and forewing, respectively. Red shading indicates inferior performance of the rigid wing compared to the actual deforming wing, green shading indicates better performance. [60]

The wing deformation results from the interaction of aerodynamic and structural (i.e. inertial and elastic) forces acting on the wing. These form a force equilibrium, a simplified form shown in vector notation in Equation 1.1.

$$\underbrace{\mathbf{K}\ \mathbf{x}}_{\text{Elastic forces}} + \underbrace{\mathbf{I}\ \ddot{\mathbf{x}}}_{\text{Inertial forces}} + \underbrace{\mathbf{L}}_{\text{Aerodynamic forces}} = \mathbf{0}. \tag{1.1}$$

Assuming an linear elastic model, the structural forces are the product of wing deformation, $\mathbf{x}$ and wing stiffness, $\mathbf{K}$. The typical wing construction of flapping wing flight allows large deformations as the wings are usually light and flexible. Due to the large deformations and specific stiffness, the elastic forces typically show non-linear behavior, making their influence more difficult to model. Often, elastic forces are for instance released towards a stroke end as other forces are reducing, leading to extended rotation of the wing trailing edge [37].

Inertial forces are the product of the wing acceleration, $\ddot{\mathbf{x}}$ and wing inertia, $\mathbf{I}$. The most prominent effect is typically a phase lag of the wing surface motion compared to the that of leading edge, which results in large incidence angles of the wings [17]. In some cases this can result in more complicated behavior such as a recoil effect after stroke reversal which benefits the thrust production [48].

Aerodynamic forces, $\mathbf{L}$ result due to various effects, for instance the airfoil orientation, but also its velocity or acceleration, e.g. induced by wing heaving or rotation. Furthermore, non-linear effects such as LEV production are present in flapping wing flight. To a large extent aerodynamic forces are resultant from the wing stroke velocity. As this is the first derivative of the location, the produced forces typically act as damping, and are phase shifted compared to the structural forces [37]. Structural damping may also influence the force equilibrium, however is typically low compared to aerodynamic effects and often neglected.

How these interactions affect the wing deformation has been relatively well researched for hovering flight [9, 11, 22, 58]. This includes for instance different studies on the wing-fluid mass ratio

which affects the ratio of inertial and aerodynamic forces [10, 36, 56], wing stiffness [16, 43] and also the effect of wing-wing interactions [37].

Relatively little research has however been done on the influence of different flow conditions on the wing deformation, where most have studied the wings in stationary ambient conditions with zero freestream velocity. Most of the tests considering states other than hover have been conducted for insects [13, 47, 50], which does however not allow free variation of flow and flapping parameters.

The introduction of a freestream velocity thereby plays a large role on the produced aerodynamic forces and flow structures and will therefore also have a coupled effect on the deformation, where unsteady effects are reduced with increasing flow velocity [36]. In forward flight the flapping motion is thereby not aligned normal to the freestream velocity, which implies that asymmetric net forces are produced, and the wings are no longer symmetrically loaded, thus deformations are asymmetric. Research on single wing fliers generally finds that the downstroke (the stroke direction that has a downwards component) is stronger loaded due to the stroking motion against the freestream velocity. The downstroke thereby generates mostly lift, while the upstroke generates some amount of thrust [50], the specific amount and orientation being dependent on the and wing shape and path [20].

1.2. The DelFly II

An interesting aspect is especially the effect of different flow conditions on the Delfly, including the clap-and-peel motion. Primarily, this motion is beneficial at hover or low flight speeds, while becoming less relevant at higher velocities [36]. The deformation of the clap-and-peel motion in such flight condition is until now only briefly studied in literature by Nakata et al. [34].

Therefore, this study will focus on the DelFly, which is a family of four- or X-wing flapping-wing MAV exhibiting the 'clap-and-peel' motion between the wing-pairs on each side. The DelFly II, shown in Figure 1.3 and henceforth simply called DelFly, is the variant which aerodynamics have been most extensively researched and it will also be used in this study.
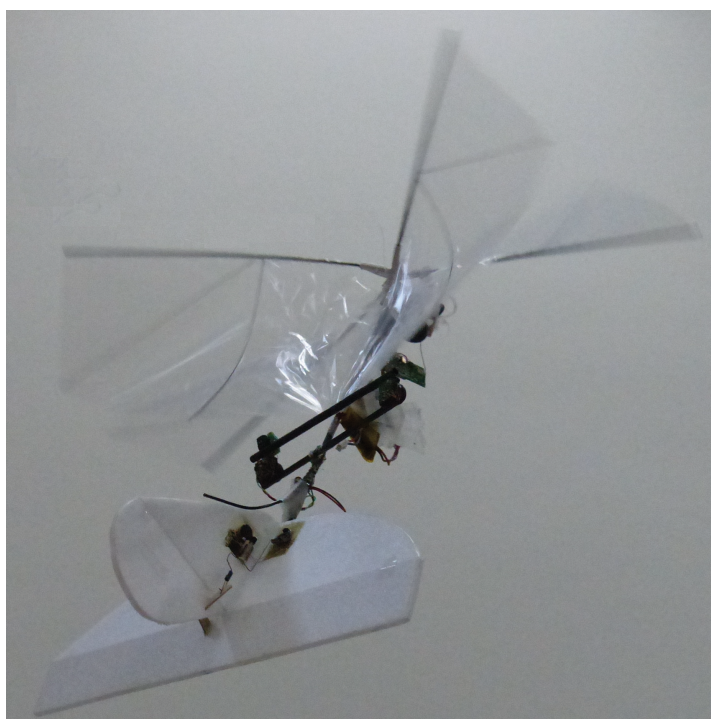
Figure 1.3: The DelFly II in forward flight performing a peeling motion. [36]

Until now, detailed measurements of the DelFly wing deformation are available only for hovering flight. Here, the wing deformation shall be investigated in different flight conditions with changing flow conditions. This fills a large knowledge gap and allows to gain a better understanding of the occurring phenomena in the flight of the DelFly and flapping-wing fliers in general, especially the changing influence of the wing-wing interactions in faster and asymmetric flow conditions.

1.3. Methodology

The assumption of purely symmetric loading previously allowed to measure only one of wing and assume a mirrored motion of the other. As now considerable asymmetry is introduced this will no longer be the case, therefore now both wings must be measured. While theoretically the previous measurement setup could simply be used to measure upper and lower wings separately, it is likely to introduce considerable error during synchronizing and aligning the measurement data, and due to changing measurement conditions between recordings. Therefore, it is desired to find and adapt a measurement setup which allows measurement of both surfaces, while being of limited complexity.

Optical methods using camera sensors lend themselves well to such applications. Methods used in wing deformation studies typically track discrete points or continuous patterns applied to the wings, or asses the distortion of light structures in the form of random patterns or fringes. The choice of method is here restricted due to the close proximity of the wings, which limits the optical accessibility. Furthermore, the structural properties of the lightweight wings shall not be changed considerably, as this introduces uncertainties when comparing results to those of other experiments. This limits the choice of measurement technique and limits the straightforward use of previously applied methods. Fixing the measured object relative to the cameras is furthermore advisable as it reduces variability between measurements and limits the complexity of the measurement procedure. Therefore, the DelFly will be tethered in a windtunnel test section and different free-flight condition will be modeled using previously obtained settings of freestream and flapping frequency.

Studying these complex deformations using numerical simulations is for now unfeasible. The strong coupling of fluid and structure interactions has until now only been solved for relatively simple geometries [20], while all exact flapping wings replications rely on experimental measurements of the wing shape to generate geometries used in the aerodynamic solvers [15, 34, 60]. Together with previous flow measurements of the DelFly [14, 32], measurements of wing deformations in forward flight create a complete validation case which could allow more realistic simulations and advancements of numerical solvers.

1.4. Research objective and thesis structure

Resulting from the points laid out in the previous sections the main objective of this thesis is formed to be:

> *To determine and analyze the changes in deformation of interacting flapping-wings in different flight conditions by experimental windtunnel measurements.*

Each of the following chapters solves part of this objective. First, a detailed overview of suitable measurement techniques is given within the literature review in Chapter 2. Techniques are generally classified in passive and active technique, where passive techniques monitor the object texture, while active techniques use special light sources which increase contrast and form an integral part of the measurement procedure. These are explained in Section 2.3 and 2.4, respectively, and followed

by a short conclusion section, which forms the basis to determine which techniques are suitable for the thesis objective.

This theoretical knowledge is expanded on in Chapter 3, where the measurement techniques are assessed within short preliminary studies, giving closer insight to their applicability to two wing measurements. This assessment is concluded with a trade-off study, which presents the selected measurement technique.

The final measurement technique is then discussed in more detail in Chapter 4. This includes the descriptions of the measurement setup and the processing of the acquired data. An evaluation of the performance of the measurement technique is also given.

Chapter 5 presents the results of the measurements, to fulfill the main thesis objective. Before the results of the more complex forward flight condition can be analyzed, a better understanding of the underlying phenomena must be achieved. Therefore, first a parameter study is carried out for the effects of flapping frequency (Section 5.1), inflow velocity (Section 5.2), reduced frequency (Section 5.3) and body pitch angle (Section 5.4). The flapping frequency studies thereby resemble hovering flight, which was previously studied by Perçin et al. [37]. The section therefore mostly serves as verification of the measurement method. Analogously, changing inflow velocity at zero pitch angle effectively models climbing flight. The findings of these parameter studies are then used in the investigation of forward flight, which is presented in Section 5.5. Lastly, descending flight is shortly treated in Section 5.6.

All findings of the thesis project are finally summarized in Chapter 6, together with recommendations for future work.

<div style="text-align: right; font-size: 3em;">2</div>

Review of optical shape measurement techniques

This chapter gives an overview of optical measurement techniques suitable for flapping-wing deformations. It focuses thereby on the multitude of applications to natural and robotic fliers when possible, as it allows a better understanding of the specific properties. In the following section, the early work will shortly be presented, which shows that understanding wing deformations was found to be an essential part of understanding flapping-wing flight and serves as a motivation to develop more detailed methods. The fundamental optical workings of these methods are explained in Section 2.2, which serves as a robust platform for current passive, and active techniques, shown in Section 2.3 and 2.4 respectively. In Section 2.5 all findings are collected and a short judgment of the theoretical suitability to the thesis project is given. These findings are later considered in the final measurement technique selection, presented in Section 3.

2.1. History

Jensen [25] was one of the first researchers to measure the wing movement of a tethered locust. He analyzed stroboscopic slow-motion film and determined the wing movement relative to the body and made crude estimations of the angle of attack of the wing. Furthermore, he studies a severed wing in shear flow, noting that the wing deforms and consequentially results in an increased stall angle. This shows that the significance of wing deformation was already understood, even with the limited measurement quality.

Nachtigall [33] carried out extensive measurements on flies suspended in a wind tunnel. Interesting is especially the novel lighting setup he used, shown in Figure 2.1a: Three separate light sources (L_i) illuminated the fly in the X, Y and Z axis, all directed towards separate quadrants of the imaging film using mirrors (S_i). This allowed first 3D measurements of the wing outline. Thereby it was assumed that the recorded images are parallel projections, thus perspective magnifications or distortions were neglected. The wing deformations of the studied flies was thereby found to be relatively stiff, most of the flapping cycle has only low twist deformations and no camber change could be observed. At stroke reversal the trailing edge was however found to have a second harmonic one order of magnitude faster than the flapping frequency, which showed that the measurement setup had the capability to measure high frequency phenomena in the order of 1 kHz.

At this point the missing description of perspective distortion was limiting the measurement quality significantly. Zarnack [62] was the first to consider this optical effect, making first quantitative measurements of locust wing deformations. His measurement setup used a planar two lens

<div style="text-align: center;">7</div>

camera as stereo setup which was calibrated by an early method to determine the internal orientation of the lenses. Based on the known geometry he was then able to determine the real world 3D position of a point based on the 2D position in the two images, assuming that there is no inaccuracies of the setup. He was then able to calculate the three dimensional wing geometries of a locust by manually digitizing defined wing points - mostly vein endpoints on the wing outline - through the flapping cycle using an early computer. This allowed him to calculate twist deformations mathematically.
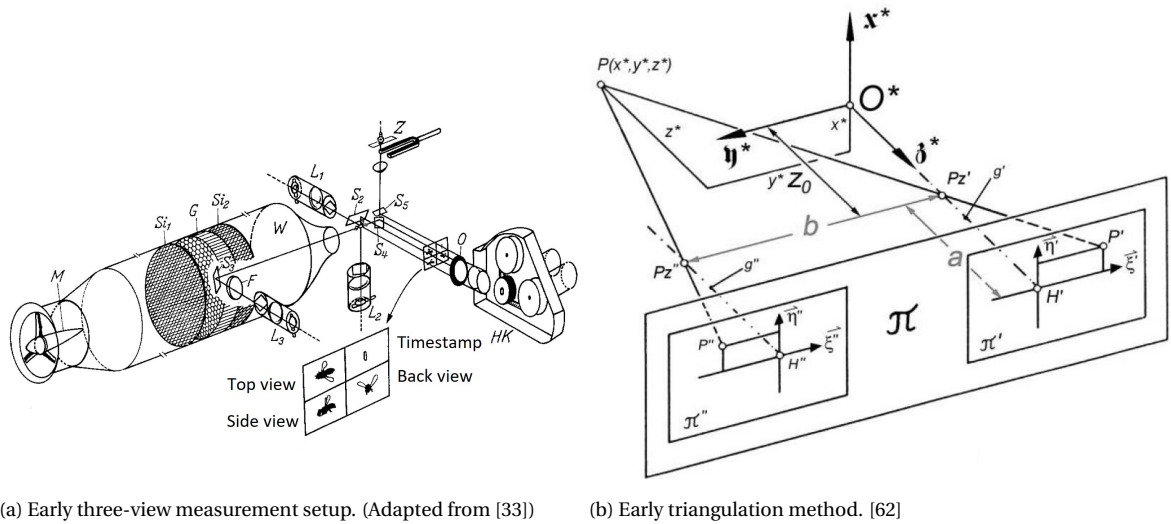
(a) Early three-view measurement setup. (Adapted from [33])   (b) Early triangulation method. [62]

Figure 2.1: Early photogrammetric measurement setups.

While giving remarkable measurement detail, the previous studies proved that a more robust framework was necessary for more extensive studies. Necessary developments for this were done in the later part of the 20th century, for instance the definition of the direct linear transformation (DLT) method by Abdel-Aziz and Karara [1], which still forms the basis of current computer vision applications. The basics of these optical models are described in Section 2.2. Furthermore, the amount of manual labor was limiting the measurement detail, often limiting studies to descriptions of the wing outline, while assuming the wing surface to remain planar. This limitation was removed with the introduction of electronic video cameras, for instance by Burner et al. [7], who were among the first do describe aircraft wing deformations.

All these improvements today allow considerably better spatial resolution with lower uncertainty while reducing the amount of manual labor. The first higher resolution application to flapping wing insects used active illumination techniques, specifically the comb fringe method explained in Section 2.4.2.

2.2. Camera Model

Having a mathematical description of a camera is essential to using it as a measuring tool. The following sections will introduce the framework and the commonly used pinhole model that describes a single camera and extend the theory to stereo or multi-view setups, necessary to measure arbitrary 3D geometries.

2.2.1. Pinhole model

The pinhole model is commonly used to describe a camera. This model reduces the lens system to a single point, called principle point, where all rays of light pass through before reaching the image sensor. To be able to describe rays of light, homogeneous coordinates are used. Instead of using a Cartesian coordinate system, where the position is described by $\mathbf{X}_{cart} = (X_{cart}, Y_{cart}, Z_{cart})^T$, any point is described by a 4-row homogeneous coordinate $\mathbf{X} = (X, Y, Z, T)^T$. The relation between them is

$$X_{cart} = \frac{Y}{T}, \quad Y_{cart} = \frac{Y}{T}, \quad Z_{cart} = \frac{Z}{T}. \tag{2.1}$$

Thus, $n\mathbf{X}$ describes the same point as $\mathbf{X}$, and all points with an identical ratio of X, Y, Z or with multiples of T are co-linear, up to the point at $(X, Y, Z, 0)^T$, which lies at infinity. It can be helpful to interpret X, Y and Z as a certain slope of a line which length relates to $1/T$.

The pinhole model is visualized in Figure 2.2, where rays reflected by world points $\mathbf{X}_i = (X_i, Y_i, Z_i, T_i)^T$ are passing through the principle point at $\mathbf{C}$ and intersect the image plane at $\mathbf{x}_i = (x_i, y_i, w_i)$.
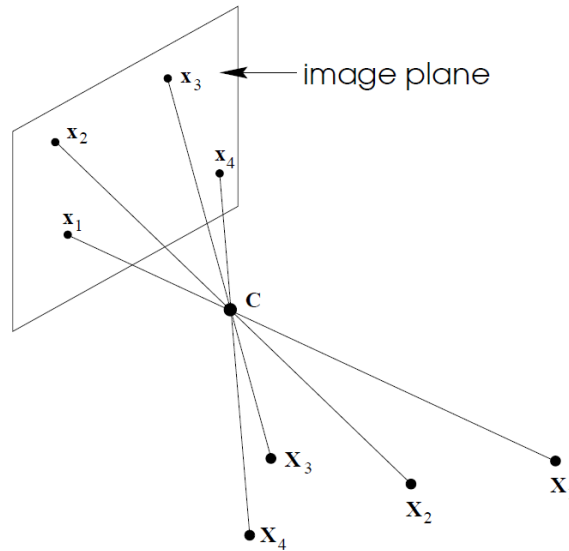
Figure 2.2: Pinhole model. [23]

This gives a relation between world points $\mathbf{X_i}$ and their projection on the image plane, $\mathbf{x'}_i$:

$$\begin{pmatrix} x_i \\ y_i \\ w_i \end{pmatrix} = \mathbf{P}_{3\times4} \begin{pmatrix} X_i \\ Y_i \\ Z_i \\ T_i \end{pmatrix}, \tag{2.2}$$

or in condensed form

$$\mathbf{x_i} = \mathbf{P}\mathbf{X}_i, \tag{2.3}$$

where $\mathbf{P}$ is known as the camera matrix. This matrix only needs to be known to scale as homogeneous coordinates are used. Thus, it has only 11 degrees-of-freedom (DOF) [23]. The matrix can be split into the intrinsic and extrinsic camera matrices, one describing the internal parameters such as pixel size, skewness and focal settings while the external matrix contains the rotation and transformation of the camera relative to the coordinate system.

2.2.2. Basic camera matrix calibration

The combined camera matrix can be determined when sufficient correspondences between image points $\mathbf{x}_i$ and world points $\mathbf{X}_i$ are known. As homogeneous coordinates are used, the left and right hand side may also be scaled solutions. Equation 2.3 can therefore be expressed as

$$\mathbf{x_i} \times \mathbf{P}\mathbf{X}_i = \mathbf{0}. \tag{2.4}$$

To calculate the cross product, $\mathbf{P}$ is split into its three rows $\mathbf{p}^{jT}$, $j = 1,...,3$:

$$\begin{pmatrix} y_i\mathbf{p}^{3T}\mathbf{X}_i - w_i\mathbf{p}^{2T}\mathbf{X}_i \\ w_i\mathbf{p}^{1T}\mathbf{X}_i - x_i\mathbf{p}^{3T}\mathbf{X}_i \\ x_i\mathbf{p}^{2T}\mathbf{X}_i - y_i\mathbf{p}^{1T}\mathbf{X}_i \end{pmatrix} = \begin{bmatrix} y_i\mathbf{p}^{3T} - w_i\mathbf{p}^{2T} \\ w_i\mathbf{p}^{1T} - x_i\mathbf{p}^{3T} \\ x_i\mathbf{p}^{2T} - y_i\mathbf{p}^{1T} \end{bmatrix} \mathbf{X}_i = \mathbf{0}. \tag{2.5}$$

As $\mathbf{p}^{jT}\mathbf{x}_i = \mathbf{x}_i^T\mathbf{p}^j$, this can be rewritten to a set of three equations:

$$\begin{bmatrix} \mathbf{0}^T & -w_i\mathbf{X}_i^T & y_i\mathbf{X}_i^T \\ w_i\mathbf{X}_i^T & \mathbf{0}^T & -x_i\mathbf{X}_i^T \\ -y_i\mathbf{X}_i^T & x_i\mathbf{X}_i^T & \mathbf{0}^T \end{bmatrix} \begin{pmatrix} \mathbf{p}^1 \\ \mathbf{p}^2 \\ \mathbf{p}^3 \end{pmatrix} = \mathbf{0}, \tag{2.6}$$

where $\mathbf{p} = (\mathbf{p}^1 T, \mathbf{p}^2 T, \mathbf{p}^3 T)^T$ is a 12-vector containing the elements of $\mathbf{P}$. The third row is thereby a linear combination of row one and two, thus from each point correspondence two equations are obtained:

$$\begin{bmatrix} \mathbf{0}^T & -w_i\mathbf{X}_i^T & y_i\mathbf{X}_i^T \\ w_i\mathbf{X}_i^T & \mathbf{0}^T & -x_i\mathbf{X}_i^T \end{bmatrix} \begin{pmatrix} \mathbf{p}^1 \\ \mathbf{p}^2 \\ \mathbf{p}^3 \end{pmatrix} = \mathbf{A}_i\mathbf{p} = \mathbf{0}, \tag{2.7}$$

As $\mathbf{P}$ and $\mathbf{p}$ have 11 DOF, 5½ point correspondences are needed. The matrix $\mathbf{A}$ is then assembled from the rows of different $\mathbf{A}_i$. This system of equations can then be solved, setting an arbitrary scale for instance as $||\mathbf{p}|| = 1$.

Point correspondences can for instance be obtained by placing a calibration plate (consisting of a known planar point grid) into the image view. The coordinate center is then defined in one of the points with the Z axis orthogonal to the grid. As the grid spacing is known, all world point locations are known. In the image the individual point grid locations can be found using the known geometries and point finding algorithms explained in Section 3.2. To calibrate an entire volume the calibration plate can be moved by known steps in Z directions. Downside is however that the calibration plate and its position is only known to a certain accuracy. This is why typically camera matrices of multiple cameras are determined simultaneously, which allows the plate to be located at an arbitrary location in space.

For either approach, some error in the point correspondence will exist. Then, $\mathbf{A}\mathbf{p} \neq \mathbf{0}$. To still obtain a reasonable solution, typically considerably more correspondences are used, and other methods are added to minimize $\mathbf{A}\mathbf{p}$.

The direct linear transformation (DLT), introduced by Abdel-Aziz and Karara [1], solves the overdetermined system using the singular value decomposition of $\mathbf{A}$, where $\mathbf{p}$ is the unit singular vector of the smallest singular value. The determined camera matrix could be further improved by least square optimization, using for instance the Levenberg-Marquardt algorithm. Both these methods are explained in detail in [23].

Lenses of typical cameras have finite lens thickness which introduces radial distortion. This holds especially for cameras with a low focal-length, which will for instance distort the image of a square into a more rounded object where each corresponding point is displaced radially. Therefore in practive the linear pinhole model are typically improved by a distortion correction originated by Brown [6].

2.2.3. Triangulation in stereo- or multi-view setups

To determine the location of a world point, multiple cameras are required. This process is based on the linear Equation 2.5, part of the DLT method earlier derived for a single view. Combining the independent parts for two cameras views with $w_i = w'_i = 1$, the following equation is obtained:

$$\begin{bmatrix} x_i\mathbf{p}^{3T} - \mathbf{p}^{1T} \\ y_i\mathbf{p}^{3T} - \mathbf{p}^{2T} \\ x'_i\mathbf{p}'^{3T} - \mathbf{p}'^{1T} \\ y'_i\mathbf{p}'^{3T} - \mathbf{p}'^{2T} \end{bmatrix} \mathbf{X}_i = \mathbf{A}_i\,\mathbf{X}_i = \mathbf{0}. \tag{2.8}$$

If more than two cameras are used, additional rows are added to $\mathbf{A}_i$. This equation is similar to Equation 2.7 and will also not hold for the typical case where $\mathbf{P}$, $\mathbf{x}_i$ or $\mathbf{x}'_i$ are determined with some error. Thus, the equation can again be solved using the singular value decomposition of the DLT method.

2.2.4. Epipolar Geometry

The epipolar geometry describes the projection of a point into two views and gives a good visual representation, see Figure 2.3. The center of the epipolar geometry is a line through the principle points of two cameras, which intersects both image planes at the epipoles $\mathbf{e}$ and $\mathbf{e}'$. A world point can now be described by an epipolar plane π through this baseline. The plane will intersect the image planes at lines $\mathbf{l}$ and $\mathbf{l}'$.

An image point $\mathbf{x}$ of the first camera can be reprojected to a ray in world coordinates and will also define an epipolar plane. The epipolar plane will be seen as line $\mathbf{l}'$ in the second image plane. Point $\mathbf{x}'$ will lie in that plane, and its position along the line also determines the position of $\mathbf{X}$, previously described mathematically in Equation 2.8.

(a) Baseline, epipol, epipolar planes and lines.   (b) Triangulation using epipolar geometry.
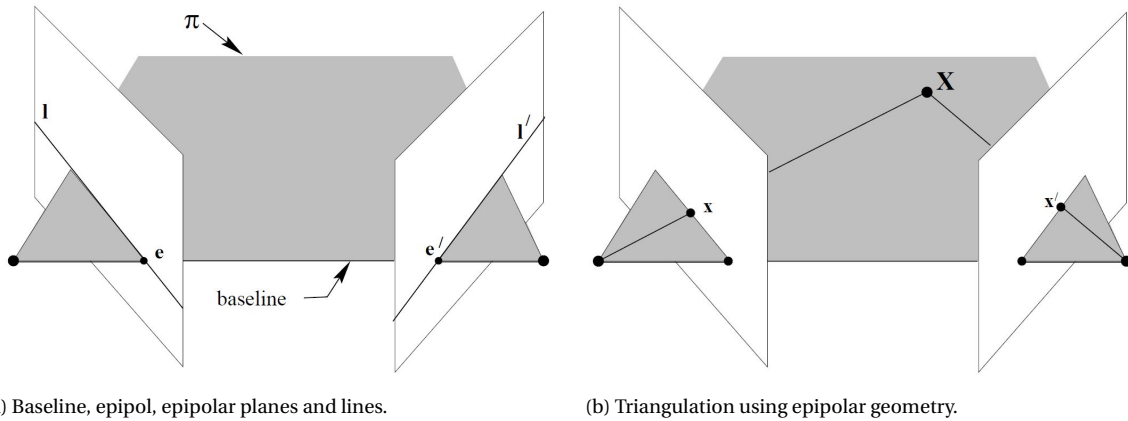
Figure 2.3: Epipolar geometries of a two view setup, the second camera being denoted by a prime. [23]

The epipolar planes are determined by the fundamental matrix $\mathbf{F}$, which is defined by correspondences between points in the two image planes:

$$\mathbf{x}^T\mathbf{F}\mathbf{x} = 0. \tag{2.9}$$

Identically to the camera matrix the fundamental matrix is only determined to scale, thus it has 8 degrees of freedom. The fundamental matrix is an essential part in describing two camera geometries and correspondences and can be used in different ways.

First, it can be used to calculate the epipolar line,

$$\mathbf{l}' = \mathbf{F}\mathbf{x}. \tag{2.10}$$

This could for instance be useful when point correspondences are being searched. If the epipolar line is known, the search region can be limited to this line, or a small band around it, as for instance done by Walker et al. [47]. In this case, the fundamental matrix could for instance be determined by the two camera matrices using the following equation:

$$\mathbf{F} = \mathbf{e}' \times \mathbf{P}'\mathbf{P}^+, \tag{2.11}$$

where $\mathbf{P}^+$ is the pseudo-inverse of $\mathbf{P}$ [23].

Another use can be the determination of the camera matrices using the fundamental matrix. The fundamental matrix can be calculated from Equation 2.9, using 8 or more point correspondences. As point correspondences typically contain some errors, typically more than 8 point correspondences are used to have an overdetermined system that is solved by methods such as those described in Section 2.2.2. Once the fundamental matrix is known, the camera matrices can be determined. Usually, the coordinate system is placed in the principle point of the first:

$$\mathbf{P} = [\mathbf{I}|\mathbf{0}], \tag{2.12}$$

where $\mathbf{I}$ is a 3×3 identity matrix. Then, the second camera matrix is calculated as follows:

$$\mathbf{P} = [\mathbf{e}' \times \mathbf{F}|\mathbf{e}'] \tag{2.13}$$

[23]. As the camera matrices are now known, world points can now be determined as will be explained in Section 2.2.3. This shows one of the strengths of stereo imaging: Both determining the camera geometries and calculating world point locations can be done from an initially uncalibrated setup as long as sufficient point correspondences can be determined from the stereo image pair. This for instance allows calibration planes to be located at arbitrary locations in space within the calibration process.

This process is typically done using a bundle adjustment process. Therefore, the reprojection error of the triangulations using the corresponded points is minimized using different optimization approaches. A decent initial guess of these variables is necessary to achieve convergence, which are typically determined using one of the simple calibration methods discussed before. The cost of such an optimization process increases however rapidly with the number of variables, therefore often only the extrinsic matrices are improved using this process [47, 49].

2.3. Passive optical 3D shape measurement

2.3.1. Point Tracking

The term Point Tracking is used here to describe methods that track distinct points or features on flapping wings to determine its deformation, an example is shown in Figure 2.4. Additional points on the wing surface allow considerably higher resolutions compared to the earlier methods presented in Section 2.1. Several different steps need to be undertaken to have a working method: Initially, points or features and their exact location are identified in two or more camera views. These points then need to be matched correctly across the views. Here, the camera principles can for instance be used, which are also necessary to determine the depth information as explained in Section 2.2. Matching then also needs to be done over the different frames or time steps that are recorded, which is often done by tracking the initial point distribution. Tracks of points representing the wings are then acquired. If necessary, the final full-field wing surface can then be determined by interpolation methods. Generally, Point Tracking is a broadly used approached and well documented. Several commercial applications also exist, however are not commonly used in flapping-wing applications in literature.
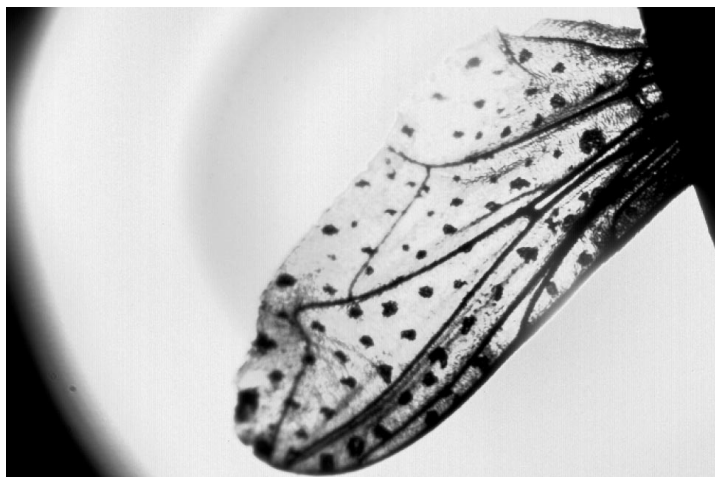
Figure 2.4: Housefly wing with added markers used for tracking. [49]

Flapping wing applications   Wallace et al. [49] were the first to develop a Point Tracking method to be used for measuring the deformation of insect wings. They proposed to use multiple cameras giving N views to record the predominantly transparent wings which are illuminated by separate collimated laser beams. The method is based on a central projection theory using the pinhole model plus corrections for radial and tangential distortion as proposed by Brown [6]. The calculated camera matrices, except the distortion parameters, were further improved using a bundle adjustment technique.

A spot grid illuminated by white and laser light recorded by 0.5 megapixel cameras are used as a reference test setup to further investigate the mean pixel error, MPE. An empirical relation of

$$MPE \approx 0.1(1 - 1/N), \quad \sigma \approx \pm 0.05 \tag{2.14}$$

was found for a static reference test case, indicating that the error is inversely related to the number of views. The MPE was then linked to the real world error, which is calculated as the difference between known grid positions of reference plates and the measured grid positions, which are determined using correlation methods. The relation was determined to be

$$error \approx MPE \frac{50}{498\sqrt{N-1}} \approx \frac{5(1 - 1/N)}{498\sqrt{N-1}}. \tag{2.15}$$

Generally, the determined in-plane errors correspond closely to the confidence in the grid spacing. Errors in out-of-plane direction however tend to be larger, around an order of magnitude larger than a reference measurement made by a high precision white light interferometer or twice the in-plane error. White light thereby outperforms laser light, which is negatively affected by light speckle which increases the error in spot centroid determination.

Lastly they applied the developed framework to a static measurement a housefly wing with painted spots, shown in Figure 2.4. With $MPE(N = 10) = 0.8$, errors were larger than those of the calibration target, likely due to the larger irregularity of the hand-drawn markers. Generally, they postulated that the Point Tracking algorithm should be well suited for measurements of flapping wing deformations. Dynamic effects such as blur were shown to have low impact.

The work of Walker et al. [47] used a quite comparable setup to study wing deformations of tethered locusts and free flying hoverflies, again using a bundle adjustment for the improvements of the extrinsic camera parameters.

A central part of the work is the addition of a semi-automatic method for Point Tracking of the tethered locust, as previously the matching was done manually. They used four cameras of

0.5 megapixel to 1 megapixel resolution and 975 Hz recording rate, two on each side of the subject, to track around 100 manually placed points on the hind-wing and around 22 natural features on the back wing (See Figure 2.5a). The tracking procedure was then as follows:
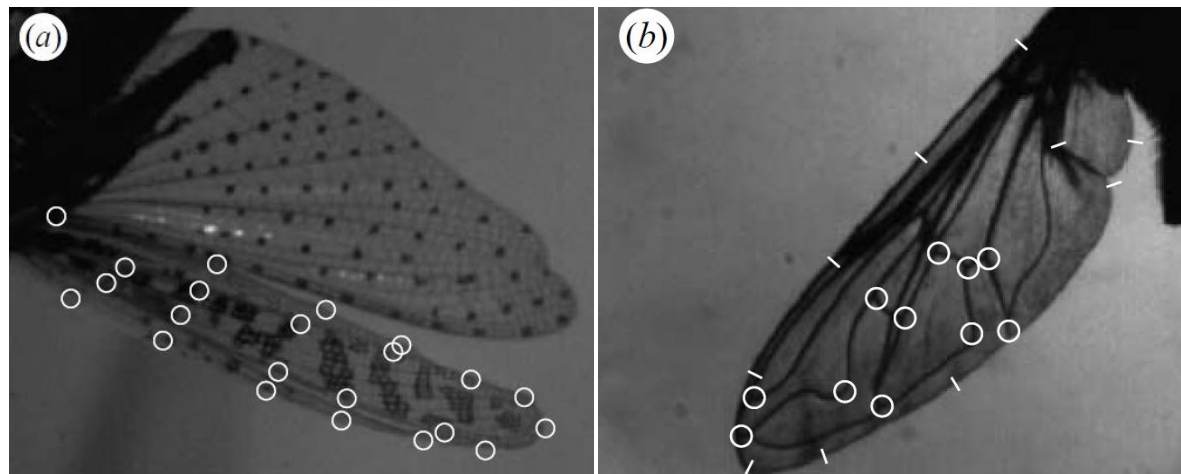
(a) Locust wings with natural features on fore-wing (circles) and points on hind-wing(black dots).

(b) Hoverfly wing with natural features (circles) and points on wing edge found using epipolar geometry (lines).

Figure 2.5: Insect wings with tracked points. [47]

First, all points were manually found in all views for the initial wing beat cycle. Based on this, the wing shape for the first cycle was determined to later be used as a template. Some points were thereby lost for parts of the cycle due to wing-folding. For proceeding frames only the wing tip needed to be marked. The algorithm then found the two closest matches in the template and re-projected linearly interpolated world points into the four camera views using the DLT relations (Equation 2.2) to be used as an estimate of the point location. The exact location of a point was then determined as the location with the least square error between the grey level of the search region of the new image and previous template image. Once all points were found in all views, their new world position was determined using the DLT algorithm. In total this was repeated for 10 different recordings for 5 cycles each. Overall, around 96 % and 92 % of the points could be tracked for the hind and fore-wing, respectively. The fore-wing showing a slightly lower ratio due to the lower contrast of the tracked natural features compared to placed high contrast dots.

Once the 3D position of all points were found, the point tracks were filtered to reduce the measurement error. Therefore, a forwards-backwards third-order low-pass Butterworth filter was applied that eliminated all frequencies above the eight harmonic which are assumed to be erroneous. Based on this, cubic splines were used to fit the wing outline and a regular spaced fine mesh was fitted to the wing surface. This gave the first high resolution measurements of flapping-wing deformations with only limited assumptions and relatively low uncertainty.

The general approach was also applied to the flying hoverfly, however some simplifications had to be made due to the varying attitude. While the camera setup was similar with four 1 megapixel cameras, giving a mean reprojection error of around 0.2 %, the tracking could no longer be automated as the body position was not steady. Furthermore, only a limited amount of points could be identified and tracked. These were 12 natural features, together with 10 arbitrary points on the wing edge as shown in Figure 2.5b. The edge points were identified using principles of epipolar geometry: An arbitrary point lying on the wing outline was selected in one view, the corresponding epipolar line could then be drawn in the other views as explained in Section 2.2.4. The intersection of the epipolar line with the wing outline is then the point location. This assumes that no errors have been made in the previous steps, for instance in calibration or point selection, otherwise the epipolar geometry becomes a finite thickness band. In total, this procedure was done for 20 cycles.

Koehler et al. [28] implemented a similar manual method for free flying dragonflies. They used an orthogonal three camera setup with 1 megapixel resolution. Thereby they reduced the number of tracked points to 15 to 16 placed points per wing, arguing that higher recording resolutions is not worth further complications of the free flight measurements. Instead, B-spline interpolation methods showed to give smooth surfaces for arbitrary mesh typologies, making them a satisfactory interpolation method. Small scale corrugations of the wing model were then later overlaid using static shape measurements.

Furthermore, they added an algorithm to avoid lost points within the flapping cycle, which occurred in about 5 % of the measurements. Whenever a point could not be identified in two or more views, making triangulation impossible, a B-spline interpolation of the point location in adjacent time steps was used to estimate the point location.

Nakata et al. [34] were among the first to implement a Point Tracking algorithm to flapping-wing MAV. They used three 1 kHz cameras with about 0.5 megapixel resolution to record wing deformations of a four-wing MAV mounted in a wind tunnel to mimic forward flight, making this setup very similar to that of interest in the later thesis. Recorded images, an example is given in Figure 2.6, are imported into the commercial software DippMotion (Ditect), which automatically calculates point tracks, minimizing the amount of manual labor. The wing shape was then determined using a function of Fourier series for interpolation. Wing twist and camber change could then be reconstructed. This shows that the shape of multiple wings in close proximity can efficiently be measured using a Point Tracking method.
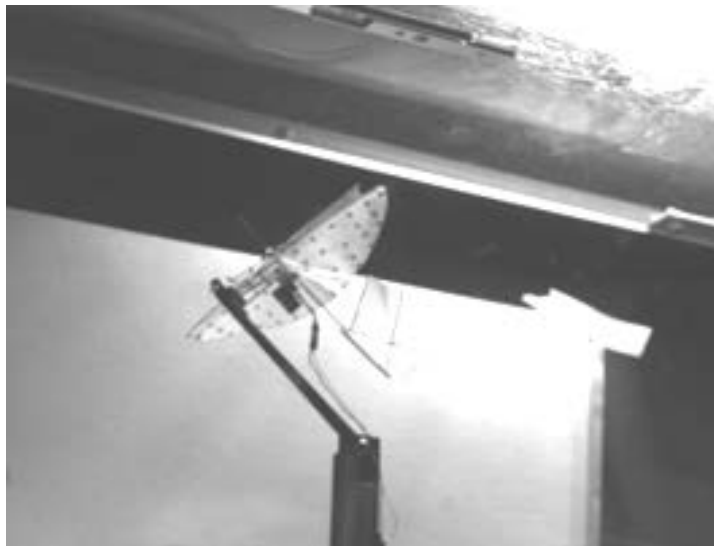
Figure 2.6: Recorded image of four-wing MAV with makers in windtunnel. [34]

However, some limitations were present in the study. First of all, parts of the lower wing could not be tracked in the phase where the wings are in contact. Furthermore, the resolution of the tracking was limited. Only approximately 20 points were marked on a wing, corresponding to the stated 5 mm resolution of the system. This resolution is especially poor for the fact that the MAV is tethered, making the framing easy. Also, no comment was made towards the accuracy of the wing in the report and is likely not given by the commercial software, which makes uncertainty quantification in later stages difficult.

The DelFly studies of [37] were one of the latest implementations of Point Tracking to flapping-wing shape measurements. Compared to [34], they considered only the hover case where the wing deformations on each side are symmetrical, thus only one wing needed to be tracked. The used

setup comprises two high-speed cameras with 1 megapixel resolution at 1 kHz to 2 kHz recording frequency orthogonal to the wings to measure their shape plus an identical one orthogonal to the stroke plane to record the stroke angle. Recording, calibration and image preprocessing was done within the commercial software DaVis (LaVision).

Compared to previous implemented algorithms, the Point Tracking is mostly automated using a developed algorithm which is explained in detail. Initially, three points defining the wing orientation must be selected in each view. Then, the algorithm finds the 200 image points by itself using the specified grid structure as an initial estimate of the point locations followed by a Hough transform together with centroid detection to determine the exact location of the point. Triangulation is then used to determine the world coordinate of the marker points, where points which projection lines miss by more than 1.4 mm are neglected. The algorithm is repeated for the proceeding time steps, where the initial estimate is improved by using a prediction of the point location using its measured kinematics. Manual input is necessary occasionally when points are lost. The average distance between projection lines was 0.1 mm, which is about 0.07 % of the half wing-span. To determine twist and camber, the final wing outline was extrapolated using the outside points of the mesh grid.

Discussion   Point Tracking showed to be quite well suited for applications to flapping wing shape measurements. The DLT algorithm forms an accurate foundation to the algorithms. Complications are then the efficient detection, matching and tracking of the markers and their exact position, which determines the accuracy. While for free-flying objects manual methods are still necessary, for tethered objects several methods have been implemented allow automated point finding, full automation is however still rarely used. Initial estimates of the point location can be found using point templates to interpolate from [47], or grid structure information and prediction methods [37]. The exact point location can then be found using correlation methods [49] similar to using least square errors in the grey levels of a search region [47], or Hough-Transform and centroid detection [37]. Achieved spatial resolutions lie upwards of 100 points using a 1 megapixel camera and accuracies can range between 0.07 % and 0.2 % of the wing span [37, 47] or of sub-pixel level [49]. If a continuous representation of the wing shape is necessary, interpolation techniques exist that were shown to give satisfactory results [28, 34].

2.3.2. Digital Image Correlation (DIC)

Image correlation can be understood as a technique that identifies corresponding locations in two images by minimizing the difference in its surrounding pattern or intensity values by shifting the subset window. The recorded object must have a high contrast texture, therefore speckle patterns are often applied, as shown for instance in Figure 2.7.
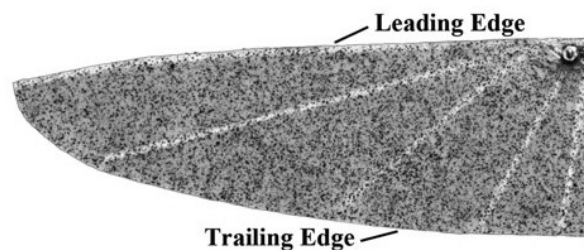
Figure 2.7: Typical DIC speckle pattern applied on flexible wing. [56]

At the core, a Digital Image Correlation (DIC) approach compares sub-windows of different images and finds the specific shift in pixels of the region as the peak in the correlation coefficient. Different versions to calculate the correlation coefficient exist thereby, often individual pixel inten-

sities are multiplied. Different methods to find a window shift below a pixel size exist, for instance bilinear interpolation of the pixel intensities [45] or interpolation of the correlation window peak.

In the DIC applications, this pixel shift between windows typically represents the strain of a planar object. This process can however also be used to measure 3D shapes and strains by correlating window shifts not only done in time but also between the cameras. Those methods are based on the principles introduced in Section 2.2 to calculate the real world position of a point based on the corresponding locations in two or more camera views. Epipolar geometry can be used to limit the search region to a single line or band. The image is often rectified along that line, which allows easier considerations of the subimage projective transformations in rotated camera views. Several commercial software packages exist today that allow for straight forward use of DIC, which shows the maturity and widespread use of the method.

Flapping wing applications   The first applications of DIC to measure the shape of flapping-wings were done by Stewart and Albertani [43], basing their applications on the work of Albertani et al. [5], who investigated deformations of highly flexible MAV wings. Several different wing geometries were tested, flapping of frequencies between 5 Hz to 10 Hz with angles of up to 16.5°. A stereo camera system was used with a recording frequency of 100 fps. These images were then processed using the commercial software VIC-3D (Correlated Solutions) to obtain the wing deformations. The software determines the wing shape by correlating the image sequences to a reference image of the undeformed wing [56]. Other details were not noted. Calibration of the stereo system including camera intrinsic parameters were also discussed, were however likely done inside the software as this is one of the functions.

Each wing had a rigid section attached that is used to determine the purely flexible deformations of the wing by subtracting the rigid body rotations of the wing. Uncertainties of the flapping angle as large as 1.01° or 22 % of the maximum angle exist for some flapping frequencies due to the shortcomings of the rigid transformation model. Nonetheless, first full field measurements could be made. Errors of the system were calculated to lie between 0.3 mm to 0.9 mm or 0.2 % to 0.6 % of the half wing span.

Wu et al. [56] extended the application to a flapping angle of ±45°, which is a more common range for insects and in MAV applications. This poses higher requirements on the measurement setup. In total four cameras with around 2 megapixel resolution are used, configured in two pairs which record the upper and lower part of the flapping cycle separately (see Figure 2.8). It was assumed to enable recording of flapping ranges of up to 180°.

The images were acquired using a stroboscopic illumination technique. Recordings are done at a relatively low frequency of 15 fps maximum for multiple cycles, which are then sorted to a single cycle using the phase angle of prominent point on the driving mechanism. This allows relatively simple cameras to be used, while ensuring sufficient exposure, however measurement uncertainty is increased due to temporal variations over longer measurement periods and tracking algorithms would be complicated. The author notes for instance a variation of up to 10 % in the flapping frequency, which was accounted for by the phase recognition system, however cannot be accounted for otherwise. Perçin et al. [37] showed that such variations can give considerable differences in wing efficiency and shape.

Camera calibration and DIC is again executed within VIC-3D. Due to small errors within the calibration process, the processed data of the two camera pairs had to be aligned by rotating and translating the results so that they match in the image plane. To determine the pure shape deformation three points near the wing joint are used to represent the rigid body rotation, which was then isolated from the total shape to give the pure deformations.

Accuracy estimations were done later in Wu et al. [57] for the similar wing geometries with flapping frequencies of up to 35 Hz and ±35° flapping range. While the phase angle uncertainty was
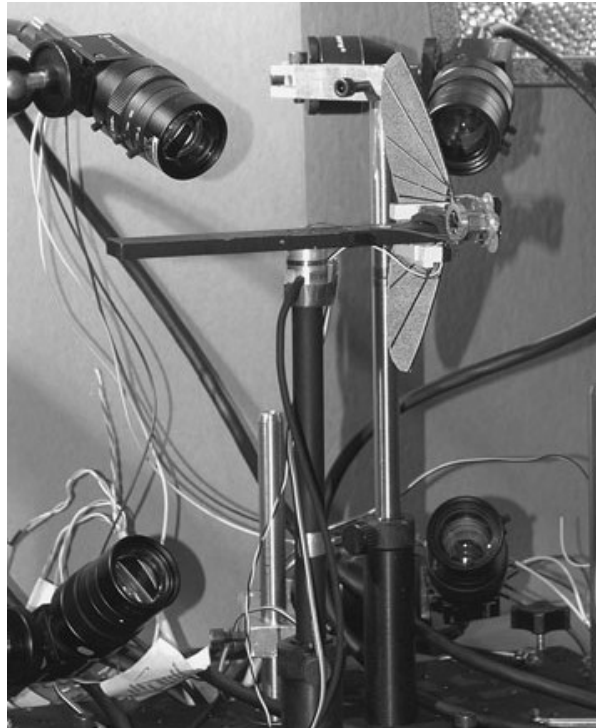
Figure 2.8: DIC setup including two stereo camera pairs. [56]

estimated to be 12 %, the geometric uncertainty is under ±0.1 mm, which is around 0.13 % of the half wingspan.

Several other studies have been carried out on different MAV and insects. Mostly different commercial software packages were used, another example being StrainMaster developed by LaVision used by Coleman et al. [9] to record a hummingbird inspired MAV in hover or Ha et al. [22] who used the software AMARIS developed by GOM to measure a beetle inspired MAV.

Discussion   The ease at which high spatial resolution can be achieved is one of the main upsides of DIC. While the method does not typically give true continuous measurements of deformation or strain, the images can be sampled in arbitrarily small steps as the measured object has a continuous pattern applied. Accuracy of the system is also high when the correct patterns are used. This holds also for the 3D triangulation, as the underlying theory is well known and can make use of advanced calibration methods [22]. Several commercial software packages exist, which show the maturity of the method as well as a large general interest in the technology.

The flapping-wing application poses thereby some difficulties for the DIC method. To achieve good correlation, the pattern must be captured with high contrast and minimal blur. Therefore, exposure times must be low, often within tens of microseconds, and sensor illumination must be large. These requirements typically contradict themselves and are only overcome by using high intensity light. This is often done using stroboscopic lighting [9, 56], which can however require many cycles to be recorded, increasing the uncertainty due to varying conditions. Furthermore, the large flapping angles can lead to a distorted pattern, which is also unfavorable and reduces the chances of successful correlation. For this reason, often multiple stereo pairs are used which record separate areas of the flapping phases [56]. Achieved accuracies reach up to 0.13 % [43, 57] and resolutions of 0.87 % have been reported [9].

2.4. Active optical 3D shape measurement

As mentioned in the introduction, the term active measurement techniques encompasses all optical metrology methods that make use of specialized light sources to give information to images recorded by camera setups. Active techniques can thereby be split into two groups: Triangulation methods which make use of how the projected light is distorted on the object of interest, and time delay methods use the temporal information of the emitted and absorbed light.

For active triangulation techniques the light source acts like an opposite of a camera, i.e. emitting light instead of absorbing it, but can be modeled the same way as a camera, explained in Section 2.2. Fringe analysis methods, which are based on projected light planes or fringes are presented first in Section 2.4.1 to 2.4.4, followed by general Structured Light techniques in Section 2.4.5.

Time-of-flight (TOF) is a time delay method that measures the time passed between emission and sensing of the light, which gives the total outbound and return distance to the object when multiplied with the speed of light, explained in more detail in Section 2.4.6. Digital holographic interference (DHI) uses the known light wavelength to measure distance by recording the phase information within a hologram. This is explained in more detail in Section 2.4.7. Neither of these methods are commonly used for flapping-wing deformation measurements, however as they generally fulfill the necessary requirements, an overview is given for completeness.

2.4.1. Fringe Shadow

The Fringe Shadow method is simple approach of measuring flapping angle and twist, initially developed by Zeng et al. [63] to study dragonfly wings. The method works by recording the shadows of a wing illuminated by two orthogonal fringe pattern projector (FPP) lasers projecting collimated comb fringes. The shadow region of the projection effectively is the projection of the wing in two dimensions, which was used to determine the local twist angle and flapping angle. Similarly to the work done by Willmott and Ellington [53] camber deformation could not be accounted for, which makes the method unsuitable for applications with camber changes.

2.4.2. Projected Comb Fringe (PCF)

Song et al. [41] were the first to obtain camber deformations of flapping-wings using a tethered dragonfly as subject.

While Zeng et al. [63] stated the reflectivity of such dragonfly wings can be too weak, leading to unrecognizable distorted fringe pattern, Song et al. [41] stated that the specular or mirror-like reflections of the dragonfly wing are sufficient for a PCF method. Diffusive reflection was said to be still insufficiently small, thus sine fringes that give true full-field resolution could not be used as the phase information (see Section 2.4.3) would be destroyed.

The general setup used by Song et al. [41] is shown in Figure 2.9. The FPP is placed at 45° with respect to the image plane and aligned so that the fringes are projected onto the dragonfly body (see Figure 2.9c). The normal vectors of all fringes are known by a numbering relative to the dragonfly body, which allows the calculation of the world coordinates of any point lying on a fringe using simple algebraic relations. This allows the determination of the incidence angle using the fringe endpoints, and also the camber by selecting multiple random points along a fringe. As only one camera view was used, the problem of matching points between cameras no longer exists. Points along the camber were then interpolated to give a consistent chordwise spacing. The entire wing shape was described by the sum of the camber profiles, which was again interpolated as required.

This setup allowed the measurement of flapping angles between ±30°. Typically, 5 to 9 fringes can be seen on a wing with a spacing of 4 mm to 8 mm. The accuracy of the system was also stud-

(a) Measurement setup and coordinate system.

(b) Comb fringe projection on dragonfly.

(c) Recorded fringe pattern on dragonfly wing.
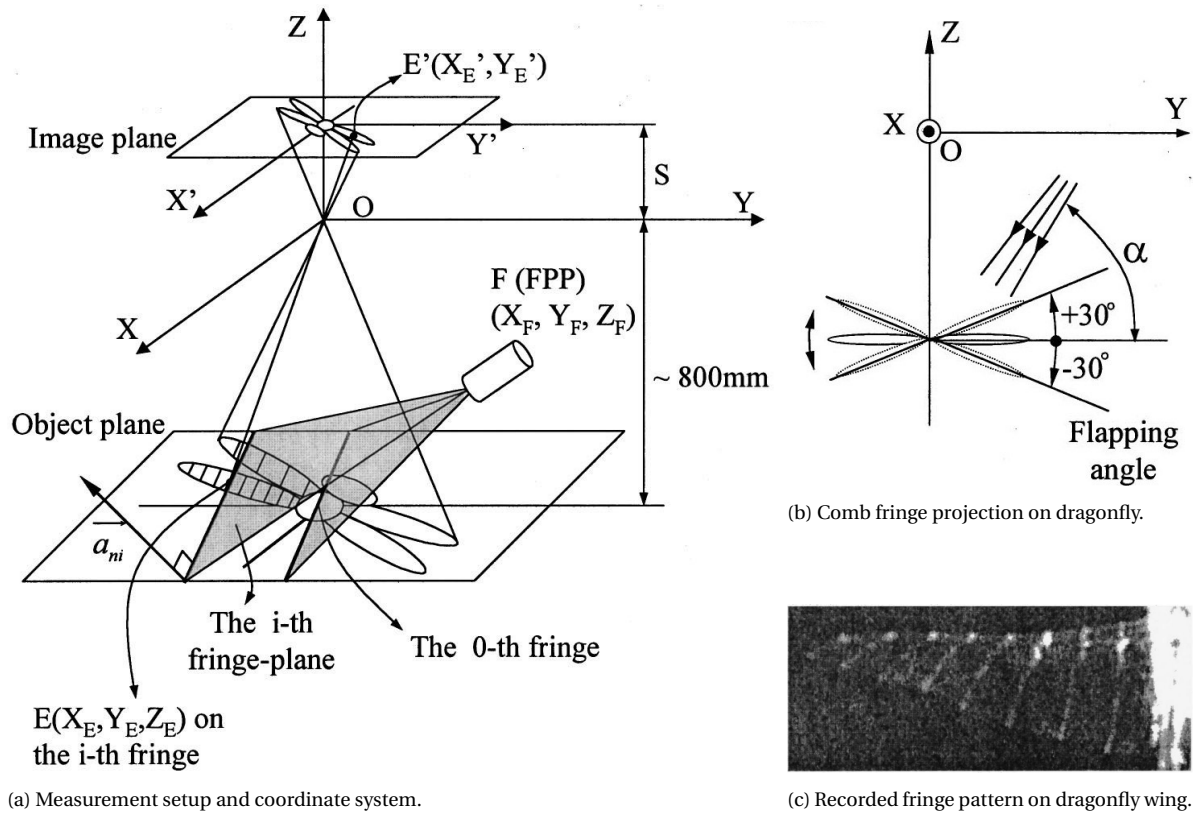
Figure 2.9: PCF configuration and example recording. [41]

ied. A cylinder with known radius was used as a reference object, which could be measured with a standard deviation of 0.42 % relative to the diameter. The main error cause is seen in the digitizing of the fringes.

Wang et al. [51] extended the method to allow measuring of free flying dragonflies. As the insect body was no longer fixed, it could no longer be used to determine the 0th fringe plane. Instead, an additional laser was used to project a laser sheet that represents the 0th fringe and determines the order of the remaining fringes. Furthermore, the coordinate system origin was placed on the lowest of a set of calibration planes, which were introduced to work as new depth calculation method. Images of the planes with projected fringes at different known Z locations were taken and used to calculate the slope of the fringe planes using the known order. Accuracy of the system was found to be slightly improved, also as lens distortions effects were captured now in the calibration images. For the reference case of a cylinder the relative uncertainty was now slightly better with a measured standard deviation of 0.1 mm or 0.26 % of the cylinder diameter. Limitation of the accuracy is here seen in the camera resolution, which is only 260 pixel × 260 pixel.

Wu et al. [55] addressed the problem of the limited flapping range that could previously be measured. So far, the recordings were limited to a range of ±30°, which would require multiple recordings at different orientations to measure the complete flapping cycle of insects with larger flapping angles. To allow for this larger range, they used two of the previously used setups configured orthogonally. As the fringe sheets of both systems are not parallel, this gives a 2D-fringe pattern on the wings, which was however still evaluated separately.

The method developed by Deetjen et al. [13] can also be classified as a comb fringe method.

They used a high-frequency projector to project a binary, orthogonal 2D grid which spacing varies in one dimension onto a small parrot flying between perches, which allowed the calculation of the wing shape using the introduced triangulation methods.

The varying fringe spacing was used to determine the order of the recorded fringes. The fringe planes recorded by the camera can be calculated by defining that they intersect in the projector lens. Then, the individual angle of a set of projected, known planes is matched with unknown planes of the camera. The correct match is found where the squared difference in angle is minimal, visualized in Figure 2.10. After the horizontal fringes is matched, the calculated variables can also be used to match the regular spaced vertical fringes. Corresponding camera and projector pixels are then known by the algorithm, which allows the calculation of the real world coordinates according to Equation 2.8 using the previous stereo calibration.
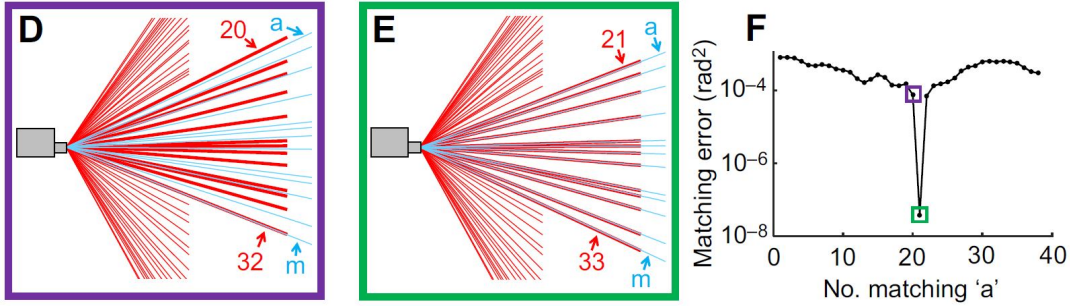
Figure 2.10: Fringe matching, red are known projection fringes and blue are ordered but unknown camera fringes. [13]

On average, the final measurements consisted of 285 grid intersections and over 10000 other fringe points, which where then interpolated to over 25000 points. The accuracy of the system when measuring a reference sphere was determined to be 0.31 mm or 0.7 % of the diameter. While this is slightly worse than previous comb fringe methods, the much higher resolution and complete automation of the system is a significant advantage, together with the robuster triangulation framework. Furthermore stereo angles between projector and camera can be reduced, increasing measurable flapping ranges.

2.4.3. Sine Fringe

Compared to the PCF method, the sine fringe method gives true full-field shape measurements as now the continuous light intensity gradient can be used to match any camera and projector points. Compared to most other methods it is one of the newest and least mature, however a significant amount of development was done in recent years.

The method is based on the Fourier transform profilometry (FTP), originally developed by Takeda and Mutoh [46]. In FTP a camera records the distorted sinusoidal fringe pattern projected onto an object. A typical setup is shown in Figure 2.11a, where the sinusoidal fringes are projected on a plane orthogonal to the figure. FTP calculates the local height $h(x, y)$ of an object based on the distance $\overline{CD}$ in a reference plane R, which occurs due to trigonometric principles described above. Based on the distance d between camera and projector and their offset l_0 from the reference plane,

$$h(x, y) = \frac{l_0 \overline{CD}}{\overline{CD} - d}.$$ (2.16)

$\overline{CD}$ can be represented as the phase shift $\Delta\phi(x, y)$ between the recording of the projection on a reference plane and the object:

$$\Delta\phi(x, y) = 2\pi f_0 (\overline{BD} - \overline{BC}) = 2\pi f_0 \overline{CD},$$ (2.17)

(a) Basic crossed axis FTP setup and geometry.   (b) Sine fringe pattern on bottle shape.

Figure 2.11: FTP setup and example recording. [46]

where f_0 is the fundamental frequency, which diverges in the images if non-telecentric projections are used. Therefore both recordings are filtered in Fourier domain, to retain only the spectrum of the phase while removing all unwanted effects, for instance due to the reflectivity of the object. After multiplying the complex signal of the reference plane with the complex conjugate of the object and calculating the logarithm, $\Delta\phi(x, y)$ is obtained. The obtained phase shift will be limited to a range between $-\pi$ and π, which needs to be unwrapped to give the total phase. This is relatively trivial if the object has continuous height changes which result in low phase changes between pixels, however advanced methods need to be employed when more general cases are studied [8, 29, 44]. The final unwrapped phase can then be inserted into the geometrical relation of Equation 2.16 to give

$$h(x, y) = \frac{l_0 \Delta\phi(x, y)}{\Delta\phi(x, y) - 2\pi f_0 d}.$$ (2.18)

As the phase signal is measured at pixel resolution, so is ultimately $h(x, y)$, thus full-field measurements with pixel resolution are obtained with this method.

Flapping wing applications   While reflectivity is accounted for in theory, very high changes will still prevent useful measurements. This prevented early measurements of flapping wings, which was first overcome by Cheng et al. [8], who applied the modified Windowed Fourier Transform (WFT) method to study dragonfly wings. This modification separates the recorded images or signals into smaller subsets which further reduces the effect of poor image quality and noise. The window size does however affect the results significantly and needs to be selected carefully, here a subset size of 20 × 20 pixels were used. Furthermore, they used a parallel grating to generate a telecetric fringe pattern and assumed that the distance l_0 between camera and object is much larger than the measured dragonfly wing, which simplified the depth calculation to

$$h(x, y) = \frac{\phi(x, y)}{2\pi f_0 \tan(\theta)}.$$ (2.19)

This allowed him to get first true full-field results of the dragonfly with reasonable detail.

Sine fringe methods became much more popular in studies on MAV, as wing material properties could now be choosen, thus reflectivity was no longer problematic. Zhang et al. [64] used an off-the-shelf digital micromirror device (DMD) projector for the sine projection and a high-speed video camera to record the images of the MAV flapping at 30 Hz and 100° flapping range. The typical light flicker of DMD projectors and their detrimental effect on the image quality was not discussed. DMD projectors regulate the intensity, here a sinusoidal distribution, by varying the amount of time the mirror angle is set to an "on" position where the light is reflected through the projection lens. This effect was studied more by Gong and Zhang [19], who suggested using a binary pattern, allowing mirrors to be set to "on" respectively "off" continuously, which is defocused to form a quasi-sinusoidal pattern.

The shape measurement algorithm is based on a full field 3D FTP method. The Fourier transform is not only take in x and y dimension, but also in time t, which reduces the likelihood of temporal reconstruction errors. Phase unwrapping is trivial as long as the phase change between all pixels and frames is below π. The wing shape is lastly calculated from the phase shift as given in Equation 2.18.

Presented results show a very high temporal and spatial resolution. The wing flapping angle shows however some very abrupt changes, which might indicate some remaining noise in the measurements. Uncertainty estimates are again not given.

Li and Zhang [29] apply other improvements made for sine fringe projection to the measurement of MAV flapping-wing deformation and body position in hover. They applied a Modified Fourier Transform Profilometry (MFTP) method to give accurate results of the fast flapping wings together with Four-step phase shifting profilometry for better unwrapping that allows determine the absolute phase for both wings and MAV body.

The MFTP method uses the recording of two sine fringe patterns I_1 and I_2, phase shifted by π. The mean of both signals will give the object image, while their difference contains pure phase information. Using Fourier transformation and filtering the height can then be calculated as

$$\phi(x, y) = \arctan\left(\frac{Im[I_f(x, y)]}{Re[I_f(x, y)]}\right), \tag{2.20}$$

where $Re[I_f(x, y)]$ is the real, and $Im[I_f(x, y)]$ is the imaginary part of the filtered complex phase intensity $I_f(x, y)$. This is a very neat technique, which reduces the noise of the relevant signal significantly and furthermore allow a larger height gradient range as derived by its inventors Li et al. [31].

For the Four-step phase shifting profilometry two additional patterns are recorded as I_3 and I_4, which allows the phase to be extracted without taking a Fourier transform as

$$\phi(x, y) = \arctan\left(\frac{I_3 - I_4}{I_1 - I_2}\right). \tag{2.21}$$

The arc-tangent function in both Equation 2.20 and 2.21 shows that the phase will again be wrapped. For this reason, in addition to the recordings I_1 to I_4 with a high spatial frequency, four more recordings I_5 to I_8 with a low spatial frequency with a period similar to the sensor size are taken. This reduces the effect of the 2π phase range, while the high frequency images retain high accuracy. For the wings the MFTP method was used with I_1 and I_2, while for the body I_1 to I_4 was used to account for geometrical and textural changes. The respective surfaces are then stitched together using geometric relations discovered from the object image. The general flow is shown in Figure 2.12.
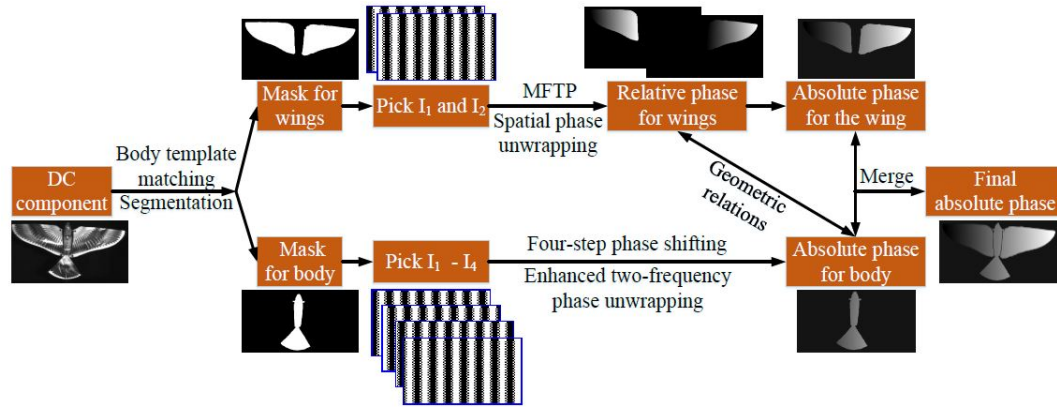
Figure 2.12: Hybrid sine fringe flowchart. [29]

The method used to calculate the object shape from the absolute phase is explained in Li et al. [30]. Calibration images of planes in different locations are used to obtain a correspondence between projector and camera pixels, and also to determine the intrinsic and extrinsic matrices of the camera and projector. This then allows the use of the extended pinhole model for both camera and projector as explained in Section 2.2.1 and Equation 2.8 to calculate the real world coordinate corresponding to a local intensity and phase.

Discussion The sine fringe method allows to make full field measurements of wing deformation. However, the approach has several requirements. The wing material must be opaque and with homogeneous reflectivity to obtain decent phase information. Furthermore, typically multiple shifted patterns must be recorded, which requires both a high-speed camera and projector for higher flapping frequencies. While high-speed cameras are relatively common, high-speed projectors are much scarcer, making the method less favorable and complex together with the relatively high calibration and processing requirements.

Nonetheless, the technique allowed deformation measurements of previously unobtained detail and accuracy at relatively high flapping frequency. The highest measurement quality was obtained by Li et al. [30], which used a specialized projector refreshing at 5000 Hz with 2 megapixel resolution, which allowed close to 1000 Hz temporal resolution using 8 patterns. Some unevenness in the wing surfaces can however still be seen, it appears that the wing texture might still have some effect on the shape measurements. The errors of the system applied to different reference cases was determined by Li et al. [30] to be around 0.09 % to 0.12 %.

2.4.4. Moiré

Another technique that practically falls into the fringe analysis range are Moiré methods. No measurements of flapping-wing shapes could be found, also because the method is relatively unfavorable compared to the better described comb- or sine-fringe methods.

The technique is called after the Moiré effect, which occurs when two similar patterns overlap and form another pattern, as visualized in Figure 2.13a, Using the exact orientation of the fringes depth information can then be calculated. Typically, one of the pattern is projected by a laser while the other is simply overlaid on top of the camera image that recorded the other pattern, visualized in Figure 2.13b and 2.13c.

Fleming et al. [18] applied the principle to measuring the flexible wings of an MAV, similar to that later measured by Albertani [4], Albertani et al. [5]. They acquired quite reasonable results with

(a) Moiré depth measurement schematic. [59]

(b) Projected fringe pattern recorded by the camera. [18]

(c) Superimposed pattern to form Moiré contours. [18]
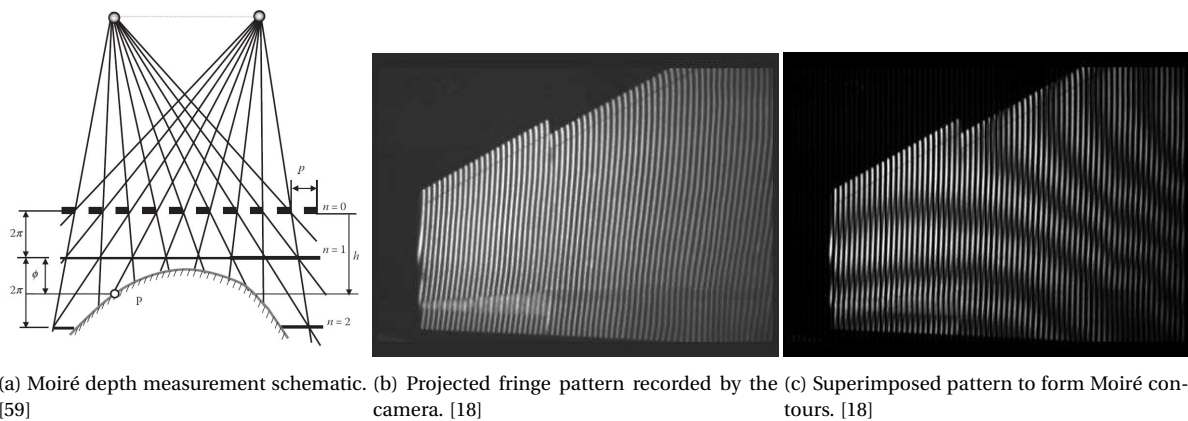
Figure 2.13: Moiré principles.

high resolution. The nominal accuracy of the system was 0.4 mm, which is around 0.26 % of the MAV wing span.

2.4.5. Structured Light

In principle, any pattern can be used to measure an object shape. Essential is thereby only that light source coordinates and image coordinates can be matched, which can also be done using a correlation or tracking algorithms. This allows the world coordinates to be triangulated using camera and projector models. As previously explained these can be acquired using a calibration, where typically by first the camera is calibrated using a calibration plate as explained in Section 2.2.2, and sequentially calibrating the projector optics using recordings of projections on reference planes captured by the calibrated camera, e.g. as done by Li et al. [30].

Flapping wing applications   Some measurements of flapping wing deformations using light projection have been made in the past. However, all found examples thereby use the light sources only to add additional texture to the wings without incorporating a light source model into the triangulation matrices. Thus, strictly speaking the following techniques are not truly active Structured Light methods, but only enhanced passive Point Tracking and DIC methods.

Curtis et al. [11] used two lasers to project structured grids of points onto different flapping wing geometries flapping at up to 7.5 Hz over a ±45° range. They used lasers to project points onto the wings which is supposed to further reduce intrusion by eliminating any added mass typically introduced in a Point Tracking approach. The fact that the points are not at the same location of the wing for varying flapping angles brought some implications. First, as mentioned before wing points were no longer tracked but only the general wing shape. Also, a balance had to be found for sizing the grid, either many points will not be projected onto the wing for large parts of the cycle, thus lowering the resolution, or wing regions will remain without points for parts of the cycle, making the measurements incomplete. This holds especially for the wing boundary, which makes the determination of the outline difficult.

The grids were formed using special projection heads, each giving a 7×7 point grid, totaling 98 points. In total four high-speed cameras were used recording at 1000 fps with 0.25 megapixel resolution. The cameras were configured in two pairs to measure the upper and lower half of the flapping cycle separately, similarly to Wu et al. [56]. Images of one camera can be seen in Figure 2.14. Calibration and processing of the recorded images was done within the commercial software Photomodeler 6 (PhotoModeler Technologies), using a typical point grid to determine camera pa-

rameters as explained in Section 2.2.2. In the first few recorded images points needed to be found manually, then the software finds most of the points in the remaining frames automatically. The point centroid is also determined by the software to obtain sub-pixel accuracy. To get a measure of the wing outline points the corner points were manually marked. The results appear to be decent, however no accuracy or resolution measure is reported.
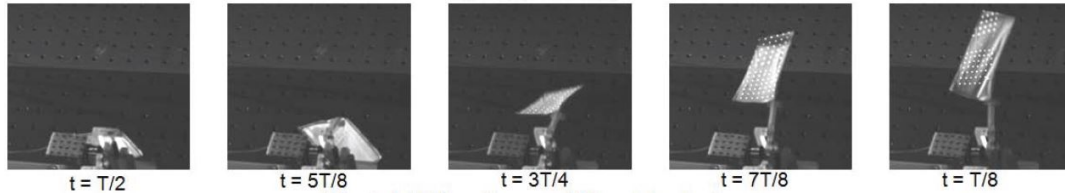
Figure 2.14: Images of laser point grid projected on flapping-wing taken over flapping cycle of period T. [11]

Wolf and Konrath [54] similarly used an approach where a passive method is enhanced by projecting additional texture onto the object. The studies measured the wing deformations of an owl in free-flight. Therefore, cameras and projectors were mounted onto a frame connected to a dolly that followed the flight path for several meters. As the owl wings have a finite thickness, cameras and projectors are placed above and below the wing to measure both the upper and lower wing shape. Initially a DIC approach was intended to be used to determine the wing shape using the natural wing texture for correlation. However, the texture prove to be insufficient for good correlation results. Therefore, additional high contrast speckle texture was projected onto the wings using multiple special high sharpness LED projectors. This technique is also called Projected Pattern Correlation Technique (PROPAC). The final texture recorded by a camera can be seen in Figure 2.15.
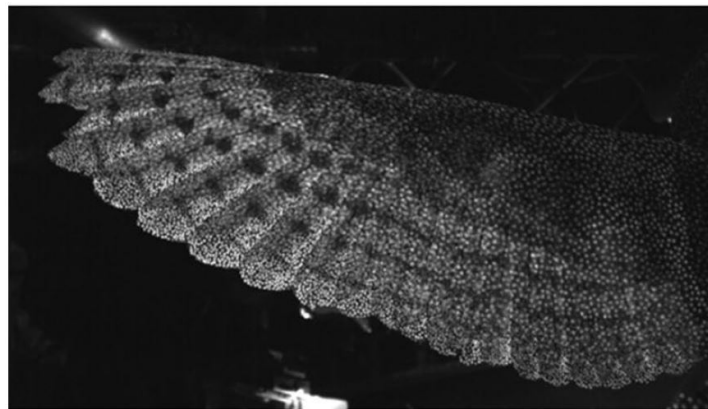
Figure 2.15: Owl wing with projected speckle pattern for increased texture. [54]

Different camera types were used for recording at 1000 fps, which gives excellent temporal resolution of the around 4 Hz flapping frequency of the owl. To increase the correlation accuracy, the recorded images were warped manually using features of the owl wings to obtain better matching of the correlation windows. The correlation process was then done within DaVis (LaVision), previously mentioned in Section 3.3, with correlation windows set to 16 pixel × 16 pixel with 70 % overlap for the upper wing and 24 pixel × 24 pixel with 60 % overlap for the lower wing.

Discussion   Generally, Structured Light approaches show some advantages compared to previous method. As for the fringe methods they reduce intrusion by not requiring any added texture to the wings, however they also reduce the high sensitivity to image quality of the sine fringe processing algorithm while maintaining high spatial resolution. Advantageous appears thereby especially the

PROPAC approach, which allowed to decent accuracy values of 0.09 % and relative resolution of 0.55 %.

Incorporating a light source model into the triangulation, making it a true active Structured Light approach should thereby improve the measurement quality even further as more views generally increase accuracy [49].

2.4.6. Time-of-flight (TOF)

To measure the shape of an object, the temporal information encoded in the emitted and absorbed light rays can also be used. TOF cameras measure the distance d of object from the light source and sensor by multiplying the time t a signal takes to travel from the source to the object and back to the sensor and light source using the light speed c. A simple relation is

$$d = \frac{1}{2}tc, \tag{2.22}$$

assuming camera and light are approximately at the same location in space. t can thereby be measured by different principles [24]. So-called pulsed-light methods measure the time between emission and sensing of a single light pulse in a relatively straightforward fashion. The light pulse is well defined with a duration typically hundreds of nanoseconds and intense enough to be clearly distinguishable by the sensor from the background illumination. Continuous wave methods use a light source that changes the emitted light intensity in form of a sinusoidal function. As the sensed intensity does not directly relate to the emitted intensity, reflectivity and background light intensity is unknown, the sensor must take four measurements per period to determine the phase difference ϕ between emission and sensing. The distance is then calculated as

$$d = \frac{c}{4\pi f}\phi, \tag{2.23}$$

where f is the pulse frequency. To avoid phase wrapping, the measurable distance is typically limited to $0 \le d \le \frac{c}{2f}$ [24].

The method is still in early stages and relies on relatively new and proprietary projector and sensor technology. While accuracy is acceptable with ratios of around 0.5 % of the measured range, Sensor implementations comparable to typical cameras are up until today limited in their temporal and spatial resolution, typically reaching only tens of fps and 0.01 megapixel resolution with few exceptions [24].

To use a TOF method, a special pair of projector and sensor is required. Until today, only few of these have been developed and their advancement is relatively low compared to normal cameras. Resolutions of 0.01 megapixel are typical at double digit fps, while accuracies of 0.5 % are common [24]. This is makes them impractical compared to simpler methods that often achieve similar measurement quality.

2.4.7. Digital holographic interference (DHI)

Digital holographic interference is a method based on measuring the phase of the light at the sensor produced by a single wavelength light source. Specifically, the interference of an object and a reference beam is recorded in a digital hologram created by an image sensor. Compared to a normal image, a hologram also contains the phase information of the incoming light. This phase information is obtained due to the interference of the two beams. The phase information of successive holograms can then be used to determine the deformation over a timestep.

Aguayo et al. [2] applied such a setup to the measurement of butterfly wing deformations. The used setup is shown in Figure 2.16, which is the typical out-of-plane DHI setup. A known, wavelength laser beam is split in a 50:50 beam splitter (BS). On part of the beam is redirected towards

a microscope objective, which spreads the laser beam to illuminate the object. From there it is reflected, and parts of the beam are bundled in an aperture (A) and lens (L) system, passing through the beam combiner (CM) into a high-speed camera. The other part of the beam is lead directly from the BS through and optical fiber (OF) to the BC and onto the high-speed camera sensor. In the camera sensor the two beams interfere and either cancel or enhance each other dependent on their relative phase.
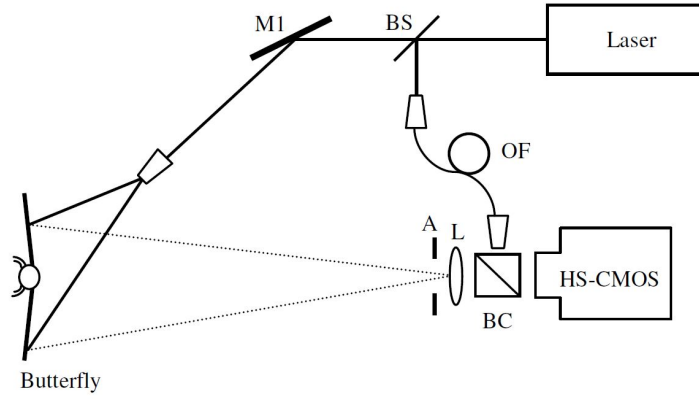
Figure 2.16: Holographic interferometry setup. [2]

The recorded hologram then has the general intensity

$$I(x, y) = |R(x, y)|^2 + |U(x, y)|^2 + R(x, y)U^*(x, y) + R^*(x, y)U(x, y), \tag{2.24}$$

where $R(x, y)$ and $U(x, y)$ are the reference and beam amplitudes and $R^*(x, y)$ and $U^*(x, y)$ are their complex conjugates.

The relative phase ϕ_n between two successive holograms I_n and I_{n-1} is then obtained by calculating the Fourier transform and the inverse Fourier transform. Then,

$$\Delta\phi_n = \arctan\left(\frac{Re[I_{n-1}]Im[I_n] - Im[I_{n-1}]Re[I_n]}{Im[I_{n-1}]Re[I_n] - Re[I_{n-1}]Im[I_n]}\right). \tag{2.25}$$

This process is similar to that of the FTP method explained in Section 2.4.3, and also here the obtained phase information still needs to be unwrapped. Here, this is done by a commercially available minimum cost matching algorithm.

From $\Delta\phi$ the displacement can then be determined using the known light wavelength λ:

$$\Delta\phi = \frac{2\pi}{\lambda}\mathbf{d}\cdot\mathbf{S}, \tag{2.26}$$

where $\mathbf{d}$ is the displacement vector in three dimensions and $\mathbf{S} = \mathbf{e}_0 - \mathbf{e}_i$ is the sensitivity vector dependent on the unit vectors of the light projected towards and reflected of the object [35]. As $\Delta\phi$ is known in each pixel, this also holds for d, thus the technique gives true full-field resolution.

Aguayo et al. [2] recorded megapixel images at 500 fps of the butterfly flapping. The timestep was therefore 2 ms, within which the local wings surface is displaced by up to 0.9 µm. The total deformation over the flapping cycle can be obtained by tracking the temporal changes starting from an initial known deformation. This limits the use of the method, as it depends on assumptions of the initial shape, e.g. a flat surface, and errors of the measurements will add up over longer measuring sequences. In Aguayo et al. [3] measurement sequences of 50 frames of different butterfly types are presented. The accuracy and resolution of these measurements were stated to be in the order of micrometers, which is around 0.01 % of the field of view or wingspan.

DHI methods use normal cameras and lasers, the setup must however be configured very carefully due to the nanometer scale of the measured wavelengths. Resolution and accuracy are however very good. The first being intrinsically full-field as the sine fringe method, while the second reaches values of 0.01 % [3], which is one order of magnitude lower than any other presented methods. Problematic is however that only the changes in displacement can be measured, this would require an accurately known initial state, something that is not trivial for highly flexible wings.

2.5. Literature review conclusions

The literature published on shape measurements of flapping-wings shows that optical methods are well suited for measuring the quickly deforming, complex shape of these wings. A table which compares the reached accuracy and spatial resolutions in different sources is shown in Table 2.1. Temporal resolution is not given in the table, as it is directly related to that of the used camera model. Values for accuracy and spatial resolution are given relative to largest object dimension, making this measure independent of the object size. The same holds mostly for the spatial resolution. Cameras with larger number of megapixel will thereby typically increase the achievable spatial resolution, as smaller, thus more structures can be captured.

Table 2.1: Accuracy and spatial resolution comparison. Percentage values are relative to largest object dimension, i.e. often wingspan or half wingspan

	Accuracy	Spatial Resolution
Point Tracking	0.2 % [47], 0.07 % [36]	122 [47], 25 [34], 200 points [36]
DIC	0.2 % to 0.6% [43], 0.13 % [57]	0.87 % [9]
Comb fringe	0.42 % [41], 0.26 % [51], 0.7 % [13]	100 - 200 [41], >10000 points [13]
Sine fringe	0.09 % to 0.12 % [30]	Full-field
Moiré	0.26 % [18]	Full-field
Structured Light	0.09 % [54]	0.55 % [54]
TOF	0.5 % [24]	Full-field
DHI	0.01 % [3]	Full-field

The achieved accuracy lies for most methods around 0.1 % to 0.2 %, which for the DelFly would correspond to around 0.15 mm. These methods all use modern variations of triangulation algorithms, which minimize the mean pixel error in the calibration process which directly relates to the mean error as Wallace et al. [49] showed. Outliers with much lower accuracy are comb fringe methods, which did not make use of advanced triangulation methods, and TOF methods, which rely on relatively new sensors. DHI in contrast reaches much better accuracies with around 0.01 %, making it the best solution according to the numbers as also the spatial accuracy is among the best.

The effectiveness of the spatial resolution varies greatly per method. Some methods, like sine fringe, TOF and DHI are intrinsically full-field, meaning they get a depth measurement value for each pixel. As the DIC pattern is continuous, the method can theoretically also reach full-field measurements if correlation windows are stacked with a single pixel offset, which is however very inefficient and adds little information. Comb fringe or Point Tracking meanwhile only obtain measurements at distinct markers, which reduces the spatial resolution considerably as the markers must have a relatively large size and spacing. This limits the minimum scale of deformations that can be captured. To obtain a continuous description for wings with sparse measurements, different interpolation methods were applied in literature such as B-splines [28] or cubic splines [47].

While DHI may be the best setup on paper, it relies on greatly on an accurate setup, which is quite complex by itself. This can make the method less favorable compared to other methods depending on the scope and requirements to the measurements. For the DelFly, the quality of the results acquired by Perçin et al. [37] were already quite pleasing, which means that a significantly improved quality may be secondary to simplicity and robustness of the setup. Other parameters that must be considered are the general suitability to geometry and material of the wings. Sine fringe relies on a predominantly matte, non-translucent wing which minimizes specular reflections while DIC requires a specific texture. Other specifics of the measurement setups are also relevant, for instance the measurable flapping range. Thereby it should be noted that techniques can be combined to extend their functionality, e.g. Wang et al. [51] added a Point Tracking method to their PCF approach to measure body attitude. as Lastly the availability of the measurement equipment must be considered. Expensive equipment may not be available and can be disproportionate to the general project scope.

Generally, many of the presented methods are considerable and relevant for measuring flapping-wing deformations. The relative simplicity and low requirements to wing surface properties of Point Tracking makes it still an attractive measurement technique, especially as the modern applications tend to reach decent spatial resolution [37]. DIC is also a promising technique, as it allows full field measurements while having a robust matching algorithm. Downsides are however the larger requirements to the wing surface texture. This can for instance be avoided by replacing one camera by a Structured Light source, for example a relatively simple projector.

These three methods were chosen for short preliminary tests, presented in Chapter 3, with the purpose to a get sound understanding of the specific functioning when applied to the thesis objective. Other methods such as sine fringe, DHI or TOF were not chosen as the specific measurement equipment was not available and too expensive to acquire, and furthermore tended to be too complex to implement from scratch to fit the scope of this project.

3

Assessment of measurement techniques

To better determine if a measurement technique is suitable for measuring the DelFly wing deformations and whether a robust method can be developed, it was chosen to carry out short trial measurement campaigns. Achievable certainty was secondary to this, as realistic assessments would require much longer trial periods and can instead be made based on the discussions in the literature review.

The methods choosen for further investigation were Point Tracking, DIC and a simple Structured Light correlation approach. All of the chosen methods are therefore in principle triangulation based, which allows them to have a similar setup, discussed in 3.1. The only difference is the way pixel in the different views are being matched, and the effects on the imaging properties. The Point Tracking is treated first in Section 3.2, followed by the DIC approach in Section 3.3 and lastly by a Structured Light approach in Section 3.4.

With the knowledge of these initial trials and the previously carried out literature study, the optimal measurement technique to acquire the final results is selected. This is done using a trade-off study presented in Section 3.5.

3.1. General measurement setup

The trial campaigns studied a simple hover case with a flapping frequency of 8 Hz, which was chosen to reduce the measurement difficulty and the wear of the model due to high loads, while still maintaining the general characteristics of the model. Typically, only the wing closer to the cameras was measured, which limited the algorithm complexity while still giving insights to what measurement setups are feasible for measuring both wings.

The used DelFly model consists mostly of only the wing and driving mechanism, explained in detail in Section 4.1.1. All measurements use an identical base setup where the model is mounted on its side on a frame, so that a top view is easily recorded using horizontally mounted cameras. All tests use high-speed Photron Fastcam SA 1.1 cameras, positioned at a 30° stereo angle. Figure 3.1 shows the basic arrangement, here for the DIC measurements, which has an additional lamp added on the camera side. The cameras were calibrated with the MATLAB stereo camera calibration app using arbitrarily orientated checkerboard patterns, which gives all relevant parameters for the camera models.

3.2. Point Tracking

For the first trial campaign, discrete markers are added to the wing which are then matched between camera views and tracked in time to measure the wing shape deformation. Additionally,
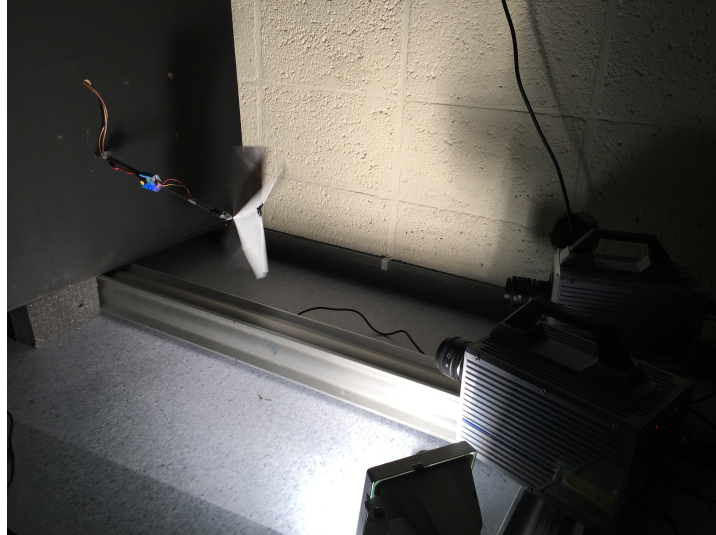
Figure 3.1: Basic trial test setup schematic

approaches were the wing stiffeners are tracked plus additional lines on the wing trailing edge, using an approach similar to that by Walker et al. [47] were considered and tested. While promising, a successful implementation was not achieved in time.

3.2.1. Measurement procedure

For the Point Tracking setup, a background illumination approach similar to the one by Perçin et al. [37] was chosen, as this prevents any specular reflections of the wings. Therefore, a white background was added to the basic measurement setup, which was illuminated by a 1 kW halogen lamp. Different point sizes and patterns were tested, ultimately points with approximately 2.5 mm radius spaced at 15 mm × 15 mm as shown in Figure 3.2 were used. The additional weight of points applied to a wing half was not consistently measurable on a scale with ±0.02 g resolution.

The recorded images are further improved by some initial image preprocessing to increase the point visibility. These steps included background removal using a separate recording and thresholding, to obtain binary images. The raw and preprocessed images are shown in Figure 3.2.

The following Point Tracking algorithm is built around a simple circle finding method together with a finite difference velocity calculation:

Initially, all points must be found in both camera views. Therefore, the known wing point locations are used, which multiplied by a camera magnification factor gives the approximate point spacing in pixel. The approximate location of an easily recognizable point (e.g. a corner point) is then selected manually in the starting image of each view where the wing is approximately orthogonal to both cameras, i.e. during the end of the in-stroke. The algorithm then searches a local search window for points using the default circular Hough transform method build into the MATLAB function `imfindcircles` and selects the closest point is selected as a match. All remaining points are found sequentially by searching around a prediction relative to the prior point. Once all points are found in both views, they are triangulated using the MATLAB DLT implementation [23] to obtain the world point locations.

As the points do not have any distinctive features, their location is tracked using temporal information. Point movements between frames are assumed to be small, therefore for the second timestep the location is simply assumed to lie closely around the measured location in the first timestep. From the third timestep onward, the image point velocity is calculated using a backwards finite difference method, which is then used to predict the subsequent location. After each timestep

(a) Raw image   (b) Image after preprocessing
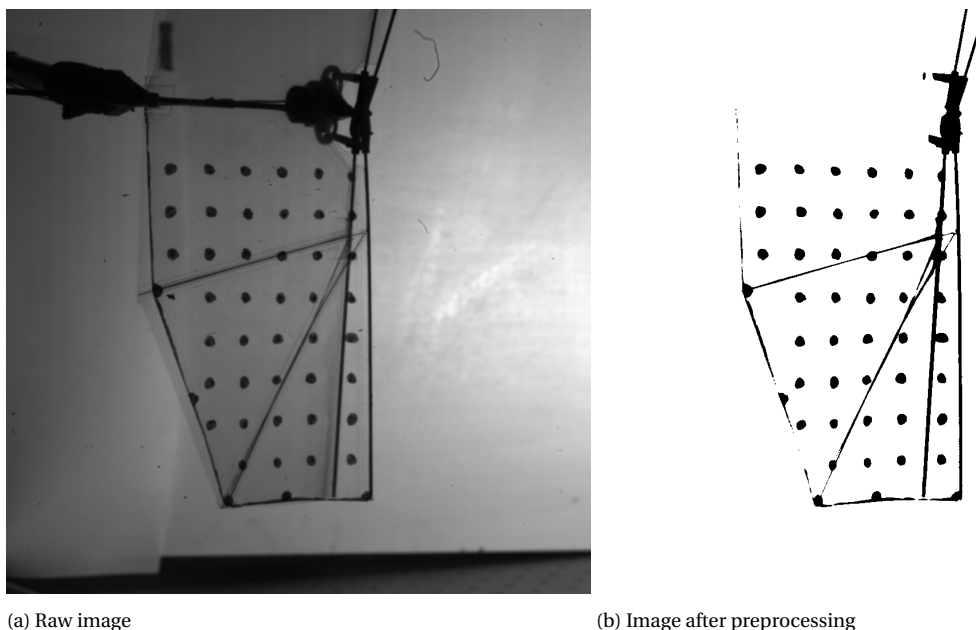
Figure 3.2: Sample images from Point Tracking trial measurements.

points are again triangulated to give the world point locations.

Apart from this MATLAB implementation, it was also attempted to use the Shake-the-Box algorithm [39] of the LaVision software DaVis. However, while the software also works with a stereo setup, for successful point identification three cameras or more are necessary. The presence of wing stiffeners in the images, and high distortion of the planar points are also likely to prevent good tracking.

3.2.2. Performance and possible improvements
The large points allowed a robust working of the CHT algorithm although points are partially occluded by the wing stiffeners at some instances. As an example, the upper right point in Figure 3.2 is still correctly identified.

Once the correct magnification factor is estimated, points are successfully found in the first timestep. The resulting wing shape appears to be accurate, with an average reprojection error of 0.25 pixel over the 42 points. For the consecutive timesteps, the location prediction works quite well, with a prediction error of around 1.5 pixel for recordings of both 1 kHz and 2 kHz, which lies well under the point spacing. As a result, the matching is successful, and the wing shape is accurately measured.

However, typically after around 10 to 20 timesteps, some points are lost. This is mostly due to poor imaging conditions, as well as due to larger occlusions, for example of multiple wing stiffener. Furthermore, noise in the velocity measurement due to inaccurate point center location finding leads to lost points. Once points are lost, they are typically not found again, as no method to detect false identifications is implemented. Furthermore, lost points can accidentally be matched with other points due to the purely sequential approach. All these limitations typically result a completely deteriorated wing shape after around 50 timesteps, around a quarter of a flapping cycle, where only few correct points remain.

In addition to the single wing measurements, some trials were done were points on both wings

were tracked. This poses a great benefit of this method, as theoretically no additional hardware is needed to measure both wing halves per side. However, while the points are placed so that they do not overlap during the contact phase, point occlusions between both wings are not preventable for all phases, which means that points are now lost at an even faster rate and false matches are more frequent.

Nonetheless, considering the crudeness of the algorithm, the Point Tracking method appears to work relatively decently. Many points of improvements exist, the largest is possibly the potential of using the known point spacing to create an additional spatial prediction. This should allow consistent matching of points event with only two cameras. Other improvements could be a better temporal prediction by filtering noise in the location measurements and better image preprocessing.

3.3. Digital Image Correlation

Within the second trial campaign, a DIC method was tested. This approach replaces the discrete points from the previous section by a continuous pattern. A potential advantage of this is the robustness of matching image locations using correlations. These locations again give the 3D wing shape using triangulation. Apart from an own MATLAB implementation, processing was also done using the commercial DIC software StrainMaster from LaVision.

3.3.1. Measurement procedure

Several different patterns were tested, some applied using special paint rollers, others by sprinkling paint. The tested patterns were thereby applied onto a white base coat to achieve a high contrast. In principle a background illumination technique would again be possible for a single wing, however when measuring both wings simultaneously the patterns would overlap and be close to indistinguishable from another. Therefore, the white base cote is applied, which adds around 0.1 g to 0.2 g per wing half depending on the thickness of application. Sample recordings of different tested patterns are shown in Figure 3.3. The 1 kW halogen lamp now illuminates the wings directly, specular reflection is however limited due to the matte paint finish.

(a) Large roller pattern.   (b) Small roller pattern.   (c) Dense paint sprinkles.   (d) Sparse paint sprinkles.
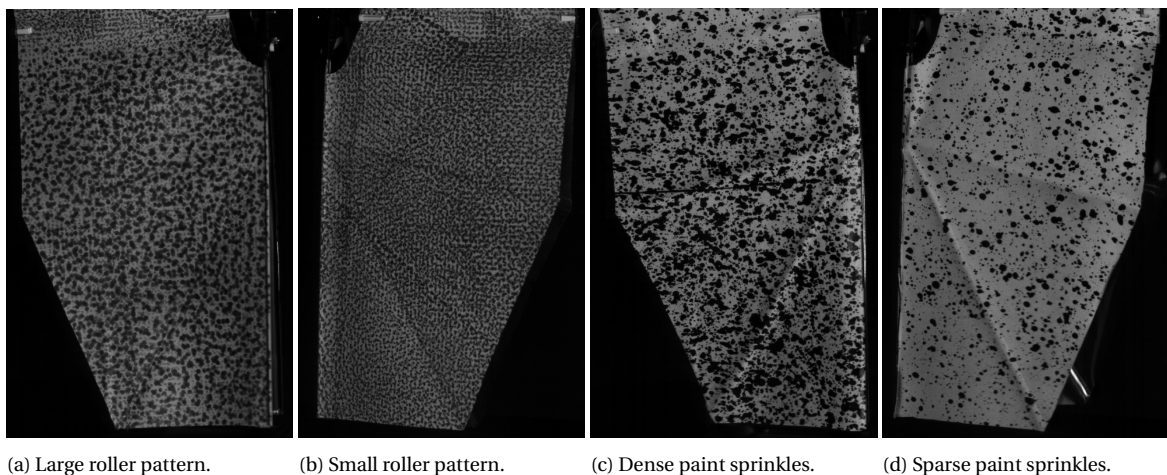
Figure 3.3: Sample images showing different pattern applications for DIC trial measurements.

For the MATLAB DIC implementation the recorded images were again preprocessed to improve the pattern contrast. These steps included masking, local contrast enhancement using the `adapthisteq` MATLAB function, and again thresholding to obtain binary images.

The MATLAB algorithm then uses a differential correlation process: Initially the algorithm matches wing locations between both views by correlating both initial images of the wing contact phase. The correlation matrix was obtained using the `xcorr2` MATLAB function, plus an additional sub-pixel correlation peak finding by optimizing a cubic fit of the correlation matrix. Distortion of the recorded patterns due to the different viewing angles was not considered. The matched points are then triangulated using the MATLAB DLT implementation [23].

For the following timesteps, the matching correlation was performed between the consecutive timesteps, separately for both views. This procedure proved to be the most successful in preventing bad matches, as pattern distortion between images is mostly eliminated here. However, as correlation is no longer performed over the two views, some drift in the determined pattern location still occurs, which results in an over time increasing triangulation error.

3.3.2. Performance and possible improvements

Despite this phenomenon, decent results were obtained. Overall, the large roller pattern shown in Figure 3.3a recorded at 1 kHz with a 50 pixel × 50 pixel window size performed best. Using a 50% window overlap, 443 measurement points that have a minimum signal to noise ratio of 1.1 are found initially. This number drops slightly to an average of 433 points over the first cycle half, with an average triangulation error of 1.1 pixel. Around 50 measurement points are lost at the stroke reversal, likely due to the fast pitch rotation of the wing. For the rest of the second cycle half the number of found points remains almost constant at around 380 with an average triangulation error of 1.2 pixel.

The short processing trials using StrainMaster also show promising results. Here, the differential correlation process also shows the best results for the large deformations, giving a robust measurement for the large roller application. However, it appears like relatively large smoothing and interpolation is applied, for instance the leading edge tip is heavily bend in the measurements, which cannot be correct due to the leading edge stiffener.

Apart from that, DIC appears to work decently also with the large deformations of the DelFly wings. StainMaster would give usable results almost directly, limitations are only the unknown accuracy of the results, and a necessary method to detect the wing boundary. The MATLAB implementation performs also quite well, some points for improvements could be reduction of the correlation window drift.

3.4. Structured light

For the Structured Light implementation, a relatively simple correlation-based method was chosen. The approach is somewhat similar to that of the DIC implementation, only that now the correlation pattern is now projected onto the wing by a light source which replaces one of the cameras. Triangulation using a DLT approach would still be possible using camera models for both projector and camera, however for simplicity here an approach using reference plane recordings is applied.

3.4.1. Measurement procedure

The Structured Light was projected using a simple off-the-shelf projector with a specified brightness of 1800 ANSI lumen, 2000:1 contrast ratio, and a resolution of 1024 pixel × 768 pixel. The projector was set to project images of a random dot pattern. Binary intensity settings were chosen, as here the micro-mirrors of the DLP projector are theoretically continuously in either on or off position, thus preventing flicker of the projection. While Gong and Zhang [19] successfully used such a configuration for a sine fringe projection, here a flicker with 120 Hz and higher harmonics still remained,

possibly due to wrong projector settings or wrong source format. Nonetheless, recordings were carried out, however with varying quality for higher recording rates.

To minimize specular reflections and increase contrast, the wing was painted matte black. An example recording is shown in Figure 3.4a, where the wing was static. It can be seen that the projected pattern has large fluctuations in intensity, especially around the wing stiffener regions. Together with the light flicker, this prevented successful measurements of a moving wing.
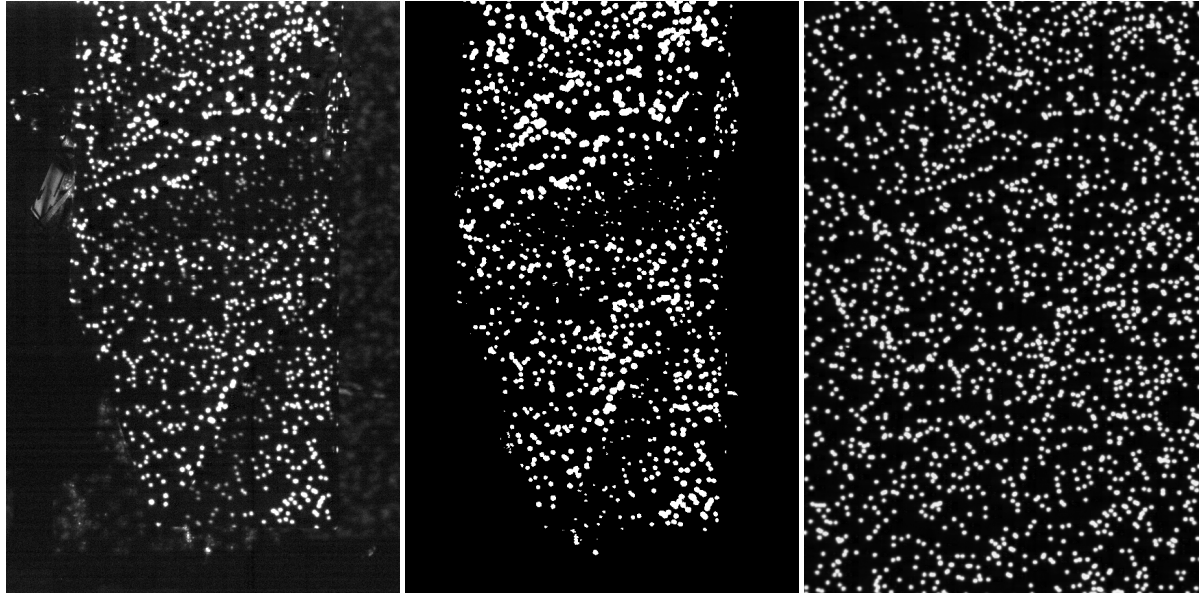
(a) lower 16th intensity percentile of raw wing recording.   (b) Preprocessed wing recording.   (c) Reference plane recording.

Figure 3.4: Sample images of Structured Light trial measurements.

Later tests of different wing materials showed that a matte white wing may give improved pattern quality due to increased intensity. Clear wings also reflect a considerable amount of light, especially when the finish is slightly matte. Quick tests showed a similar reflection of light compared to black wings and up to 50 % of light compared to a white wing.

After importing, the images are preprocessed using masking, local contrast enhancement, and thresholding. A resulting recording is shown in Figure 3.4b.

The wing shape is then determined in form of a depth map. Therefore, two reference planes spaced a known distance apart were initially correlated using the procedure explained in Section 3.3.1. This gives the ratio between depth and pixel shift $\frac{dZ_{ref}(x,y)}{dpixel}$, which is subsequently used to determine the wing depth map. Therefore, the wing recordings are correlated with one of the reference plane recordings, where the correlation regions are limited to a region following the reference plane shift, effectively making use of the euclidean geometry. The wing depth map is then simply determined as $\Delta Z(x,y) = \frac{dZ_{ref}(x,y)}{dpixel} \Delta pixel(x,y)$.

3.4.2. Performance and possible improvements

Results obtained by this crude Structured Light implementation were of limited quality. Even after preprocessing the recordings had large intensity gradients in the pattern which prevented robust correlation. This can be attributed to the chosen black wing surface and remaining specular reflection. Furthermore, the projector refresh rate prevented low exposure times, resulting in consider-

able blur and making high-speed recordings impossible. It remains difficult to judge how easy these problems are solved, it is likely that a more specialized light source is necessary.

The simple depth calculation method showed to work relatively well, giving an average error of around 4.5 % when measuring the location of a third reference plane. The conversion of X and Y image locations to world coordinates was not considered. In a final implementation a triangulation approach should be used for increased robustness.

3.5. Trade-off study

While the outcome of the preliminary tests varies greatly, they generally showed that with certain improvements all tested methods could allow successful measurements of the wing deformations. However, the quality of measurements may be considerably different, as well as the amount of work necessary to develop the setup.

To be able to form the best decision between which method to use for the wing deformation measurements, it was decided to carry out a trade-off study. Therefore, several different measures were selected and applied with a specific weight, and a grading from 1 to 10 was given to each method, shown in Table 3.1. Weight selection and grading were carried out as objectively as possible, however as the process is not entirely based on numeric measures it may not entirely immune to subjective grading.

Table 3.1: Measurement technique trade-off table

| | | Point Tracking | | DIC | Structured |
Measure	Weight	Opaque	Clear		Light
Intrusiveness	30%	4	9	4	4
Accuracy	15%	6	6	5	5
Resolution	15%	6	4	8	8
Setup Complexity and Preparation	15%	5	8	5	4
Development Effort and Risk	25%	7	4	8	5
Total	100%	5.5	6.4	5.9	5.0

3.5.1. Considered measurement setups and measures

The methods considered in this study are the three from the preliminary tests, with two different setups for Point Tracking. As stated above, other active techniques such as fringe methods or time delay methods were not further considered for the measurements, as the setups and processing techniques are of relatively high complexity and are likely to extend the scope of this project, especially considering the limited amount of practical knowledge available. Thus, the considered measurement setups are essentially those explained above, however expanded to measure the deformation of both upper and lower wings. As DIC and Structured Light approach require opaque wings, their setups require a second view of the lower wing. This means either a second camera and light setup is necessary on the lower wing side, or the cameras must be moved to the lower wing side for a second recording which are then stitched together in the processing. Point Tracking however allows the use of transparent wings, therefore the lower wing pattern can simply be recorded through the upper wing, requiring only a single sided camera setup. As this however increases the complexity of correctly tracking the points and allocating them to the correct wing, also a two-sided setup with opaque wings is considered. In theory, wing transparency could also be exploited for single sided DIC or Structured Light measurements. For instance in experimental flow measurements volumetric correlation methods exist that could allow to correlate overlapping patterns of both wing pairs.

However, the used algorithms are highly sophisticated and often require considerable computing power [38], which puts them outside the scope of this project.

Five different measures were selected to rank these setups. The first is intrusiveness, which is generally low as all approaches are optical. However, all methods considered require some modification to the wings, where the added texture may alter the structural properties considerably. As the carried out measurements shall be comparable to earlier DelFly measurements, it is of large importance that the wing properties resemble previous measurements as closely as possible. Therefore, the weight is selected as 30 %.

The next measures are accuracy and resolution, which are both weighted with 15 %. These are graded based on the previous literature study, with some considerations for the specific setup used here. General aim is thereby to achieve a result comparable with the previous study by Perçin et al. [37].

Apart from these measures which mostly define the quality of the measurements, also the effort of obtaining the measurements is considered. This includes the setup complexity, which is determined by the used equipment, and the estimated preparation time (model preparation and setup assembly). This measure is weighted at 15 %.

As stated before, accurate measurement techniques often require sophisticated setups, which may exceed the scope of the project, considering that a large part is allocated for processing and analysis of the results. Therefore, the effort it takes to setup a working method, and the risk that the developed method does not allow successful measurements, or requires considerable manual input during processing, is considered as the last measure. The allocated weight is 25 %.

3.5.2. Grading

For intrusion, the grading of the method is predominantly driven by the added weight to the wings. Tests of different paint applications showed thereby that the wing properties changed considerably once an additional 50 % of weight is added compared to the wing surface material, weighting 0.46(2) g for one wing. 0.23 g added weight is therefore graded as 1, with the rest graded linearly to a 10 at zero added weight. A coat of paint thick enough to obscure most light weighs approximatly 0.15 g, giving all measures with opaque wings a grade of 4. The clear Point Tracking method is graded as 9, as the added weight lies within the scale measurement resolution of 0.02 g.

The highest measured accuracies of the selected methods in literature all lie closely together and are all reasonable for the DelFly measurements. This is sensible, as all rely on similar triangulation techniques, and only differ in the point matching and tracking methods. Point Tracking was graded slightly above the other methods, as had a marginally higher values in literature. While DIC has the worst accuracies in literature, it showed the best results in the preliminary studies, and is therefore graded identically with Structured Light.

Resolution of DIC and Structured Light is theoretically full-field and are therefore graded high. Point Tracking has only a limited resolution, however hundreds of measurement points are achievable, which is already reasonable. With transparent wings, it is however likely that the number of points per wing is approximately halved as points occlusion will become regular, therefore it is ranked lowest.

Setup complexity is however considerably reduced for the transparent Point Tracking approach, as only a single sided setup is necessary. All other methods require a two-sided setup, with the Structured Light setup requiring specialized light sources, and a specialized calibration method, which makes it the most complex method. Furthermore, wing preparation is increased for the opaque methods, and is especially high for DIC and Point Tracking as a pattern must be applied.

With the preliminary studies carried out, a relatively good estimation of the further development effort for each method can be made. The DIC approach using StrainMaster showed thereby to

be a very straightforward approach, with results for flapping multiple cycles already obtained. Point Tracking also showed reasonable results and should also be relatively straightforward to implement on an opaque wing, using the point spacing to prevent temporal tracking errors. Using a transparent wing with both wing patterns moving relative to each other in the camera views will require considerably more work and is more likely to require manual corrections. The results obtained by the Structured Light measurements were worst, however some modifications should result in large improvements in imaging quality, which should reduce the risk of unsuccessful measurements.

Overall, the trade-off study shows that Point Tracking using clear wings is the most suitable method for measuring the DelFly wing deformations. This is predominantly due to a low setup complexity, and only minimal changes to the wing structure, which justifies the additional development effort compared to the opaque wing setup. A DIC approach would be the next best choice with very high resolution and the lowest development effort, the latter suggesting its use over a Structured Light approach.

Therefore, for the final measurements a Point Tracking method will be used. In the following section the developed setup and processing algorithm is discussed in more detail.
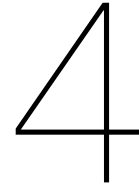
Measurement procedure

With the decision formed to use Point Tracking with background illumination to measure both wings simultaneously, a suitable measurement setup and point tracking algorithm must be selected. The approach of the preliminary study was therefore extensively improved to allow for two wing measurements, while increasing quality and robustness. The final measurement setup and point tracking algorithm is discussed in Section 4.1 and 4.2, respectively, and an estimation of the performance and a verification is carried out in Section 4.3.

4.1. Measurement setup

In the final measurement campaign the DelFly is mounted in a windtunnel, which allows to simulate different flight conditions by varying freestream velocity direction by changing the windtunnel setting and rotating the DelFly. This requires several adaptations of the preliminary measurement setup as accessibility is limited, which are discussed in the following sections.

4.1.1. DelFly model

The used DelFly consists of only the central fuselage, the flapping mechanism including BLDC motor and ESC, and the X-wing pair as shown in Figure 4.1. Similar as in other tethered studies of the DelFly, the tail is omitted. The electrical power is supplied externally using a laboratory power-supply and the PWM signal controlling the flapping frequency is supplied by a simple servo tester. A comprehensive description of the design of the DelFly II is done by de Croon et al. [12].

The wings used in this model are the current standard configuration with a half span of $r_{tip} = 140\,$mm and mean chord of $c_{mean} = 80\,$mm, shown in Figure 4.2. The wing pairs have a 12° dihedral angle and rotate around an axle just above the fuselage. The wing surface material is $15\,\mu$m thick Mylar weighing $20.4\,$g m^{-2}, which results in a weight of $0.23\,$g per wing half. The material is supported by the default carbon stiffener setup [21] to which it is attached using stickers. The leading edge stiffener has a half circular shape, where the circular part is oriented forward, so that the maximum width of $1.4\,$mm is oriented in the stroke plane, increasing the stiffness in this plane. The smaller stiffeners are circular with a diameter of $0.28\,$mm. Together, this comes to a half wing weight of approximately $0.59(1)\,$g.

The tracked points are applied on the wing using a permanent marker. Per wing, a total of 136 black markers of approximately 1 mm radius spaced in a $7.5\,$mm $\times 10\,$mm grid are applied. The grid is shifted between the upper and lower wing, so that overlapping of points during the contact phase is avoided. The marker position is exact to approximately 1 mm, this has however only very little
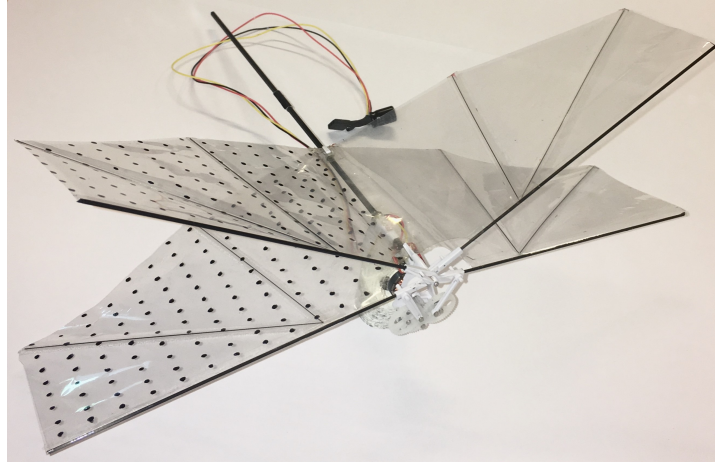
Figure 4.1: Used DelFly II model.
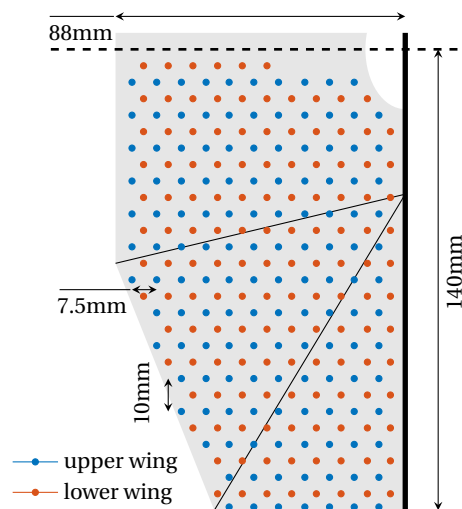
Figure 4.2: Schematic of DelFly wing half with point grids.

influence on the measurement process, with the largest effect being if the final wing outline is to be determined.

The fuselage is a square 2 mm × 2 mm carbon rod. The length was kept at around 200 mm length, which simplified the alignment. A marker was added to the fuselage to determine its orientation in the wing point recordings using the wing trailing edge tensioner as second marker. A 3D printed adapter is attached to the air frame below the quarter chord of the wings to mount the model to the measurement setup. The driving mechanism is mounted at the front end of the fuselage. This consists of a mount for the motor, a reduction gearbox including push rods, and a mount for the wing axle. The push rods are connected to the wing swing arms and allow stroke angles of $\phi = 44°$. The motor is a custom build brushless direct current (BLDC) motor with 28 windings and an internal resistance of $1.5\,\Omega$, operated at 4 V. The rotation frequency of the motor, and thus the flapping frequency, f, is controlled using an electronic speed controller (ESC), which in turn receives its input pulse width modulation (PWM) signal supplied by a servo tester. The electrical power is supplied by a laboratory power supply, after which a capacitor is added to further smooth the provided power.

The maximum continuous current draw of the motor is 1 A measured at the power supply. This

allows a maximum flapping frequency of around 15 Hz in stationary conditions. However, f also varies with the freestream, which makes the adjustment not straightforward with this simple setup. Therefore, during the measurements the current was first set to an initial estimate for a first recording. This recording was then inspected and a flapping frequency calculated based on the recording rate and the number of images it takes to complete three flapping cycles. Based on this, the current is adjusted, and the process is repeated until f is set to within 1 % of the desired value.

4.1.2. Stereo setup and pitching mechanism

The measurement setup used for the final campaign was limited to two cameras. Other high-speed cameras turned out to be defective at the start of the measurement campaign and no replacement was available in time. Generally, this is not a severe limitation, as the initial studies showed that measurement of the wing deformations were also possible with a single camera pair, and in fact the setup complexity was also a consideration in the method selection process. However, the importance of the correct viewing angles of the DelFly wings was already noted during the preliminary test series: all points had to be continuously identifiable in both camera views as no third view is available. This means both cameras must be positioned above or below the X-wing pairs, here the former is chosen. Furthermore, as the wing surfaces rotate heavily around the wing leading edges, the wing surface quickly becomes parallel to the viewing axis of one camera, thus the exact viewing angles must be selected carefully. The wing rotations commonly reach values of ±45° per wing [37], and showed to limit the camera position to an angle of ±20° from the stroke plane before points became indistinguishable from another.

This implication requires the cameras to be fixed relatively to the DelFly as the setup is rotated. It was therefore chosen to mount DelFly and cameras to a single frame, which is rotated to achieve different pitch settings. This however introduced another limitation to the viewing angles: at very large pitch angle settings (the maximum pitch angle to be measured is $\theta_b = 70°$) the cameras will start to enter the freestream with the DelFly model moving in front of the windtunnel in the camera views. This must be avoided, as it leads to flow disturbances and insufficient background illumination which would prevent successful measurements. Therefore, no camera could be mounted behind the DelFly viewing forwards, in other words the hind camera had to be exactly above the DelFly.

Therefore, the viewing angels are now limited to 0° and 20° from the y_b-z_b plane, thus the stereo angle is limited to 20°. This is a relatively narrow angle, limiting the out of plane measurement accuracy. Nonetheless, reference case measurements show still decent accuracy, see Section 4.3.2, and similar stereo angles are is still commonly used in comparable applications [40].

Figure 4.3 shows a sketch and picture of the used setup. To simplify the setup, the DelFly is mounted on its side, therefore the pitching mechanism could be positioned on the floor under the center of the open windtunnel test section, approximately 1.1 m from the nozzle. The sideways orientation, and therefore untypical orientation of gravitational forces, is assumed to have negligible influence as acceleration forces due to the flapping are considerably larger as shown in Section 5.1.5. The used rotation mechanism is designed for the use on a milling machine, thus provides excellent stiffness and precision. Due to minor play in the connection, the accuracy of the pitch angle is assumed to be around ±0.1°, which is very good considering the large pitch angle range. On the rotating stage a rectangular frame of 2 m × 1.5 m is mounted. The DelFly is connected to one side, positioned so that the quarter wing chord is exactly over the rotational axis and at 10° pre-pitch relative to the plane of the frame. This allowed the cameras to be mounted symmetrically on the other side of the frame. As the cameras are rigidly mounted to the frame, and no adjustments were

necessary with changing pitch angle, the camera pair only needed to be calibrated once, which considerably reduced the time needed to measure a sweep of pitch angles.
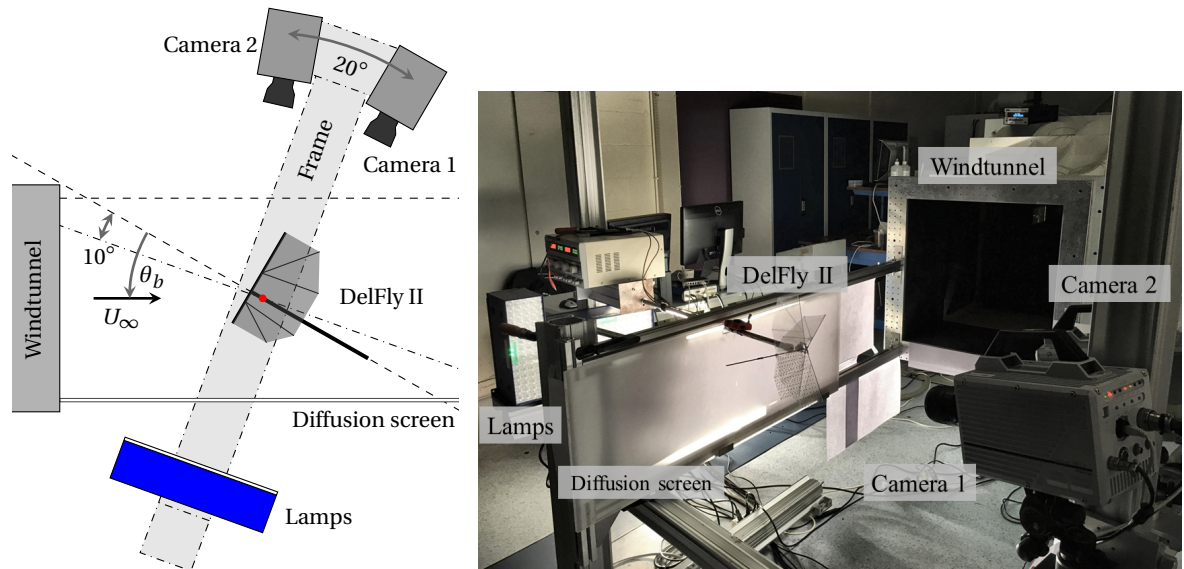
(a) Top-down sketch on the test section with the DelFly pitched with θ_b around the rotation axis (red).

(b) Picture of the measurement setup showing the DelFly mounted in front of the windtunnel nozzle.

Figure 4.3: Measurement setup.

4.1.3. Other measurement equipment

The windtunnel used for the measurements is the W-Tunnel in the high-speed laboratory of Delft Technical University. This is an open jet tunnel, which is fitted with a 600 mm × 600 mm nozzle with a contraction ratio of 3.62. The revolutions per minute of the centrifugal fan control the flow velocity, U_∞, which is measured in form of the dynamic pressure, q by using a pitot tube positioned at the end of the contraction. Dynamic pressure is then calculated to flow velocity as

$$U_\infty = \sqrt{\frac{2q}{\rho}},$$

(4.1)

where air density, ρ is determined from air temperature, T and air pressure, p measurements and the gas constant, R as

$$\rho = \frac{p}{RT}.$$

(4.2)

The dynamic pressure measurements however fluctuate considerably at the low freestream velocities at the free flight of the DelFly, making precise velocity settings impossible. Martínez Gallar [32] therefore measured the flow velocity for different fan settings using planar particle image velocimetry (PIV) in her studies. These settings were again used for measurements where $|U_\infty| < 1\,\mathrm{m\,s^{-1}}$. The maximum turbulence intensity was determined to be 1.6 % [32]. No windtunnel corrections were applied as no analytical descriptions exist for the complex wake interactions of the flapping wings at large pitch angles.

As described above, the cameras are set to a 20° stereo angle. Specifically, they are positioned around 600 mm from the DelFly in a plane orthogonal to the dihedral angle. The used cameras are two Photron Fastcam SA 1.1 with a gray level 12 bit complementary metal oxide semiconductor

(CMOS) sensor with a 1024 pixel x 1024 pixel resolution and 20 μm pixel pitch capturing at 2 kHz and 1/2000 s exposure. The cameras are fitted with a Nikon lens with 60 mm focal length and $f\# = 16$, mounted on a Scheimpflug adapter which aligns the focal plane with the dihedral plane. These settings were determined during a dedicated test series and showed to give the best compromise of captured light intensity, depth of field and motion blur.

Three LaVision LED-Flashlight 300 lamps are selected for illumination, having a combined light area of 0.09 m^2 and a 10° opening angle. The lights pulse in synchronization with the cameras with 10 % duty cycle, resulting in an average power consumption of 300 W. As done with the cameras, they are also mounted to the frame.

Although the lamps produce a relatively large and homogeneous light area, they are further diffused using a combination of paper and a frosted acrylic screen to achieve an even background illumination. The acrylic screen slides together with the DelFly support, which runs through a slot in the screen. The screen is thereby mounted in line with the windtunnel contraction, covering approximately the lower half of the shear layer behind the DelFly model. This partial closing of the test section will have a minor influence on the measurements, for instance due to pressure reflections in that area. The resulting intrusion was minimized as much as possible by trimming the screen so that the wake does not interact with the diffusion screen, but directly exits the shear layer.

Cameras and lights are addressed using the LaVision software DaVis running on a PC. This allowed synchronization using a connected high-speed controller. After recording, the images are exported as 16 bit TIF files.

In total, this setup allowed to measure most of the wanted settings without requiring any modifications. The only exception is that for $\theta_b \geq 50°$ an additional 1 kW halogen lamp is added on the camera side of the windtunnel. This lamp illuminates the windtunnel contraction area and diffusion screen, as this region is not reached by the background illumination.

4.2. Point tracking algorithm

For the point tracking algorithm, the preliminary code explained in Section 3.2.1 was completely rewritten to an object-oriented structure and expanded. Generally, the code follows the flowchart shown in Figure 4.4.

Initially, the algorithm loads different settings from an initialization file, such as the approximate flapping frequency, the calibration series, the used point spacing and starting frame and other settings. The starting frame must be chosen manually to an instance where the wings are in contact, as here they are mostly orthogonal to the camera views and the points are not overlapping.

Once loaded, some classes are initialized using the settings. This includes for instance the recording object, which then contains the camera calibration parameters, explained in more detail in Section 4.2.1.

After this, the point tracking algorithm starts, looping in time over the recorded image pairs. The image point tracking is thereby split into two parts: On one side the image is preprocessed and points are identified, explained in Section 4.2.2, and on the other the point locations are predicted, explained in Section 4.2.3. These two steps are then linked in the point correspondence step, explained in Section 4.2.4, where the measurements and predictions are matched to give the exact image point locations over time. The matching step is concluded with the determination of several properties such as velocities and statistics which are determine the certainty of each point measurement, represented by different status.

Figure 4.4: Point tracking algorithm flow chart. Blue dots indicate sections were points are explained. Grey coloring shows the initial timestep, dashed lines represent additional steps for uncorresponded or poorly measured points.

The image point locations are then triangulated to give the world point locations. As found in the preliminary studies, unsuccessful point tracking can quickly lead to incorrect triangulation. Therefore, the world locations are checked using a spatial fit, where outliers are assigned with an according status and attempted to be corrected, as explained in Section 4.2.5. Again, more properties and statistics are calculated after the determination of the world point locations.

Once the complete recording series is processed, a final postprocessing algorithm is run. As the wing flapping is cyclic, and conditions are assumed to be steady, it is assumed that the results do not vary over multiple cycles. Therefore, in the final results only the average shape over the

entire measurement sequence is considered, and the point measurements are concentrated into a single cycle. This process is explained in Section 4.2.6, together with the calculation of several airfoil parameters.

4.2.1. Camera calibration

Camera calibration is done using the MATLAB stereo calibration toolbox, which is based on the theory introduced in Section 2.2. Therefore, several calibration image pairs (here around 16) are taken of a 6×8 checkerboard plate with a 14.55 mm grid size placed in arbitrary orientations in the approximate measurement volume. The grid intersections are accurately measurable using the Harris corner detection implemented in the `detectCheckerboardPoints` MATLAB function. These image plane locations and the checkerboard spacing are then inserted to the calibration function `estimateCameraParameters`, which determines the intrinsic and extrinsic matrices and distortion parameters of the stereo setup, taking the tangential distortion due to the Scheimpflug adapter into account. These parameters resulted in a 0.09 pixel mean reprojection error, which can be considered to be very good.

4.2.2. Image preprocessing and point finding

Several preprocessing steps are carried out to improve the point detection algorithm. First, the background is removed from the raw image shown in Figure 4.5a. This is done by subtracting the mean intensity of 100 separately recorded background images from the recording intensity and cropping the intensity range to the negative region. This leaves only pixel that have a lower intensity in the recording than in the background image, which due to the background illumination are mostly those of wing points. Other image features, such as parts of the measurement frame, the DelFly fuselage, light gradients and even minor texture of the diffusion screen have approximately the same intensity in both images, and therefore have zero intensity in the resulting picture. The negative intensity range is then rescaled to a range between 0 and 1, giving the image shown in Figure 4.5b.

(a) Raw image   (b) Background removal   (d) Gaussian smoothing   (c) Inversion   (e) CHT point finding
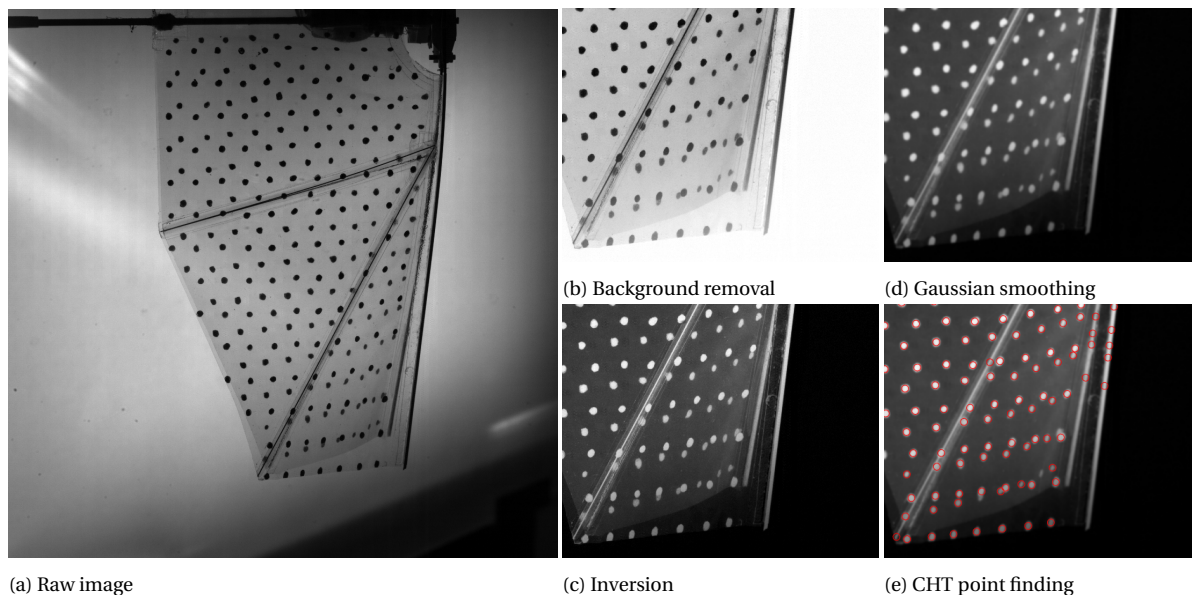
Figure 4.5: Image preprocessing steps

This image is then inverted (see Figure 4.5c) to work with the default settings of the MATLAB point finding algorithm.

Next, the image is smoothed using a 7 pixel × 7 pixel gaussian filter implemented in the `imgaussfilt`

MATLAB function, which reduces noise and showed to make point contours easier to detect by the point finding algorithm (see Figure 4.5d).

As final preprocessing step the image distortion is corrected using the individual camera parameters determined in the calibration step.

This preprocessed image is then used for point finding, using the Circular Hough Transform (CHT) method implemented in the `imfindcircles` MATLAB function. At the core, CHT methods finds points by detecting candidate edge pixel with high gradients, which are assumed to lie on a circle described by

$$(x - a)^2 + (y - b)^2 = r^2, \tag{4.3}$$

where $(x_i, y_i)^T$ is the pixel coordinate. Votes for possible solutions of the point center $(a, b)^T$ and its radius, r are stored in an accumulator matrix. As multiple edge pixel are evaluated, a peak in votes will be accumulated for the true point location [61]. The selected MATLAB implementation uses an improved two-stage approach. This approach reduces the accumulator array to a 2D matrix by combining the votes for different radii, which reduces the required memory considerably. The point radii are detected in a second step, hence the name, by determining a radius histogram of the edge pixel from the point center. Further improvements to the algorithm are done by only considering center locations which lie orthogonal to the edge pixel gradient and limiting the number of candidate pixel by only including pixel with high gradient.

Overall, the improved preprocessing allows quite robust point detection and center location measurement, as can be seen in Figure 4.5e. Some false positive points are detected at the wing stiffeners, while some marker points remain undetected. Undetected points are mostly points that are heavily distorted or occluded by other points. Occlusion by wing stiffeners was limited although smaller points are used. The two-stage method showed to reduce the detrimental influence largely and typically detects elliptical points with an aspect ratio of up to two, and points which are up to 50 % occluded. This is showed to improve the performance at shallow viewing angles, considerably, where other methods often detected two elliptical points in close proximity as one point in the center, making tracking near impossible. Other, more complex location detection methods such as center of mass methods [37] are likely to perform even worse with overlapping points, were however not tested.

Some points are also lost due to a low intensity gradient. To prevent this, if no point is found close to a predicted location, a local search is done using a search window with normalized intensity, which increases the edge gradients considerably.

To reduce the processing time, all preprocessing steps and point finding is done in parallel to the other processing steps. This reduces the impact on the total processing time from approximately 50 % to 10 % (fetching the results from the parallel process requires some time), while also limiting the memory requirements as only one image pari is stored at a time.

4.2.3. Image plane location prediction

The method used to predict point locations changes over the course of the processing, as indicated by Table 4.1. The different timesteps are indicated by it and point numbers by ip.

Table 4.1: Image location prediction methods for different time instances and status.

$it = 1$		$1 < it \leq it_{cycle}$		$it > it_{cycle}$
$ip = 1$	$ip > 1$	matched	unmatched	
Manual	Spatial	Temporal	Reprojection	Cyclic

Manual prediction   Initially, per wing one point must be selected manually. While possible within the algorithm, for batch runs the approximate point location is done outside the execution in any image editing software, and then entered to the initialization file. Based on this prediction, the correct point found by the CHT method is corresponded, as explained in detail in Section 4.2.4.

Spatial prediction   The remaining points in the first timestep will then be detected automatically using the known point spacing. This spacing is also supplied within the initialization file, together with an estimated magnification factor to convert the unit to pixel.

This spatial prediction works based on a radial basis function (RBF) interpolation. Therefore, the expected location of point i, $(\tilde{x}_{i,n}, \tilde{y}_{i,n})^T$ based on neighboring points, n at $(x_n, y_n)^T$ with a relative wing surface distance of $(\Delta x_{i,n}, \Delta y_{i,n})^T$ is calculated as

$$\begin{pmatrix} \tilde{x}_{i,n} \\ \tilde{y}_{i,n} \end{pmatrix} = \begin{pmatrix} x_n \\ y_n \end{pmatrix} + \begin{pmatrix} \Delta x_{i,n} \\ \Delta y_{i,n} \end{pmatrix}. \tag{4.4}$$

These expected locations are then weighted based on the wing surface distance using a C^2 compact support function with 200 pixel support radius. During this interpolation only point locations with a which are successfully tracked are considered. This is done using different status assigned in the following steps.

Temporal prediction   For the subsequent timesteps, a temporal tracking method is used to predict the point locations. Therefore, an up to third degree polynomial is fitted to the growing time-series, which coefficients are be used to determine the point velocity (after the first timestep they are assumed to be zero). The velocity multiplied by the timestep then gives an estimation of the point pixel shift.

As the determined point locations contain some error, noise quickly accumulates in the determined velocities. To detect outlier in the velocity, a spatial fit of the velocities is computed using the same RBF interpolation as the initial spatial prediction. If the difference between calculated and fitted velocity is larger than the fitted velocity itself, the calculated velocity is replaced by the fit, and the point is assigned with an according status. It showed thereby that normalizing the velocities with the spanwise point location, analogous to the rotational velocity around the stroke axis, improves the spatial interpolation.

Reprojection prediction   Points which were lost in previous timesteps use a different prediction method. Instead of the temporal prediction, now the relative spatial locations are used to predict their location. Different tests showed that this is best done in the world domain. Therefore, the spatial prediction method used in the image domain above is slightly modified to work in three dimensions, see Section 4.2.5 for more details. This spatial prediction is applied to the previous timestep, which is then advanced to the current timestep using a temporal prediction analogous to that used in the image domain. The spatial world prediction is then re-projected into the image view using the camera model. Additionally, if the point is considered to be correctly corresponded in the other view, the prediction is improved further by moving the re-projection onto the epipolar line.

Points which are not successfully corresponded based on the temporal prediction in a certain timestep are attempted to be corresponded once more using this method. Thereby the spatial fit is not necessary as the previous location is considered to be correct.

Cycle prediction   As the wing motion is considered to be cyclic, the wing points track will repeat with each cycle. This makes the prediction of point locations easier once a complete flapping cycle is measured: The location of a point in the previous cycle or cycles can simply be used for the location

prediction of the following cycles. Several steps must however be completed before such a cyclic prediction can be used.

First, the exact cycle length, i.e. the number of recorded images per cycle, must be determined. Therefore, after the first cycle is measured (plus several recordings to be conservative as the exact length is initially not known), the points found in the last image recording are corresponded to each of the wing points in the first cycle. This is done using the optimization method used in Section 4.2.4. The timestep with the lowest mean distance between corresponded points is then assumed to be at the same phase as the last recording. The delta in timesteps divided by the approximate number of completed cycles between the corresponded recordings then gives an exact measurement of the mean cycle length and flapping frequency over the recording. Using this, the phases of all timesteps can be determined.

Then, the point location in subsequent timesteps is predicted to be that of the corresponding phase in the previously evaluated cycles. As some points may however be lost during the evaluated cycles, not all phases could be predicted using this cyclic prediction. Therefore, a gap filling and filtering process is executed, identical to that in the final postprocessing step, explained in Section 4.2.6. The prediction is reevaluated after each successive cycle, becoming slightly more accurate as lost point gaps are closed in some cases.

4.2.4. Corresponding point location prediction and measurements

After point predictions and measurements are acquired in a camera view, they are then merged. Initially, the correspondence simply done in sequence: The distance of the manual approximation from all point measurements is calculated and the measurement with the lowest distance is considered to be this point. Based on this measurement, the spatial prediction of the next point is then calculated, and again corresponded to the remaining measurements. This process is repeated until all points of one wing are matched, then the same process is repeated for the second wing in that camera view.

This sequential approach is however flawed. Especially when multiple points lie close to another, or when point predictions are poor, it easily occurs that a prediction is corresponded to an incorrect measurement. This will lead to further incorrect correspondences down the line, making the processing algorithm diverge. Therefore, an optimization routine was setup which simultaneous corresponds all point predictions and CHT measurements by minimizing the total prediction error. This process is based on a mixed-integer linear programming algorithm implemented in the `intlinprog` MATLAB function, to which a matrix with all prediction to measurement distances below a certain limit is inserted. This limit is reduced from 20 pixel in the initial timestep to 10 pixel from the third timestep onwards. Constraints are applied which force at least one measurement to each point and prevent duplicate use of a point measurement. To prevent the optimization from failing if a prediction cannot be corresponded as no suitable point is available, the distance matrix is padded with a separate placeholder value for each prediction. Points which could not be matched successfully using this method are applied with a corresponding status.

During the initial cycle, these points are attempted to be corresponded in a second loop using the reprojection prediction, together with points that have previously been lost. Allocated measurements are thereby neglected.

4.2.5. World point location calculation and correction

The corresponded points are then triangulated with a DLT method introduced in Section 2.2.3 implemented in the MATLAB function `triangulate`. Points which are found in only one view are also triangulated, a measure which had to be taken as a considerable amount of point occlusion exists, and no third camera view is available. As the prediction methods showed to work relatively well,

this has only a quite limited effect on the measurement quality as shown later in Section 4.3.1.

Furthermore, poor points correspondences that lead to incorrect triangulation are corrected. To be considered as a successful triangulation, the reprojection error must not be above a tolerance of 1.5 pixel, and it must be within 2.5 mm of a spatial fit of the wing (5 mm for the first timestep). Points which do not comply with these tolerances are assigned with an according status and neglected in later calculations.

The spatial fit is calculated using a procedure similar to the previously introduced spatial image plane location prediction method. Therefore, the wing points are first transferred to a new coordinate system which is aligned with the local wing surface. This allows the prediction in x and y directions to be calculated as before. The C^2 compact support thereby uses a dynamic support radius to include 8 neighboring points. The z location is then determined using a second degree 2D polynomial interpolation at the calculated $x - y$ location.

Once a point exceeds the tolerances by a factor of two, the algorithm attempts to correct the measurement. Therefore, the view with lower certainty is determined, which is either the view where no point measurement could be corresponded, or if both views are successfully corresponded the view where the reprojection of the spatial fit lies further from the measured point location. The reprojection of the worse camera view is then attempted to be corresponded with an uncorresponded point measurement. If successful, the point is then again triangulated, if not the point status is set to missing. The increased tolerance of the correction is used to prevent over-use of corrections without allowing incorrect triangulations to be considered in the spatial world fit for other points.

4.2.6. Postprocessing

After the complete recording is processed, the measurement series is low-pass filtered to remove noise. This is done using the `lowpass` function in MATLAB with a cut-off frequency set to the 10th flapping harmonic. This is a relatively high limit, compared to the influence limits found in other studies [15, 47] which makes the filtering process conservative. Furthermore, the results are ultimately supposed to be concentrated to a single cycle as only the average deformation is of interest. However, it was chosen to calculate different parameters first for all timesteps, and concentrate the final results afterwards as this allows an estimation of the parameter variation over the recording length without the need for more extensive uncertainty propagation analysis.

The later analysis uses the measured points to represent the wing surface, i.e. the most forward and backward point are used as wing leading and trailing edge, respectively. As the wing point grids are shifted between the wings, they must be interpolated to the same wing surface locations to obtain equivalent parameters. Here, the points on the lower wing are interpolated to match the upper wing.

Next, the measurements are transferred from the coordinate system used in the DLT algorithm, which is relative to the center of the first camera, to the body coordinate system, denoted by the subscript "$_b$" shown in Figure 4.6a. Therefore, the location of the fuselage markers in the background recording are determined and triangulated, which gives the x_b axis and origin. The marker location is thereby determined manually. The yb axis is then determined using the mean location of the wing leading edge markers at the timestep with the closest distance, which gives the dihedral plane.

Most parameters for the later discussion are however based on the local wing coordinate system, denoted by the subscript "$_w$". This system is fixed to the wing leading edge as shown in Figure 4.6a. An exemplary $x_w - z_w$ cut is shown in Figure 4.6b, where the radial span location is denoted by r_w, typically normalized by the total half span to r_w^*. In this plot, the shown measurements are nor-

(a) Sketch of the DelFly including body (red) and local wing (green) coordinate systems and dihedral plane (blue).

(b) Definition of airfoil parameters in normalized $x_w - z_w$ plane at spanwise location r_w.
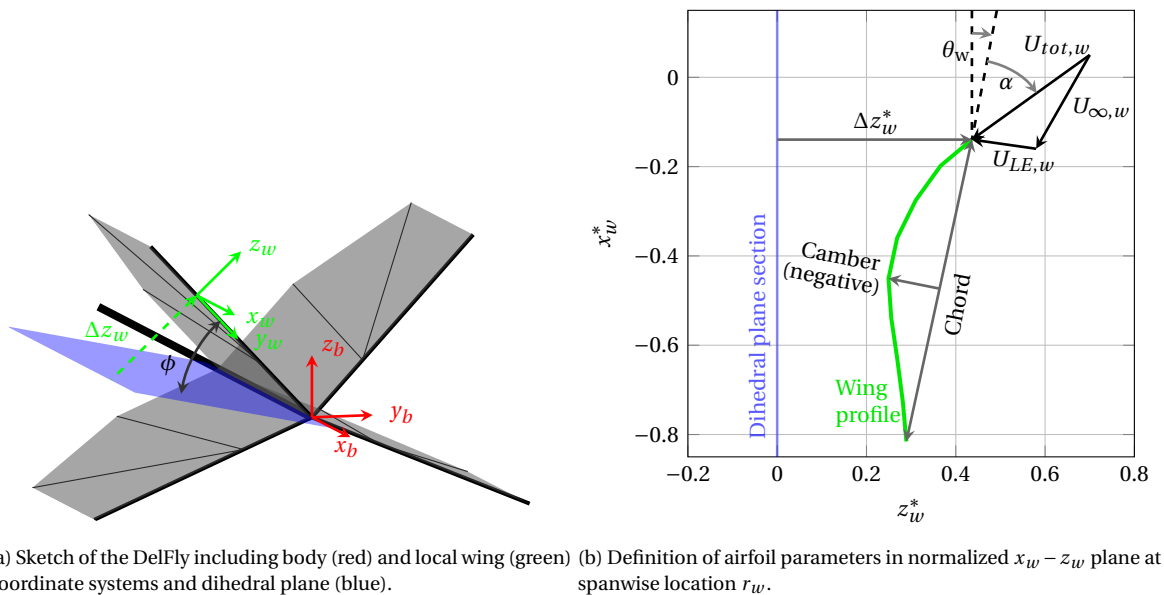
Figure 4.6: Coordinate systems and airfoil parameter explanation.

malized by the mean chord (indicated by the asterisk) and the origin is shifted by $\Delta z_w = tan(\phi) r_w$ to the intersection with the dihedral plane to visualize the stroke angle.

The camber ratio ε is the ratio of local camber and chord, where a curvature against z_w-direction is defined as negative, as shown. The incidence angle θ_w is the angle between the chordline and the x_w-axis and used to describe wing twisting. The difference between incidence angle and angle of the inflow velocity $U_{tot,w}$ is used to represent the angle of attack α. Thereby the inflow direction is calculated from the sum of the freestream velocity in the wing reference frame $U_{\infty,w}$ and leading edge velocity $U_{LE,w}$, however induced velocities are neglected.

Ultimately, all results are concentrated to a single cycle. Therefore, all timesteps are initially sorted into phase bins with size $\Delta t^* = 0.01$. The phase is indicated by the non-dimensionalized time $t^* = t/T_f$, where the flapping period $T_f = 1/f$. The cycle start ($t^* = 0$) is defined at the minimum distance between the wing leading edge, i.e. the cycle starts at the outstroke of the wing pair and ends with the instroke.

4.3. Performance and verification

Using the described measurement setup and algorithm, the DelFly wing deformation could successfully and reliably be measured in various flight conditions with limited effort for varying the setup and a mostly automated processing algorithm. A closer look at the performance of the used methods is done in the following sections. First an investigation of the tracking performance is done, followed by a reference case measurement for assessment of the general accuracy.

4.3.1. Tracking

Figure 4.7 shows different average tracking quality characteristics of the measurements. The upper wing is generally tracked better compared to the lower, having only 2.4 % lost points with an average reprojection error of only 0.195 pixel, compared to 4.4 % and 0.225 pixel for the lower wing. This occurs as over the cycle the stiffeners of the upper wing move across most of the lower wing points. Furthermore, the point intensity is slightly lower, as the light is diffused slightly when moving through the upper wing, and the points become slightly smaller as they move further away from

the camera.
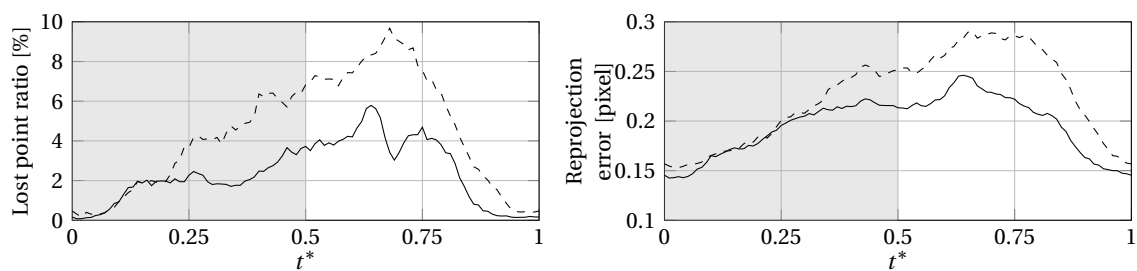
(a) Ratio of unsuccessfully tracked points. The outstroke phase is shaded in grey.

(b) Reprojection error of successfully tracked points. The outstroke phase is shaded in grey.
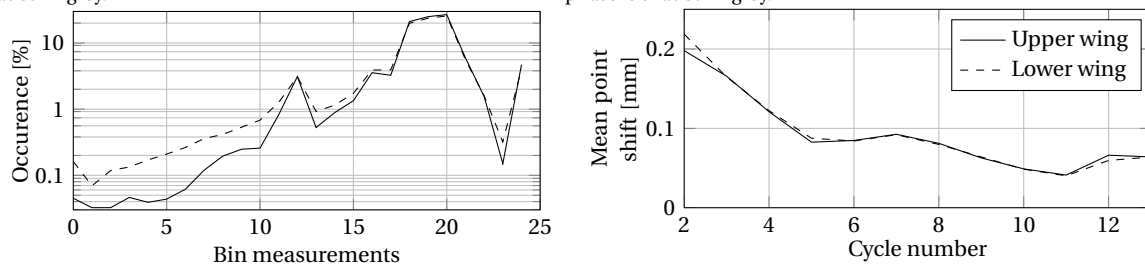
(c) Number of measurements per phase bin.

(d) Shape convergence.

Figure 4.7: Average upper and lower wing point tracking quality neglecting descent cases.

At the cycle start and end the tracking is thereby best with close to zero points lost, which is logical as points are not overlapping during the contact phase. Following this, the first cycle half is tracked well, while the second cycle half shows worse quality. No straightforward explanation for this behavior could be found. Potential reasons could be that the velocity calculation does not perform well for point movement reversal while several points are lost, or a negative impact of the specific point motions, e.g. more occlusions during this phase.

Nonetheless, is can be said that the general quality is decent. For all flight states 2000 recordings are taken (1 s recording time), which accounts to around 10 measured cycles. Each of the 100 phase bins has then typically close to 20 measurements, as can be seen in Figure 4.7c. On average, for the upper wing 1.1 % of the bins have below 10 measurement points, while for the lower wing 3.1 % have below 10 measurement points, which speaks for a decent statistical convergence.

This is also supported by the convergence of the mean wing shape. Figure 4.7d shows that between the first and second timestep the wing shape still changes on average by 0.2 mm, while from the tenth cycle this change becomes closer to 0.05 mm, which is a very acceptable value considering the movement complexity. Also, the fast convergence over the first few cycles shows that the assumption of cyclic movement is valid, supporting the cycle prediction method.

4.3.2. Reference case accuracy and verification

To gain insight into the accuracy of the world locations, reference measurements of a 150 mm diameter sphere were done (see Figure 4.8a). The measurements used the same camera setup, calibration, and processing algorithm as the wing measurements, thus represent the measurements closely. 63 markers of 1 mm radius were manually identified in the images and triangulated, having an average reprojection error of 0.11 pixel, which is very close to the calibration error. A sphere of known radius was then fitted to the world point locations using a least squares approach based on the `lsqlin` MATLAB function. The average fit distance or residual of all points is 0.12 mm.

Assuming that the measurement accuracy has a linear relation with the reprojection error, the wing deformation measurements can be said to be accurate to approximately 0.25 mm or 0.18 % of the half wingspan.
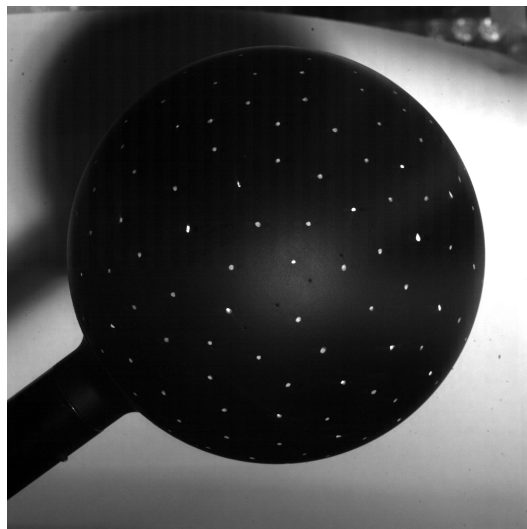
(a) Sample recording.
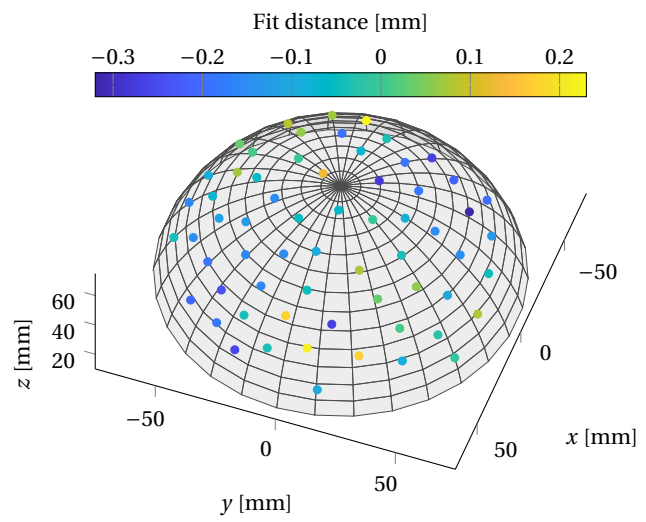
(b) Point location measurements with distances from fitted surface.

Figure 4.8: Reference sphere measurements.

5

Results

The agility of the DelFly allows numerous flight conditions. To limit the scope of the study, the results focuses on four static cases: hover, climb, forward flight, and descent. Hover and climb are initially treated in in Sections 5.1 and 5.2. The conditions are thereby treated as a parameter study of flapping frequency and freestream velocity, to which pitch angle effects are added in Section 5.4. The insight gained with this parameter study is then applied to the forward flight condition in Section 5.5, which varies these three parameters simultaneously. While the general non-linear behavior of the wing deformation does not allow straightforward superposition of the effects determined in the parameter study, they still allow better interpretation of the results. Finally, descending flight is shortly investigated, completing the range of flight conditions. Here, the freestream direction is from behind the DelFly, i.e. $U_\infty < 0\,\mathrm{m\,s^{-1}}$.

5.1. Hovering flight and flapping frequency effects

In ideal hovering flight, the DelFly would remain completely stationary, thus it experiences no freestream velocity. However, as the DelFly uses a tail to maintain stability, it cannot remain in a completely fixed position, but must always maintain some forward speed. This shows that modeling true hover is not sensible here, and zero freestream velocity is a better case which allows further interpretation of the phenomena. Recently tailless DelFly was developed which can maintain a fixed stationary position more reliably [27], which makes the stationary ambient conditions more relevant.

To maintain a force equilibrium, the flapping frequency must be set to a specific value, which increases with the MAV mass. The standard DelFly has a mass of approximately 25 g, and requires a flapping frequency of slightly above 13 Hz at very low flight velocities [26, 32]. As hover is not exactly simulated, two arbitrary flapping frequencies of $f = 7.5\,\mathrm{Hz}$ and 12 Hz were chosen to test at zero freestream velocity, which were also used in the studies of Perçin et al. [37]. This allows the hover case to be used as further verification of the measurement process in the following section. The previous studies thereby measured only the upper wing and assumed mirrored deformations for the lower. As now measurements of both wings are available, an investigation into any present asymmetric effects is also done, including a study on the influence of the sideways orientation, presented in Section 5.1.5.

Due to the not complicated setting of the flapping frequency (See section 4.1.1) the final evaluation showed a flapping frequency of $f = 7.571\,\mathrm{Hz}$ and 11.996 Hz.

55

5.1.1. Hovering flight verification

A short comparison of actual wing deformation measurements is done to verify that the general measurement approach such as calibration, parameter setting, postprocessing and other is correct. This verification adds to that in Section 4.3, where the general tracking process and measurement accuracy was accessed. Therefore, the newly acquired measurements are compared against those by Perçin et al. [37], which were supplied in digital form for the $f = 7.5\,\text{Hz}$ hovering case. This case was recreated using the newly developed setup, however the wing thickness of the new measurements is 5 μm thicker compared to those of the reference case, which still used the old 10 μm reference thickness wings. As the influence of wing thickness on the DelFly wing deformation is already studied by Perçin et al. [37], it can however be considered in the verification.

Figure 5.1 shows wing 20 wing cuts or airfoils over the cycle at $r_w^* = 0.71$ of the upper wing of both the new and reference results. As the leading and trailing edges are here represented by the marker point, the marker grid of the new results is interpolated to those of the reference (starting 5 mm from the leading edge with 5 mm spacing). Furthermore, the results were aligned and synchronized as accurately as possible by hand, as different reference points and cycle starts are used in the reference.
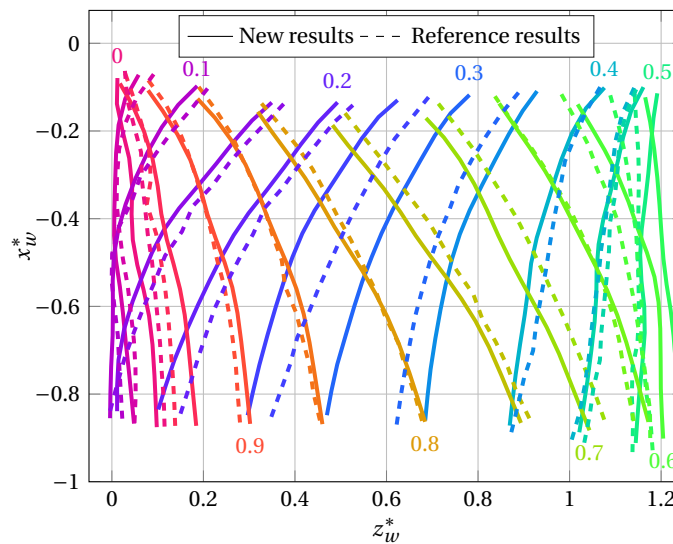
Figure 5.1: Comparison of wing deformation at $r_w^* = 0.71$ between new results and those of Perçin et al. [37] with 15 μm and 10 μm wing material thickness, respectively for $f = 7.5\,\text{Hz}$. t^* is indicated in the respective color of the airfoil sections.

The wing motion is generally quite similar for the new results. The most apparent difference is in phase, where the reference results are advanced during the outstroke and delayed during the instroke. On closer inspection it can be seen that this shift is due to a very small displacement of the reference wings from $t^* = 0.4$ to 0.45, and from $t^* = 0.95$ to 0, which speaks for very high accelerations around these phases. In comparison, the new results show a much smoother wing motion towards the stroke reversals. The change in wing mass may explain this different behavior, as the higher inertia of the new wings leads to lower accelerations. Similarly, it can clearly be seen that the new wing moves further during the stroke reversals, especially the trailing edge at the end of the outstroke, and also the leading edge at the instroke. This can also be attributed to the higher wing mass and inertia, which result in a lower influence of aerodynamic damping. This was as clearly shown by in-vacuum measurements by Perçin et al. [37], where aerodynamic damping is completely removed. Another difference is the larger heaving motion of the leading edge during the instroke of the new results. Large heave generally speaks for high wing loading, which is indeed found to be increased during instroke and reduced during the outstroke for the new wings [37]. The lower

wing, shown in Figure 5.2a, does however not show this heave phenomena, thus it speaks more for a variation of the in-plane wing stiffness compared to the reference measurement. Apart from these differences, the general change in wing deformation appears quite similar, with comparable twist and camber during most of the cycle. This further speaks verifies the measurement approach and increases confidence in the later findings.

5.1.2. General deformation

A representation of the general temporal development of the wing deformation is given in Figure 5.2. The spanwise location, $r_w^* = 0.71$ is chosen as it showed to give a good representation of the average wing shape. Spanwise effects are here not visualized, however they are relatively minor and mostly straightforward as shown in Section 5.1.4, where they are discussed in some more detail.
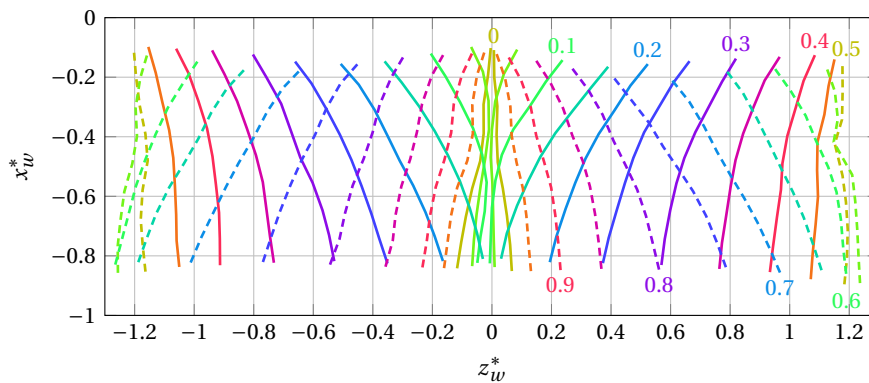
(a) $f = 7.5\,\text{Hz}$. t^* is indicated for the upper wing.
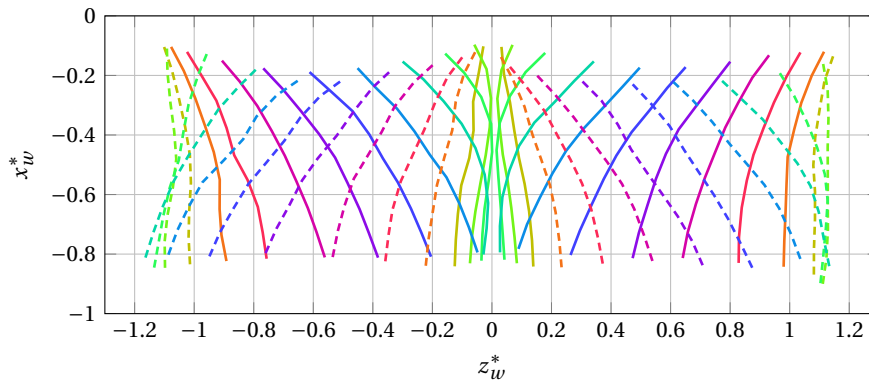
(b) $f = 12\,\text{Hz}$.

Figure 5.2: Wing deformation at $r_w^* = 0.71$ over the flapping cycle in hover due to different flapping frequencies. The upper wing can be seen in the right half, the outstroke cuts are dashed.

At $t^* = 0$, the wing leading edges are in closest proximity, with the lower wing just left of $z_w = 0$ and the upper just right. Subsequently, the wings leading edges are moved apart driven by the flapping mechanism, with the wing surface lagging slightly behind. This inertial effect passively produces an incidence angle of the wing surface as well as some camber. The incidence angle typically reduces the local angle of attack relative to the inflow direction, which is here mostly in the stroke plane. Specifically, the inflow direction in stationary ambient condition is determined entirely by the wing leading edge path, which not only moves in the stroke plane, but also starts to heave backwards at the stroke start, and again forwards towards the outstroke end where the wing decelerates. At the stroke end, the trailing edge catches up to the leading edge, and in the $f = 7.5\,\text{Hz}$ case even moves past it. This initiates the wing rotation, which again leads to a trailing wing surface with opposite incidence angles and camber during the instroke.

The stroke reversals thereby differ considerably. While at the outward position the wing is relatively flat during the rotation, at the inner position the wing-wing interaction result in a considerable camber formation. This is the previously described clap-and-peel effect, where first the leading edges come together, followed by the remaining wing surface, where the minimum distance region travels aft as the forward region detached. This peeling is the result of the formation of a LEV, which creates a low pressure region between the wings preventing the wing surfaces from detaching earlier and thus leads to large wing surface curvature. The relative duration of the clap-and-peel increases thereby with flapping frequency, here from $\Delta t^* = 0.136$ to $\Delta t^* = 0.174$, which could be explained with a stronger LEV formation holding the wings together.

Interesting is thereby that the wings do not come into contact during the clap-and-peel. Previously it was already found that the leading edges make no contact at faster flapping frequencies [37], however the remaining wing surfaces were assumed to touch. As now - for the first time - both wings are simultaneously measured during this phase, it can be seen that minimal distances remain at all times apart from a region close to the root trailing edge. In the $f = 7.5$ Hz case, this gap is relatively small at around 0.2 mm, which is still close to the measurement uncertainty, however at the faster flapping frequency this gap is increased to around 0.7 mm. The general presence of such 'air-buffer' between the wing surfaces is plausible, as viscous forces prevent large fluid accelerations close to the wing surfaces. Determining an exact reason for this behavior is however difficult, and is likely due to a combination of interactions over the entire wing cycle, such as pressure fields and elastic forces. The wing stiffeners thereby appear to reduce the wing gap, which is sensible as the increased stiffness pushes the surfaces closer together.

Some asymmetries can be seen in the overall wing deformation, these are discussed in more detail in Section 5.1.5. Also, the upper wing airfoil shows a sharp kink around $t^* = 0.5$, which is likely a measurement error. This may occur due to an incorrect point measurement or correspondence.

5.1.3. Parameter study

To better understand the differences between the two measured cases, the airfoil parameters at $r_w^* = 0.71$ are plotted against another over time in Figure 5.3. Again, some asymmetries are evident in the plots, as well as large standard deviations (s.d.) between the cycles at some instances. Typically, the s.d. lies within one percent or degree, which shows that the wing motion is very periodic. Therefore, the important trends between different flapping frequencies are clearly visible and allow further discussion of parameters.

The maximum incidence angle increases with faster flapping frequencies, with the $f = 12$ Hz case having peaks of around $|\theta_{w,max}| = 35°$, while the $f = 7.5$ Hz case peaks at around $|\theta_{w,max}| = 28°$. This increase is a result of higher inertial and aerodynamic loads due to the higher acceleration and inflow velocities, respectively, which leads to larger deformation of the wings. Furthermore, the incidence angle variation is delayed for the higher flapping frequencies, which means that the trailing edge lags further behind the leading edges. This phase shift was already noted previously and linked to the phase shift between structural and aerodynamic forces, where the latter are now increased [37]. This contrasts with other literature, which found the inertial effects to be the dominant influence on wing bending similar insect wings [10]. The rate of the incidence angle increase during the outstroke is thereby similar for both cases, it only stops later for the fast flapping frequency as it appears to be coupled to the trailing edge detachment, which is delayed in this case.

After the trailing edges detach, they accelerate quickly to velocities higher than the leading edge, which can be explained by the elastic forces build-up during the clap-and-peel. This behavior is especially visible at lower flapping frequencies, as aerodynamic damping is not as dominant here, which results in the trailing edge sweeping past the leading edge in the $f = 7.5$ Hz case. During the instroke, the incidence angle again increases later but to higher values at faster flapping frequencies.

(a) Incidence angle.

(b) Camber ratio.

(c) Angle of attack.

(d) Inflow velocity magnitude.
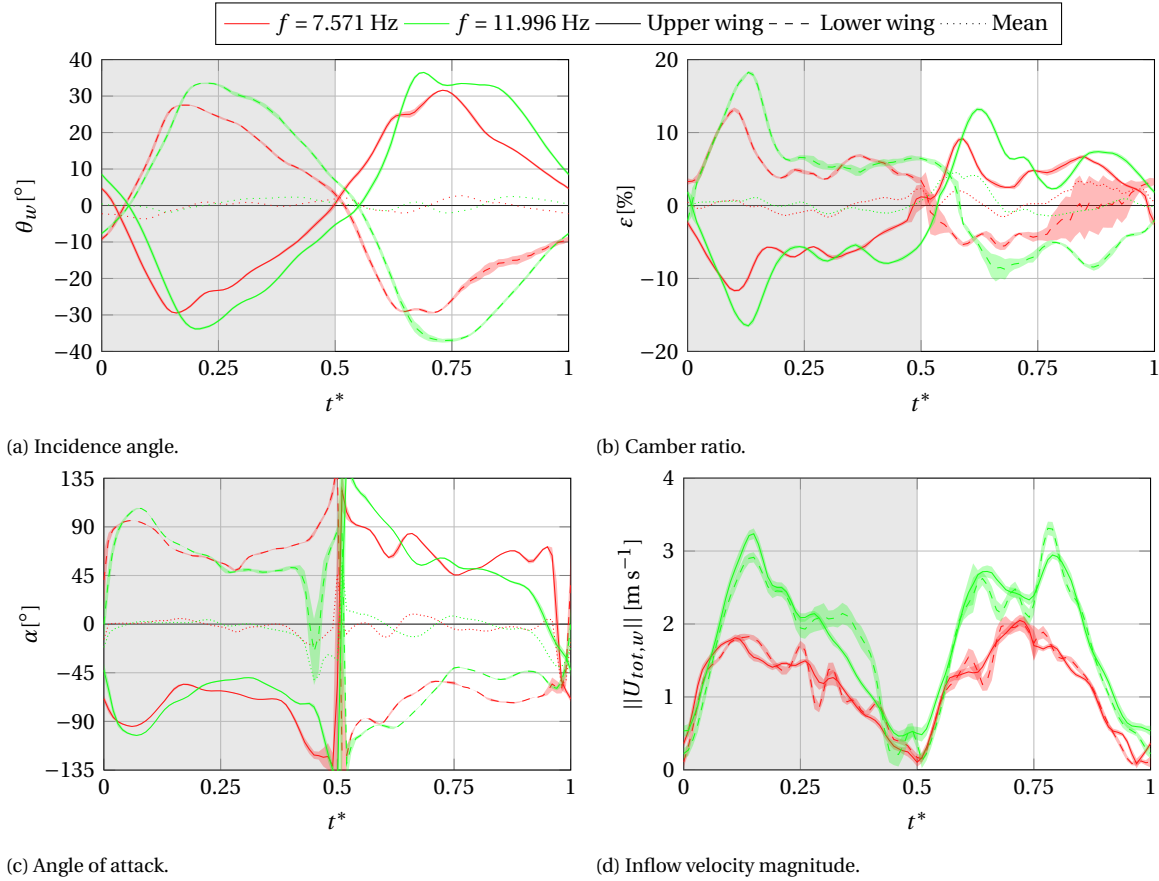
Figure 5.3: Airfoil and inflow parameters at $r_w^* = 0.71$ in hover due to different flapping frequencies. The outstroke phase is shaded in grey, the instantaneous s.d. is shaded in the respective color.

Apart from the wing twisting, the camber ratio also plays a significant role in force production and is worth analyzing. The wing peel leads to a large camber production during the cycle start, which is considerably larger at fast flapping frequencies, with $|\varepsilon_{max}| = 17.5\%$ for the $f = 12\,\text{Hz}$ case compared to $|\varepsilon_{max}| = 12.5\%$ for the $f = 7.5\,\text{Hz}$ case. As the phase duration is increased at higher flapping frequencies, the camber ratio peak is slightly delayed. For the rest of the outstroke, the camber ratio remains mostly constant with only slightly larger magnitude in the high f case. At the start of the instroke, the camber of the upper wing shows another peak, although lower than that during the clap-and-peel of the outstroke. This is similar to the recoil motion seen to increase thrust production in different insects [17, 48], which occurs due to specific inertial effects leading to trailing edge lag.

The increased aerodynamic loading can be derived from the increased inflow velocity magnitude, shown in 5.3d, which peaks are almost doubled for the faster flapping frequency. As no freestream velocity is present, the inflow velocity is thereby mostly in the stroke plane. This is also visible in the angle of attack plot in Figure 5.3c, which shows $|\alpha| \approx 90°$ at the stroke reversals where the wing has low incidence angles (and does not heave considerably). Towards midstroke the incidence angle increases, which reduces the angle of attack. This effect is increased with faster flapping frequencies, as the wing twist is increased. During the stroke reversals the angle of attack peaks and changes sign rapidly while having large s.d. spikes. These occur due to small changes in the leading edge movement direction which result in large computed direction changes as the velocity magni-

tude is almost zero. This may also explain the sudden drop of the $f = 12\,\text{Hz}$ case at $t^* = 0.42$, where potentially an incorrectly corresponded point results in a velocity spike. As the calculated inflow velocity is likely to be negligible compared to induced velocities during this phase, the stroke reversals should be neglected here. Generally, the change in angle of attack has a smaller effect than the increase in inflow velocity in the hover case.

5.1.4. Spanwise deformation

As mentioned above, the spanwise wing deformation is relatively straightforward: the deformation magnitude typically increases towards the wing tips while maintaining the same temporal trends. This general trend can be explained by the increasing inertial and aerodynamic loads towards the wing tip, and the reduced stiffness of the wing leading edge and wing surface. When looked at in more detail, some further phenomena can be found due to the non-linear nature of aerodynamics and structures, these however lie mostly below the scale of this parameter study.

The incidence angle shows the general increasing behavior almost perfectly, with the magnitude increasing almost linearly from root to tip for both flapping frequency cases, shown in Figure 5.4. Noteworthy is thereby that the outstroke twist peak occurs earlier at the tip. Closer inspection shows that across the span the peak coincides with the trailing edge detachment, which occurs first at the tip. However, at the instroke of the $f = 12\,\text{Hz}$ case the incidence angle also peaks early at the upper wing tip. When studying the 3D shape(Figure B.1), this peak can be linked to a torsional wave traveling down the span. This wave is also seen in other flapping wing fliers [47]. Here, it seems somewhat linked to the recoil effect in camber as it occurs at the same conditions and the same phase.

(a) Incidence angle at hover for $f = 7.5\,\text{Hz}$.   (b) Incidence angle at hover for $f = 12\,\text{Hz}$.
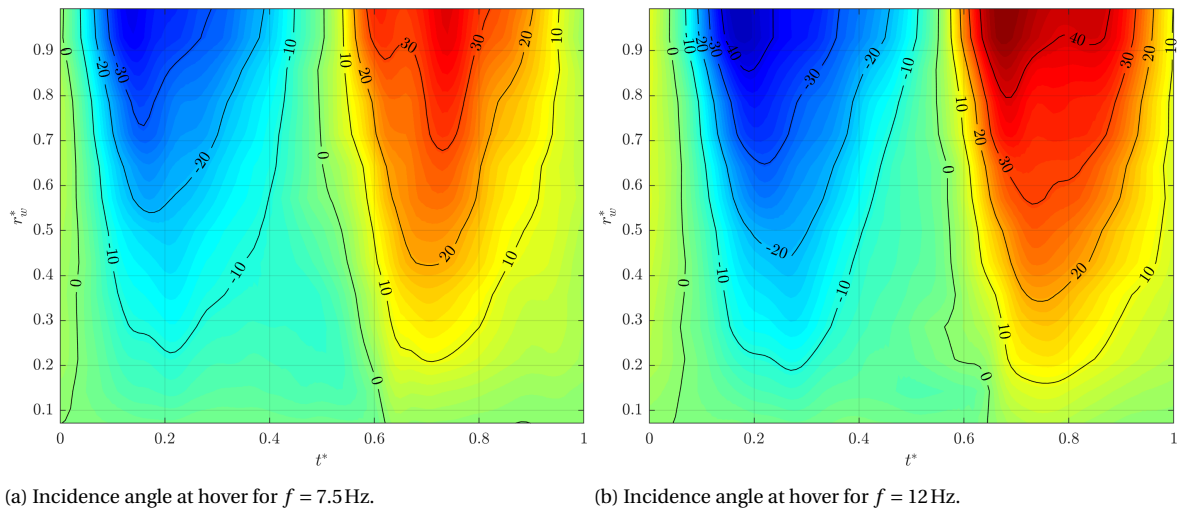
Figure 5.4: Upper wing incidence angle θ_w [°] over span and time in hover due to different flapping frequencies.

The camber ratio also shows larger values towards the wing tip, see Figure 5.5. Most dominant is the clap-and-peel phase, which results in the largest camber ratios with a peak close to the tip and a slightly delayed increase towards the root. During the remaining cycle, the wing tip however shows slightly lower values than the inward surface. The peak lies approximately at $r_w^* = 0.71$, which is in line with the findings of Perçin et al. [37]. They argued that at this location the outer stiffener position increases camber, while it flattens the airfoil further outward and mostly increases twist. As previously found, several smaller fluctuations occur over the remaining cycle, these however do not change considerably in spanwise direction. Close to the root the wing is almost completely flat,

as it is tensioned at the trailing edge.

(a) Camber ratio at hover for $f = 7.5\,\text{Hz}$.

(b) Camber ratio at hover for $f = 12\,\text{Hz}$.
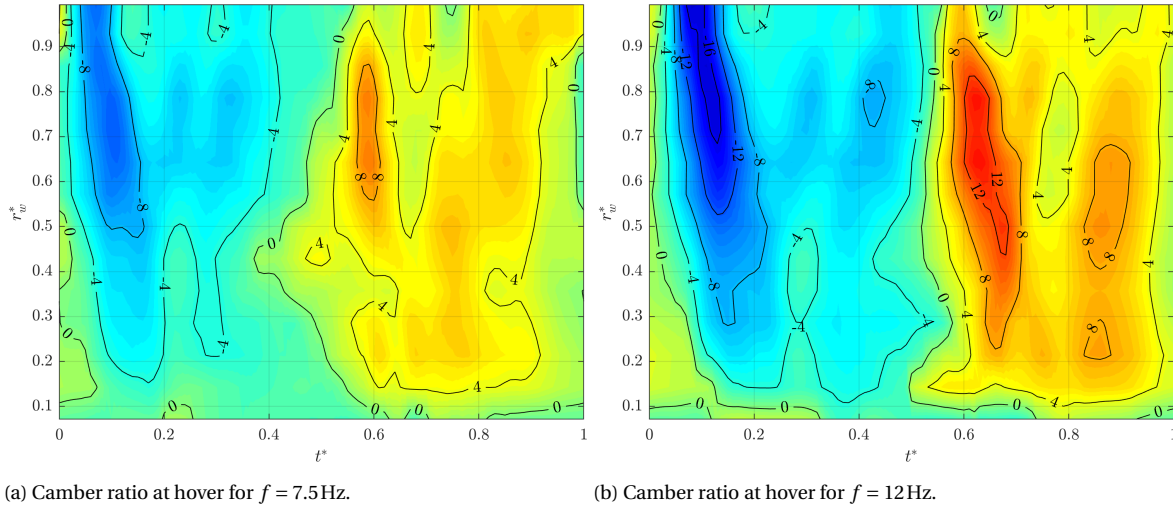
Figure 5.5: Upper wing camber ratio ε [%] over span and time in hover due to different flapping frequencies.

The remaining inflow parameters in spanwise direction of the upper wing are shown in Section A.1.

5.1.5. Inherent asymmetry and influence of sideways orientation

Even for this symmetrical flow case, some asymmetries in the wing deformations can be seen which previously were not considered. These asymmetries are visible especially during the end of the outstroke, where the lower wing displays camber while the upper wing is mostly flat. Also, the leading edge heave is clearly asymmetric, with the upper wing heaving considerably more during the instroke than during the outstroke, while the lower wing heaves approximately identically during both strokes. Multiple reasons could result in this asymmetry. The dihedral angle of the DelFly already introduces a slight asymmetry, as the upper wings come closer to each other than the lower. This leads to minor differences in the aerodynamic behavior, as well as possible asymmetric wing tensioning. Inaccuracies in the manual manufacturing process of the wings can increase these effects, short tests with a different wing pair for instance showed lower asymmetry in heave while retaining the asymmetry during the outer stroke reversal. Further discrepancies may be introduced by the measurement procedure, e.g. the support, the diffusion wall, small uncertainties in the set pitch angle and due to the sideways orientation.

The sideways orientation may affect the measurements as it effectively changes the direction in which gravitational forces act. Now, these act in y-direction, which is outside the wing symmetry plane, thus could result in slightly different behavior of the upper and lower wing. To get an approximate understanding of the magnitude of this change, the gravitational acceleration may be compared to the wing acceleration due to the flapping motion. While the measured tracks were filtered in the postprocessing, they are still too noisy to calculate the second derivative in time. Therefore, the theoretical tangential acceleration of the wing stroking between $\pm 22°$ is considered. Its rotational acceleration is calculated as

$$\ddot{\phi} = -\left(\frac{2\pi}{T_f}\right)^2 sin\left(\frac{t}{T_f}2\pi\right)22°\frac{\pi}{180°}, \tag{5.1}$$

which can be converted to tangential acceleration,

$$\ddot{x}_t = r\ddot{\phi}. \tag{5.2}$$

For a flapping frequency of $f = 12\,\text{Hz} = 1/T$, this gives a maximum acceleration at the wing tip ($r = r_{tip} = 0.14\,\text{m}$) of $\ddot{x}_{t,max} = 25.47\,\text{m}\,\text{s}^{-2} = 2.6\,\text{g}$. On average, the wing experiences an acceleration of $\ddot{x}_{t,mean} = 8.03\,\text{m}\,\text{s}^{-2} = 0.82\,\text{g}$ measured at the wing center ($r = 0.07\,\text{m}$). This shows that during the high acceleration phases, being approximately the stroke reversals, the change in gravity direction is likely not playing any considerable role, although fluid forces are minimal here. During the low acceleration phases, which are mid stroke, the gravitational forces play a relatively large part compared to the inertial forces, however here the aerodynamic forces dominate either way, thus also here the influence can be considered relatively small. This shows that the sideways orientation may is not likely to result in any considerable deformation changes.

This will especially hold for any asymmetric effects, as the misalignment of the gravitational force with the symmetry plane is minimal. A larger effect would be seen in the deformations from left to right: as the gravity force is acting towards the right wing pair in the measurements, the right wing pair will on average be deflected towards the symmetry or dihedral plane. Thus, in simple terms the delta in twist and camber between upper and lower wing would be decreased, while for the left wings the delta would be increased as the wings are deflected away from the symmetry plane.

To test this, a separate measurement of the left wing pair was taken to compare against the typically recorded right wing pair. During the processing it showed however that the camera calibration was not successful, with all points having an reprojection error of around 4 pixel. Nonetheless, the measurements could be processed, and the results appear sensible, neglecting an increased rate of incorrectly corresponded points. These measurements showed that no considerable difference in upper to lower wing deformation is present, visualized for the wing incidence angle and camber ratio in Figure 5.6. Other differences between the left and right wing half, such as the minor phase shift, are most likely due to the incorrect calibration and other measurement uncertainty.

(a) Incidence angle.   (b) Camber ratio.
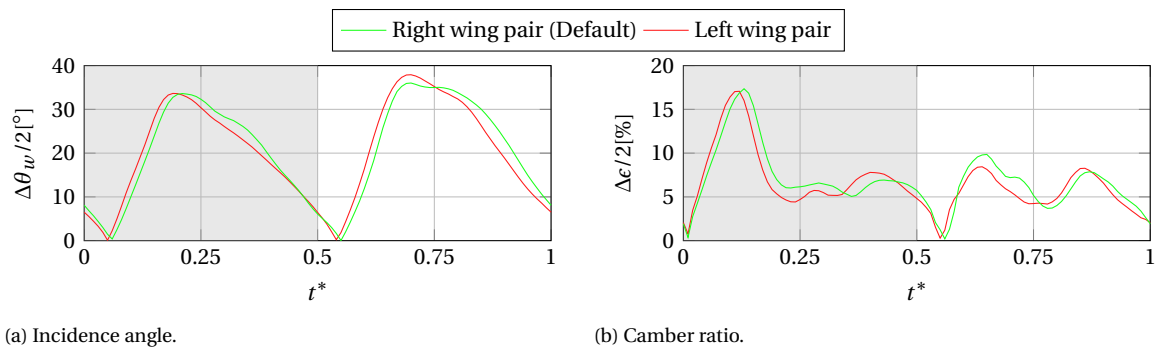
Figure 5.6: Difference between upper and lower airfoil parameters of the left and right wing half. Results are taken at $r_w^* = 0.71$. The outstroke phase is shaded in grey.

5.2. Climbing flight and freestream velocity effects

The influence of increasing freestream velocity was tested for two cases with $U_\infty = 1\,\text{m}\,\text{s}^{-1}$ and $2\,\text{m}\,\text{s}^{-1}$, or a Reynolds number of $Re \approx 5300$ and 10600. The flapping frequency was kept constant around $f = 12\,\text{Hz}$, specifically $f = 12.09\,\text{Hz}$ and $12.19\,\text{Hz}$, and the DelFly was aligned with the freestream ($\theta_b = 0°$). This again does not truly model climbing flight, as here the flapping frequency would need to increase with the freestream velocity (for the standard DelFly to values beyond $f = 13\,\text{Hz}$) to overcome the increased drag.

5.2.1. General deformation

The general deformation is again studied using the airfoil deformations at $r_w^* = 0.71$, shown in Figure 5.7. The deformations vary much less with U_∞ than f, however some small differences still occur. Mostly, the wing heave reduces at faster freestream velocities, and the wing tips stroke further and closer together, while the trailing edges maintain a similar displacement. The asymmetry between the wings is thereby reduced, with the wings heaving more symmetrically at higher flow-speeds.
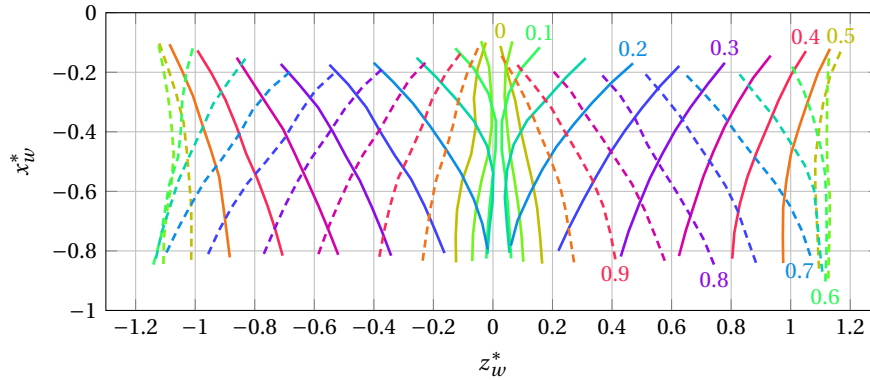
(a) $1\,\mathrm{m\,s^{-1}}$ climb.
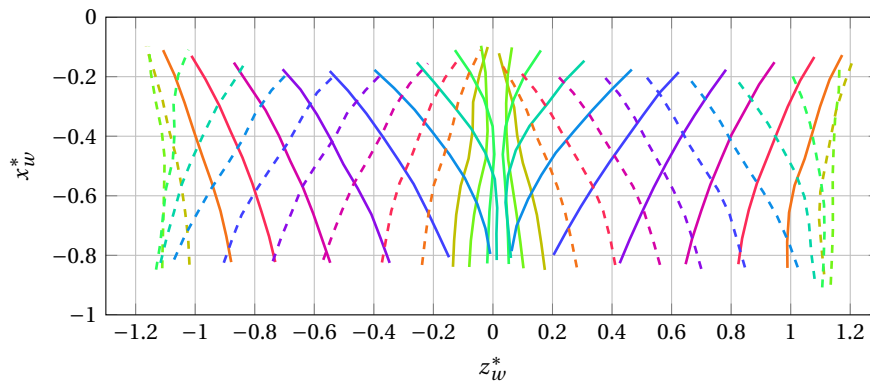
(b) $2\,\mathrm{m\,s^{-1}}$ climb.

Figure 5.7: Wing deformation at $r_w^* = 0.71$ over the flapping cycle due to different climbing velocities. The upper wing can be seen in the right half, the outstroke cuts are dashed.

The clap-and-peel duration remains almost constant, it is only slightly increased to $\Delta t^* = 0.193$ at $U_\infty = 2\,\mathrm{m\,s^{-1}}$. The wing gap is now increased considerably: apart from the wing stiffener and root at $U_\infty = 1\,\mathrm{m\,s^{-1}}$ the typical wing gap lies around 1 mm and for $U_\infty = 2\,\mathrm{m\,s^{-1}}$ around 1.3 mm.

5.2.2. Parameter study

A closer investigation of the wing deformation is done based on the airfoil parameters shown in Figure 5.8.

Through the clap and peel, the incidence angle again changes with an almost equal rate for all cases, with all reaching a similar peak of around $|\theta_{w,max}| = 35°$. In fast climb, the wing is initially twisted most outwards, and therefore twisted most inwards at the end of the clap-and-peel phase. This shows that there is a minor increase in phase lag of the trailing edge also with increasing freestream velocity. This lag is further increased by the time of the stroke reversal, as the leading edge moves faster and further in the climb cases. During the in-stroke, the incidence angle is then reduced at faster climbing velocities to values of around $|\theta_{w,max}| = 30°$ at $U_\infty = 2\,\mathrm{m\,s^{-1}}$. The increasing rate of the upper wing is now reduced, which speaks for a reduced torsional wave. This can also

(a) Incidence angle.

(b) Camber ratio.

(c) Angle of attack.

(d) Inflow velocity magnitude.
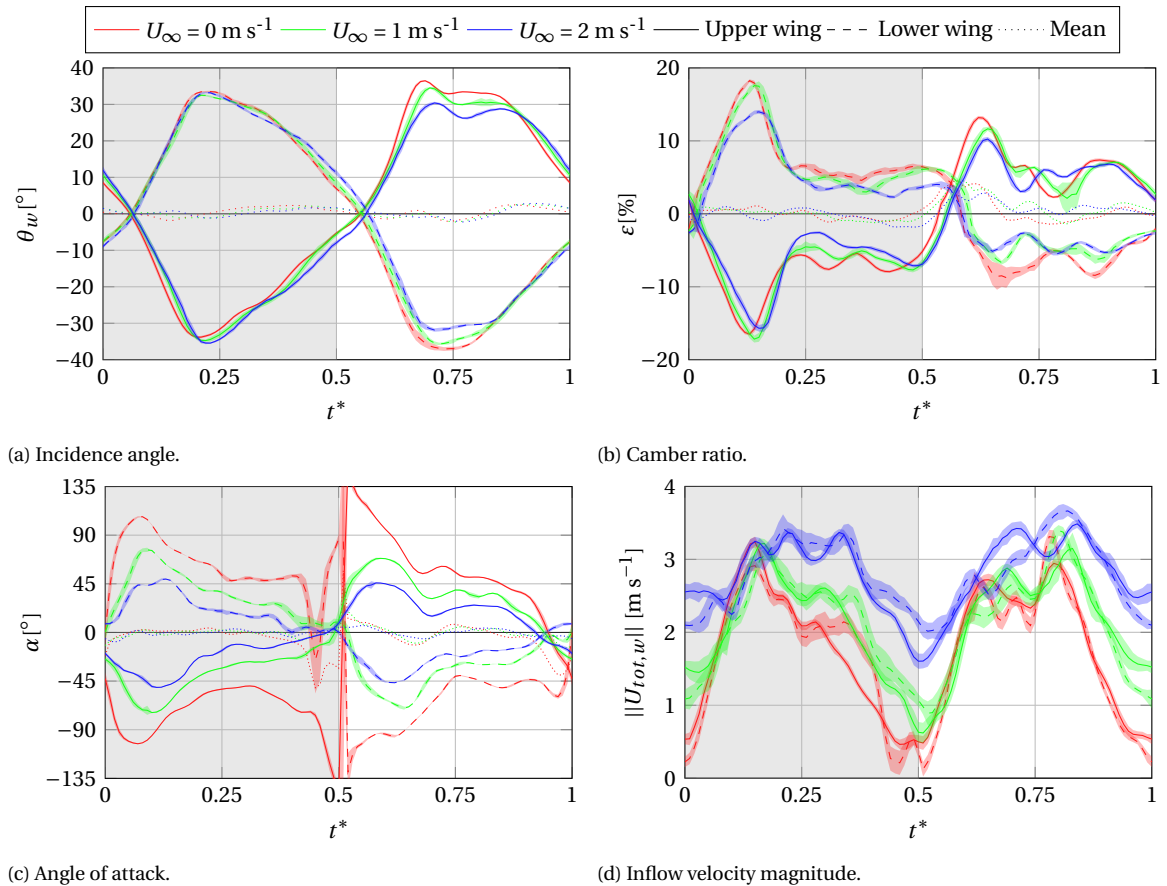
Figure 5.8: Airfoil and inflow parameters at $r_w^* = 0.71$ due to different climbing velocities. The outstroke phase is shaded in grey, the instantaneous s.d. is shaded in the respective color.

be seen in the 3D shape in Figure B.3. The maximum angle is then however maintained for longer and still shows minor oscillations.

These effects can be explained by the changing aerodynamic loading. Due to the high freestream component for the fast climb case, the inflow angle is now considerably reduced. For $U_\infty = 2\,\mathrm{m\,s^{-1}}$, this results in a low angle of attack of $|\alpha| \approx 20°$ during the majority of the fast stroke phases, as can be seen in Figure 5.8c. At the end of the instroke this effect is increased further, where α changes sign before the outstroke starts. This change occurs as the wing leading edge moves mostly forward at the end of the instroke (visible especially on the upper wing), which in combination with the remaining twist results in a reversed α.

Perçin [36] showed that with increased freestream velocity the thrust force reduces considerably. This means that the reduction in angle of attack has a larger influence on the wing loading than the relatively minor increase in inflow velocity (see Figure 5.8d). As aerodynamic forces are reduced at fast climb, so is also the damping effect, which allows the leading edge to stroke further and reduces the passive incidence angle production during the instroke. The absence of peak incidence angle reduction during the outstroke is likely due to the dominant effect of the clap-and-peel which delays the trailing edge detachment.

The reduced loading can also be seen in the wing camber, which is on average reduced with faster freestream velocities. This also holds for the clap-and-peel phase, where the maximum camber ratio is reduced by approximately 2.5 % to $\varepsilon = 15$ % at $U_\infty = 2\,\mathrm{m\,s^{-1}}$. Looking at the deformation

plots, this can be linked to the increased wing gap which reduces the local curvature. The main reduction occurs however in the following out- and instroke, where ratios are now reduced by as much as 5 %. The recoil motion of the upper wing is still clearly visible, although slightly reduced.

5.2.3. Spanwise deformation

The spanwise wing deformation is again straightforward and does not show any large trends with changing freestream velocity. Only the main points summarized here while the spanwise parameter distributions of the upper wing are shown for completeness in the Section A.2.

The twist is in all cases largest at the tip, and peaks here slightly earlier than towards the root due to the difference in trailing edge detachment and recoil effect. The increase in incidence angle towards the tip it thereby lower than the increase in inflow angle, therefore the angle of attack increases slightly towards the wing tip. The wing camber also shows no new trends, with the main peak still occurring during the clap and peel at the tip. During the remaining cycle the highest magnitude still occurs further inwards.

5.3. Reduced frequency effects

To account for the reduction in thrust production with faster freestream velocities, the flapping frequency must be increased. This ratio is also described by the reduced frequency,

$$k = \frac{\pi f c}{U_\infty}, \tag{5.3}$$

where c is a length to obtain a dimensionless scaling parameter. Here $c = c_{mean} = 0.08\,\text{m}$. This parameter is typically used to describe the unsteadiness of a flow, where values above $k = 0.2$ are considered to be highly unsteady. The reduced frequency effectively describes how the absolved phase angle as half the length c is traveled, or in other words k is inversely proportional to the chord lengths traveled per flapping cycle. Another dimensionless scaling parameter used to describe unsteadiness, or specifically oscillating flow as shedding of vortices, is the Strouhal number,

$$St = \frac{f a}{U_\infty} = \frac{k a}{\pi c}. \tag{5.4}$$

Here, the mean chord is replaced by the flapping amplitude, a, which makes the Strouhal number proportional to the mean inflow angle over the cycle. As in this case both are fixed, k and St are directly proportional to another.

Four different cases were tested, which are the two previous climb cases with $f \approx 12\,\text{Hz}$, plus two cases with $f \approx 7.5\,\text{Hz}$, which were also tested at $U_\infty = 1\,\text{m s}^{-1}$ and $2\,\text{m s}^{-1}$ ($Re \approx 5300$). The resulting reduced frequencies can be seen in Table 5.1, all of these fall in the heavily unsteady range.

Table 5.1: Measured reduced frequency cases.

k [-]	U_∞ [m s^{-1}]	f [Hz]
0.93	2.00	7.40
1.53	2.00	12.18
1.90	1.00	7.56
3.04	1.00	12.09

The measured deformations showed however no clear scaling with the reduced frequency, instead the influence of the flapping frequency seems to outweigh those of the freestream velocity.

This can be seen in Figure 5.9. Agreeing with the argument above, the calculated angle of attack scales almost perfectly with k, but the absolute peaks in incidence angle (for in and outstroke), camber ratio and angle of attack of the upper wing are plotted to represent the general deformation trends. While the deformation appears to be increasing with k, θ_w and ε are generally higher at the reduced frequencies cases with $f \approx 12\,\text{Hz}$, which indicates that f has a dominant influence on the deformation. This also showed in the thrust measurements of Perçin [36], where at identical reduced frequencies the case with higher flapping frequency resulted in larger average thrust values.
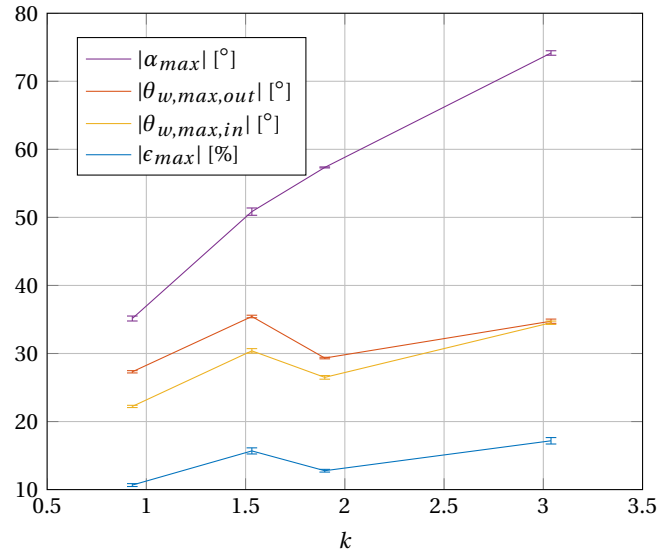
Figure 5.9: Peaks of upper wing parameters over different reduced frequencies.

The previous section on freestream velocity influences already showed that the incidence angle during the outstroke remained approximately constant with increasing U_∞. However, at $f \approx 7.5\,\text{Hz}$ the incidence angle does increase as the flow velocity is reduced, i.e. it shows to scale better with U_∞. This indicates that the dominant effect of the clap-and-peel is reduced at lower flapping frequencies, and that the deformation scales better with k.

Generally, this shows that the wing deformation is a result of a multitude of other non-linear, dynamic effects present in the DelFly. Further investigations using extended sweeps towards lower k could help to describe the different effects more thoroughly.

5.4. Pitch angle effects

Non-zero pitch angles will result in further asymmetrical behaviors, as now a freestream component and loading in z_w direction are introduced (Minor effects are already present in symmetric flow due to the dihedral angle as shown above). These asymmetric effects are studies using a sweep of pitch angles, while other parameters are fixed around $U_\infty = 1\,\text{m}\,\text{s}^{-1}$ and $f \approx 12\,\text{Hz}$. The exact values and other parameters are shown in Table 5.2.

Additionally, to the terms in- and outstroke, which described the wing movement towards and from the dihedral plane, with the introduced horizontal orientation the terms downstroke and upstroke are now used. These describe the wing movement relative to the horizon, and correspond inversely to in- and outstroke for the upper and lower wing.

Table 5.2: Measured pitch angle investigation settings.

θ_b [°]	U_∞ [m s^{-1}]	$U_{\infty,z}$ [m s^{-1}]	f [Hz]	k [-]
0	1.00	0.00	12.09	3.04
30	1.00	0.50	12.03	3.02
50	1.00	0.77	11.90	2.99
70	1.00	0.94	11.89	2.99

5.4.1. General deformation

The airfoil deformation at $r_w^* = 0.71$ is shown for two cases in Figure 5.10. The effect of the introduced asymmetry can clearly be seen and goes well beyond the minor asymmetries found in the climbing cases. Evident is for instance the rotation of the contact region, especially at the $\theta_b = 70°$ case. This rotation applies thereby to the entire clap-and-peel motion, which is otherwise relatively unaffected by the pitch angle change.
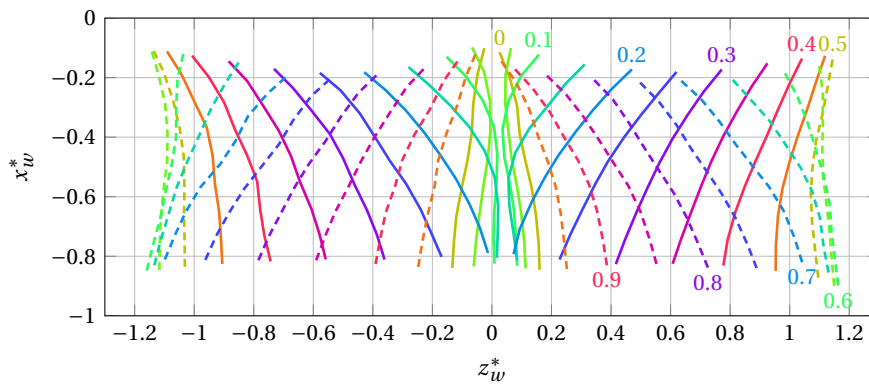
(a) 30° pitch angle. t^* is indicated for the upper wing.
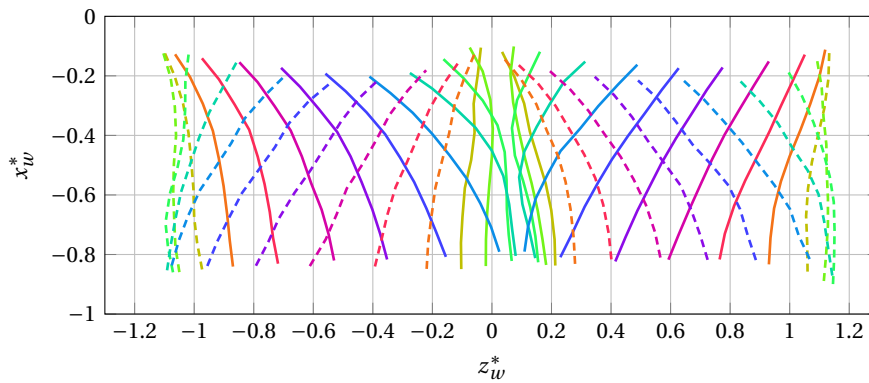
(b) 70° pitch angle.

Figure 5.10: Wing deformation at $r_w^* = 0.71$ over the flapping cycle due to different pitch angles. The upper wing can be seen in the right half, the outstroke cuts are dashed.

Furthermore, the wings now have an increased camber during the downstroke, while becoming almost flat during the upstroke. At the outer stroke reversal of the $\theta_b = 70°$ case the upper wing shows a slight S-shape, where the region towards the leading edge is already curved upwards while the trailing edge still has a negative camber. The wing gap also increases slightly for higher pitch angles, especially towards the tip trailing edge, where for $\theta_b = 70°$ the gap is around 1.5 mm. The clap-and-peel duration remains constant at around $\Delta t^* = 0.185$, as well as the stroke range where

no apparent asymmetry is visible in the maximum trailing edge deflections.

5.4.2. Parameter study

These asymmetric effects can also clearly be seen in the mean values of the deformation parameters, shown in Figure 5.11. During the stroke reversals, the mean incidence angle is positive, with mean angles of up to $\theta_w = 10°$ during clap and peel of the highest pitch setting. During the outer stroke reversal these mean angles are reduced to approximately half. The mean positive angles at higher pitch settings occur due to a faster reduction of the incidence angles during the upstroke, while during the downstroke the incidence angles reduce slower until after the stroke reversal. Further towards midstroke, the rates become more equal across the down and upstroke.

(a) Incidence angle.

(b) Camber ratio.

(c) Angle of attack.

(d) Inflow velocity magnitude.
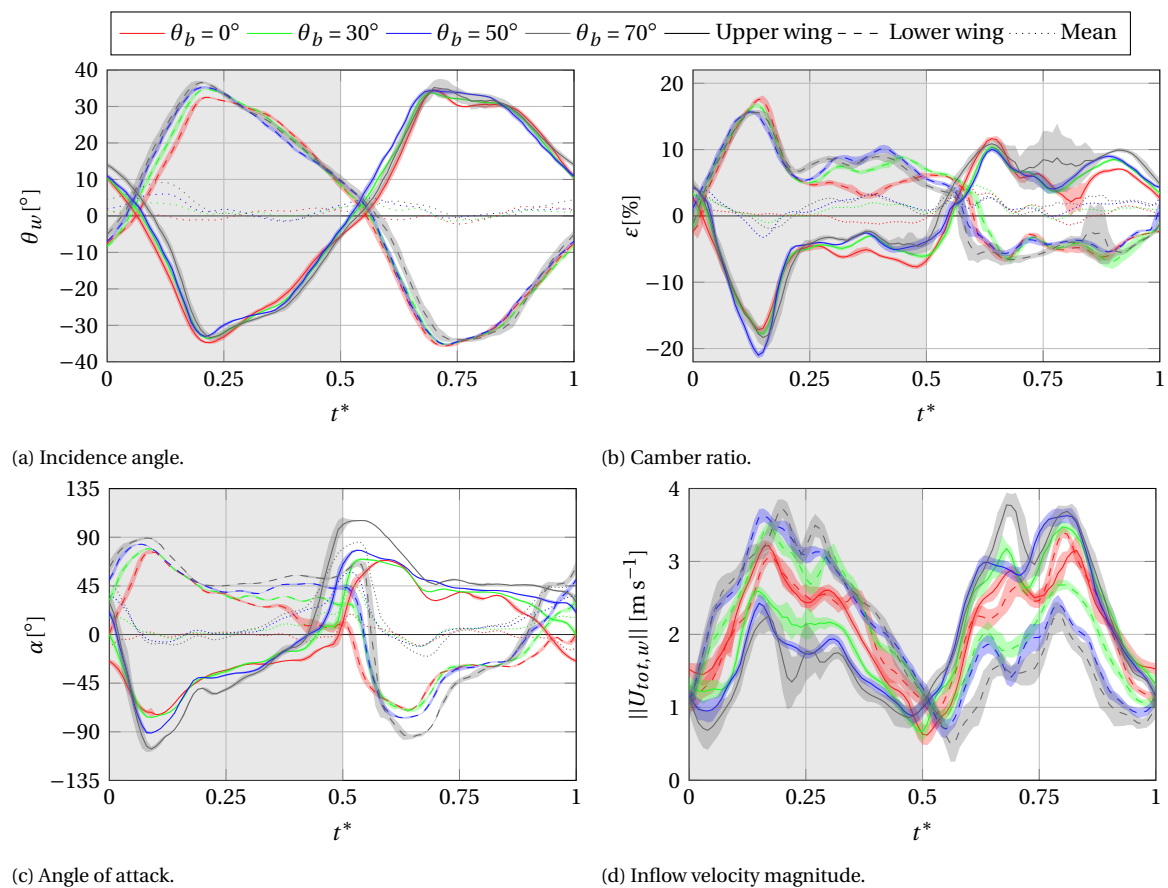
Figure 5.11: Airfoil and inflow parameters at $r_w^* = 0.71$ due to different pitch angles. The outstroke phase is shaded in grey, the instantaneous s.d. is shaded in the respective color.

The camber ratio is also mean positive over large parts of the flapping cycle for larger pitch angles. Here, the mean positive deformation shows however mostly during the fast stroke phase, which mean camber ratios of up to 5 % for $\theta_b = 70°$.

Reason for this can be seen in the changing angle of attack and inflow velocity magnitude between the up- and downstroke, plotted in Figure 5.11c and 5.11d. During the upstroke, the wings partially move with the freestream velocity, especially at larger pitch settings. This results in only a minor increase in the inflow magnitude, while the wing twisting leads to reduced angles of attack towards the stroke end. During the downstroke the increase in inflow magnitude is much larger, while the angle of attack maintains a large value for longer and is an almost constant at higher pitch angle settings. In previous studies this was shown to result in lower loading and chordwise defor-

mation during the upstroke, while the downstroke shows the opposite [20]. Interesting is thereby that this asymmetric loading has a much more minor effect on the incidence angle during the fast stroke phases, which shows a clear difference between the torsional and chordwise deformation in asymmetric conditions.

During the clap-and-peel the camber deformation appears to be still mostly affected by the specific motion. At the start of the clap-and-peel, the camber ratio is slightly positive, the upper wing quickly produces a negative camber, leading to a short duration of negative mean camber at faster flapping frequencies. Reason for this can be seen in the rotation of the clap-and-peel symmetry region, which leads to a sharper corner in the airfoil shape as the wings peel apart. The recoil effect at the start of the instroke also appears to be slightly reduced. The large s.d. in the upper wing camber ratio of the $\theta_b = 70°$ case between $t^* = 0.65$ and 0.8 (and some other cases) is likely due to undetected false point correspondences in some of the other cycles.

5.4.3. Spanwise deformation

The spanwise deformation is also after introduction of an asymmetric freestream component relatively straightforward, with values generally increasing from root to tip. One exception is thereby the angle of attack, as can be seen for the upper wing in Figure 5.12. Now, at larger pitch angles, at the end of the downstroke the angle of attack starts to reduce only at the wing tip, while in climb α became negative across the entire span. This shows that while the start of lift production is likely advanced into the end of the upstroke, it also ends earlier towards the wing tip. This effect could occur due to high loading of the wings during the downstroke that result in passive load reduction or feathering.

(a) $\theta_b = 30°$.   (b) $\theta_b = 70°$.
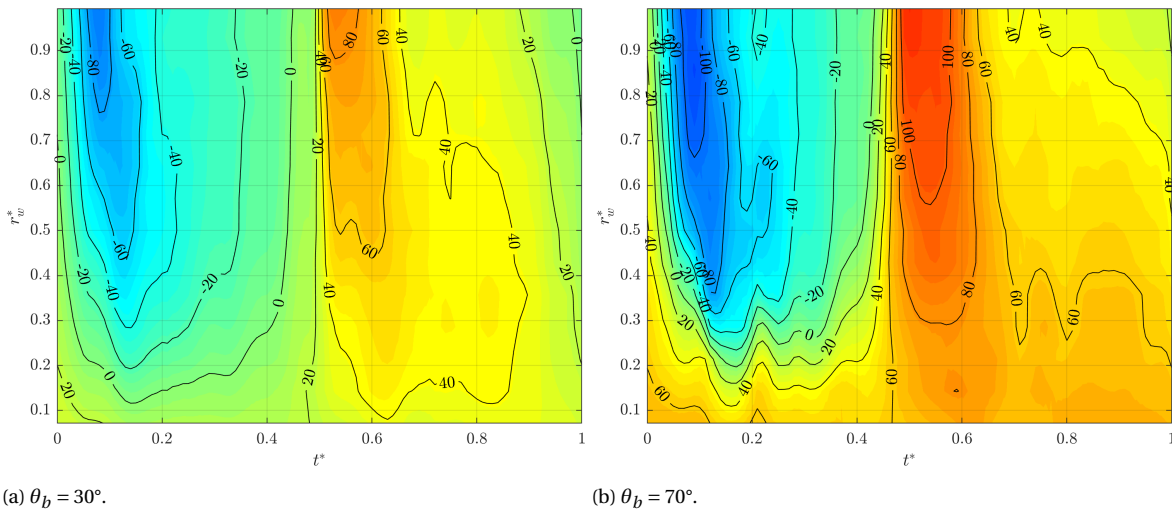
Figure 5.12: Upper wing angle of attack α [°] over span and time due to different pitch angles.

Furthermore, the S-shaped airfoil seen towards the upstroke end of the upper wing also changes in spanwise direction. Further towards the tip the wing maintains negative camber, while towards the tip the airfoil is completely inverted and shows positive camber already before the stroke reversal. This, and other spanwise parameters of the upper and lower wing are shown for in the Section A.3.

The torsional wave and recoil effect at start of the upper wing instroke reduces slightly with the pitch angle, which can be seen from the reduction of the initial incidence angle and camber ratio peak around $t^* = 0.65$ in Figure 5.11.

5.5. Forward flight

Horizontal forward flight is a more complex flight condition, where the pitch angle and flapping frequency must be matched to the forward flight velocity to achieve a force equilibrium between both thrust and drag, and lift and gravity. These settings were previously recorded by different free flight forward flight investigations [26, 32], which are now recreated in the windtunnel. The cases investigated here are shown in Table 5.3, where the sought free flight frequencies are shown with the subscript "$_{ff}$". The Reynolds number varies between $Re \approx 2600$ and 12000 for these cases.

Table 5.3: Replicated forward flight settings using tethered setup.

U_∞ [m s^{-1}]	θ_b [°]	$U_{\infty,z}$ [m s^{-1}]	f [Hz]	k [-]	f_{ff} [Hz]	k_{ff} [-]
0.50	70	0.47	13.10	6.59	13.00	6.53
1.12	50	0.85	11.99	2.70	11.89	2.67
1.63	40	1.05	11.25	1.74	11.07	1.71
2.26	30	1.13	10.15	1.13	10.11	1.12

The wing deformation now shows a number of different phenomena, where the 100 mm spanwise location again represents most of the wing. Cuts at this location are presented in Figure 5.13 and the airfoil and inflow parameters in Figure 5.14. The parameters in spanwise direction of the upper and lower wing are shown in the Section A.4.

The asymmetry between lower and upper wing thereby increases with the forward flight velocities, where the $U_\infty = 2.26\,\text{m s}^{-1}$ case shows large rotations at wing contact region and at the outstroke end, which can be seen in mean positive incident angles. This behavior was already noted for the pitch angle sweep, however now the angle is largest at the lowest pitch setting. This suggests that the increased freestream velocity during these phases has a larger influence than the pitch angle alone. In fact, the increase in asymmetry is at all times proportional to the increase in freestream component in z_b direction, $U_{\infty,z} = sin(\theta_b) \cdot U_\infty$, listed in Table 5.3. This holds for all deformation parameters, which suggests that the normal velocity is a better measure of the asymmetry than the pitch angle alone.

Noteworthy is also that the mean incidence angle is non-zero for a much larger part of the flapping cycle and is now of the same magnitude during the clap-and-peel and outer stroke reversal, while previously the latter was around half. This clearly shows that different non-linear effects are present as a result of the specific horizontal and vertical loading of the wings.

Reason for the increase in mean incidence angle in fast forward flight could be a coupling between the effect of flapping frequency decrease and freestream velocity increase. The approximately $-3\,\text{Hz}$ delta in flapping frequency and $1.75\,\text{m s}^{-1}$ delta in freestream velocity from the slowest to the fastest forward flight would account to around 5° and 9° reduction in incidence angle per wing for out- and instroke, respectively. While this is in line with the measurements of the oustroke, during the instroke the incidence angle between both wings is however reduced by approximately 26° instead of 18°. A possible reason for this large reduction could be the reduced relative flow velocity during the upstroke, as the wing moves in the direction of the freestream. During the pitch case this did however not show to have a larger influence on the incidence angle, instead mostly affected the camber ratio.

In spanwise direction the of incidence angle at faster velocities is thereby almost linearly towards the tip. The torsional wave is considerably reduced at faster flight velocities, which is visible in the reduction of the initial peak during the instroke and also from the 3D shape shown in Figure
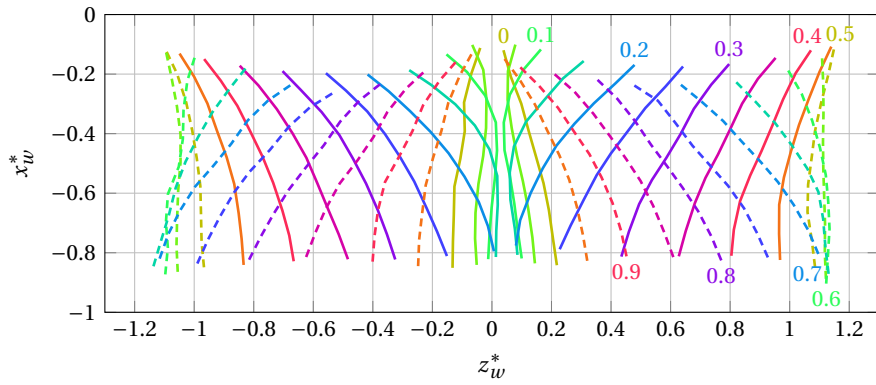
(a) 0.50 m s^{-1} forward flight at 70° pitch angle. t^* is indicated for the upper wing.
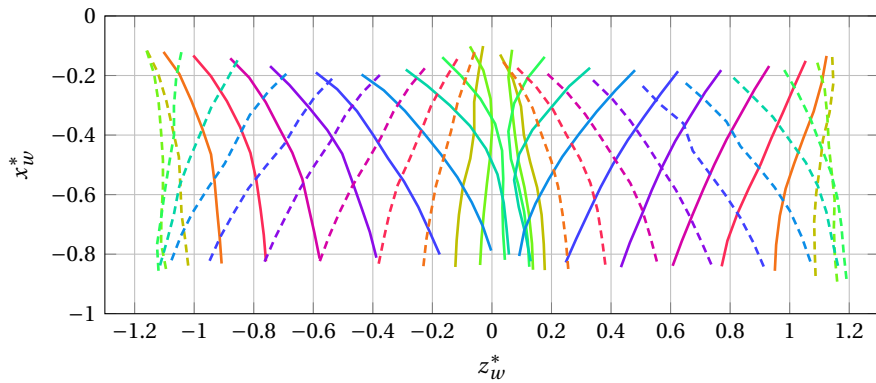
(b) 1.12 m s^{-1} forward flight at 50° pitch angle.
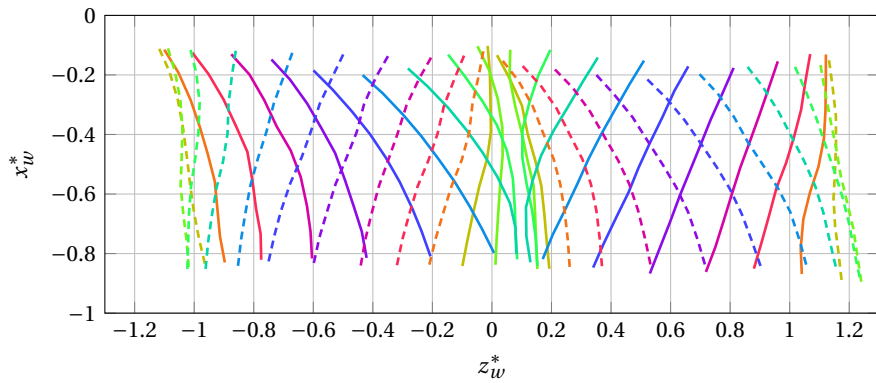
(c) 2.26 m s^{-1} forward flight at 30° pitch angle.

Figure 5.13: Wing deformation at $r_w^* = 0.71$ over the flapping cycle due to different forward flight velocities. The upper wing can be seen in the right half, the outstroke cuts are dashed.

??.

During the clap-and-peel the incidence angles agree relatively well with the previously noted behavior. The increasing rates are very similar across all cases, with the upper wing initially having lower rates, similar what was previously noted for the pitch angle cases due to an extended range of higher angle of attack. The peak is slightly advanced for the fast forward flight cases, which is in line with the trailing edge detachment, which shifts from approximately $t^* = 0.185$ to 0.165 at this spanwise location, which was previously noted to occur for reduced flapping frequencies. The wing gap increases by around 0.4 mm with the forward velocity, however the fastest case shows a very small gap towards the wing tip. The wing heave also becomes asymmetric for faster forward veloci-

(a) Incidence angle.

(b) Camber ratio.

(c) Angle of attack.

(d) Inflow velocity magnitude.
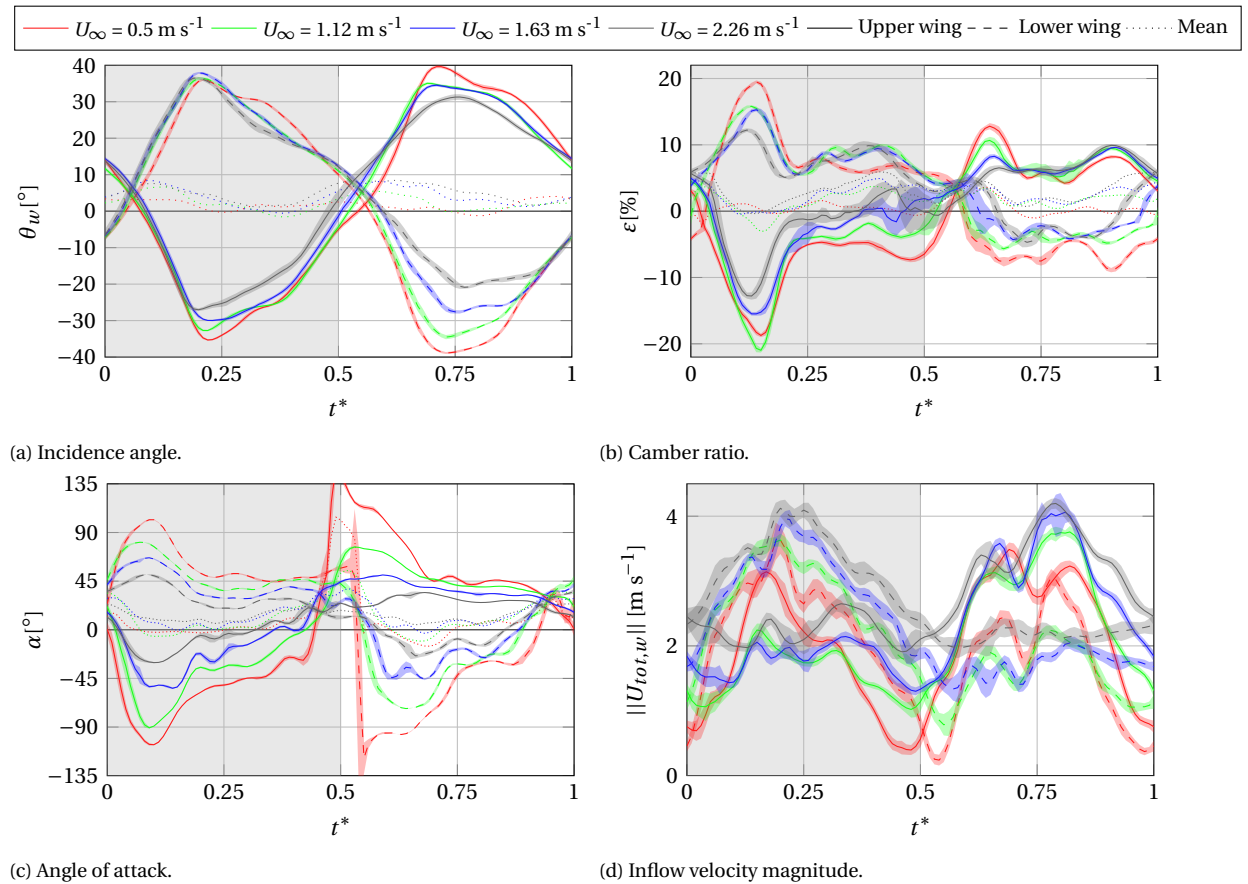
Figure 5.14: Airfoil and inflow parameters at $r_w^* = 0.71$ due to different forward flight velocities. The outstroke phase is shaded in grey, the instantaneous s.d. is shaded in the respective color.

ties, where the lower wing heaves considerably more and the upper less. It is assumed that this is a consequence of the rotation of the contact region, which angles the lower wing further downwards for its out- or downstroke. This results in an asymmetric behavior, where the wings are heaved more during the downstroke. This also indicates higher loads during this phase, which is in line with the required lift production.

The assumption that the clap-and-peel behavior is largely unaffected is also supported by the measured camber deformation. While initially the both wings have positive camber ratios, between $t^* = 0.05$ and $t^* = 0.18$ the camber ratio is almost symmetric which speaks for an unchanged LEV production. The reduced magnitude can again be linked to the reduction in flapping frequency and reduced freestream velocity, which accounts for around 3 % and 2 % reduction per wing, respectively. The $\theta_b = 50°$ case is the only outlier for this assumption, where the camber of the upper wing during peel increases very abruptly. This could be due to the specific contact region rotation, which results in larger peel angles in this case.

For the remaining cycle, the camber deformation agrees relatively well with the combination of the previous studies. Fast forward flight generally results in larger camber asymmetries, but reduced delta between the upper and lower wing. Specifically, the camber ratio during downstroke is similar for all cases, while during the upstroke the camber ratio reduces with the pitch angle, approaching zero for $\theta_b = 30°$. This is a common behavior in insect flight [20, 48, 50]. Thereby, the upper wing airfoil again has an S-shape towards the end of the outstroke (see Figure 5.13c), which was previously already observed. Again, this effect increases strongly in spanwise direction, where at the tip the

wing is curved upwards over the entire chord. This suggests that the wing is here already beginning to produce lift and possibly a LEV growing from the tip of the upper wing surface, which is noted in numerical simulations of flapping wings [20]. This effectively moves the start of the lift producing phase of the upper wing forward. This specific shape thereby makes the determination of the camber direction difficult, thus leads to larger s.d. shown in the parameter plot.

The computed angle of attack also shows an advanced lift production, as it reverses the approximately at the same instance as the camber. This large angle of attack reduction during upstroke is in line with the pitch angle study. Again, the inflow velocity magnitude is relatively low due to the stroke component in freestream direction. Compared to this, during the wing the angle of attack remains much higher and mostly constant in time, and the inflow velocity magnitude increases considerably.

Interestingly, across most forward flight velocities the inflow magnitudes are relatively identical. Except for the $U_\infty = 0.5\,\mathrm{m\,s^{-1}}$ case, during the upstroke it is almost constant at $||U_{tot,w}|| \approx 2\,\mathrm{m\,s^{-1}}$, while during the downstroke it peaks at $||U_{tot,w}|| \approx 4\,\mathrm{m\,s^{-1}}$. This appears to be due to the specific combination of the pitch angle, freestream velocity and flapping frequency.

Another argument for the occurrence of early lift production can be seen in the alignment of the clap-and-peel motion with the flight direction. The general motion is in line with that of the hover condition, which suggests that the effectiveness in force production is not considerably reduced. This will likely result in a large portion of the required thrust being produced during this phase. This could reduce the need for the wings to produce thrust during upstroke, as it is assumed to occur for single wing fliers [50]. This is also in line with the main production of tip vortices in the $\theta_b = 30°$ case as measured by Martínez Gallar [32]. Thrust production during upstroke results in some negative lift component, which will be detrimental for flight efficiency and performance. This suggests that the wing-wing interaction of the DelFly and resulting deformation leads to high efficiency also in forward flight.

5.6. Descending flight and reverse freestream velocity

As a last brief discussion, the descending flight case is analyzed. Here, the DelFly was positioned facing away from the windtunnel so that the freestream velocity simulates the MAV in descent. The tested settings are listed in Table 5.4, with the flapping frequency kept approximately at $f = 12\,\mathrm{Hz}$. The lower two velocities are assumed to be in a range typical for the DelFly, with the $U_\infty = -2\,\mathrm{m\,s^{-1}}$ case being more extreme. As in the climbing flight, the flapping frequency would thereby need to be matched with the flight velocity and mass to represent true descending flight.

Table 5.4: Measured descending flight cases.

U_∞ [m s^{-1}]	f [Hz]	k [-]
-0.5	11.83	-5.95
-1.0	12.04	-3.03
-2.0	12.03	-1.51

While setting the correct flapping frequency during the recording process, it was already noted that the frequency did not remain constant at faster descent. Additional postprocessing of the $-2\,\mathrm{m\,s^{-1}}$ case showed a frequency increase from around 11.5 Hz to 12.5 Hz over the measurement period. The change in frequency makes the used cyclic prediction considerably worse, resulting in

60 % lost points on the upper wing during the instroke. The slower cases lie closer to the typical tracking performance shown in Section 4.3.1 with lost point ratio peaks of 20 %. Consideration of the changing flapping frequency during the processing did however not increase the detection rate, which suggests that the general wing motion starts to vary more rapidly at fast descent cases, which makes any form of point tracking more difficult.

The poor processing performance can be seen in Figure 5.15c, which shows several unnatural edges in the airfoil shapes which can be linked to lost points. All results must therefore be treated with care. The other two cases shown in Figure 5.15 show much better measurements, only having a minor kink at $t^* = 0.45$ in the upper wing. The discussion will therefore focus on these cases.
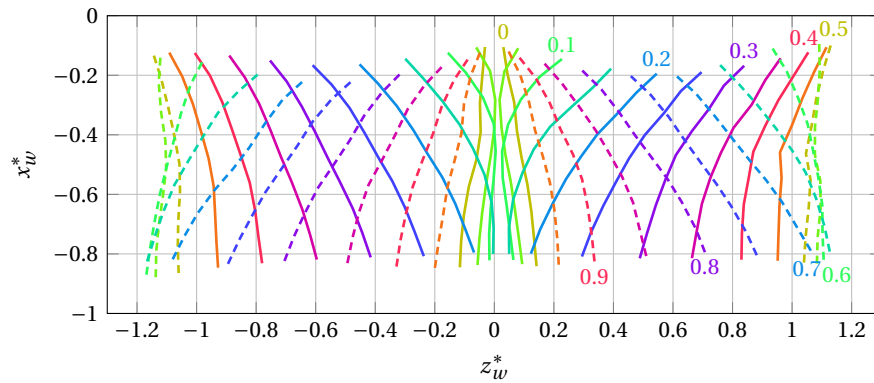
(a) $-0.5\,\mathrm{m\,s^{-1}}$ descent.
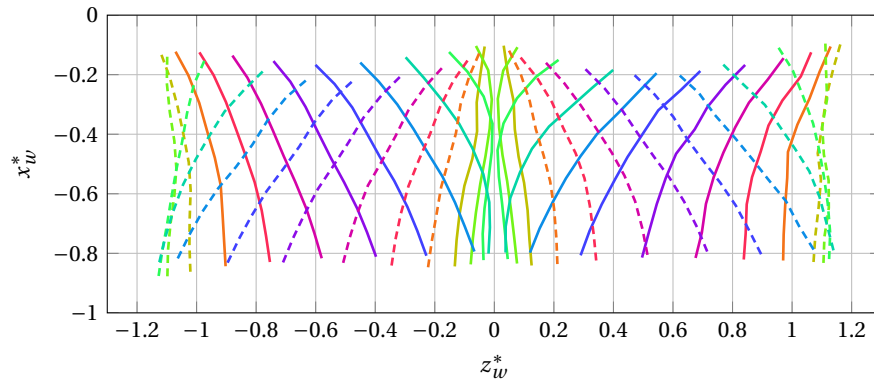
(b) $-1\,\mathrm{m\,s^{-1}}$ descent.
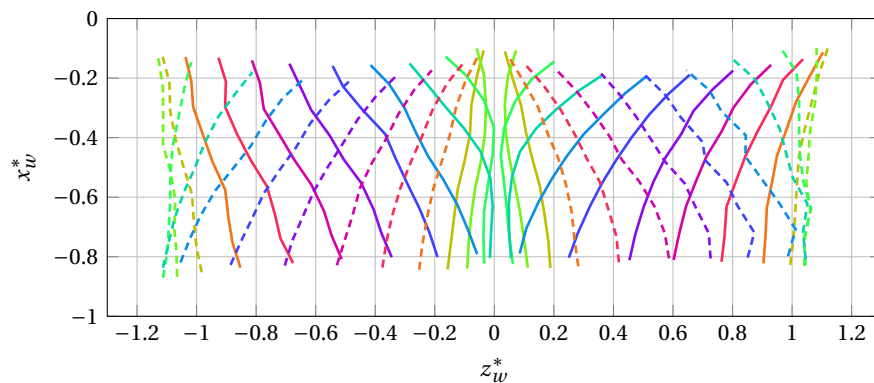
(c) $-2\,\mathrm{m\,s^{-1}}$ descent.

Figure 5.15: Wing deformation at $r_w^* = 0.71$ over the flapping cycle due to different descent velocities. The upper wing can be seen in the right half, the outstroke cuts are dashed.

When comparing the wing deformations to the hover case, the present asymmetries are mostly switched between the wings, for instance now the lower wing heaves more. In fact, as the DelFly was rotated around the z_b axis to achieve reverse inflow, the upper and lower wings were flipped so that the markers are now on the left DelFly side to keep them in the camera view, which placed the previously upper wing now the in the position of the lower wing. This shows that some asymmetries are linked to the specific wing manufacturing, e.g. differences in sanding the inner leading edge stiffener ends. This appears to affect mostly wing heave and camber, however for instance not the camber recoil effect which is still stronger in the new upper wing.

The general motion between the two slower cases is nearly identical. The clap-and-peel duration lies at around $\Delta t^* = 0.165$, which is slightly below the hover duration, continuing the trend measured in the climbing flight section. In contrast to that, the wing gap increases in descent to distances around 1 mm, thus breaks the trend. The stroking motion and wing heave also remains similar between the two cases. At $-2\,\mathrm{m\,s^{-1}}$ descent the clap-and-peel increases again to $\Delta t^* = 0.175$, while the wing gap continues to increase to around 1.5 mm.

Figure 5.16 shows the airfoil parameters over the cycle, where the large s.d. of the $U_\infty = -2\,\mathrm{m\,s^{-1}}$ case again shows large variations over the measurement duration and potentially incorrectly corresponded points. The parameters in spanwise direction of the upper wing are shown for in the Section A.4.

(a) Incidence angle.

(b) Camber ratio.

(c) Angle of attack.

(d) Inflow velocity magnitude.
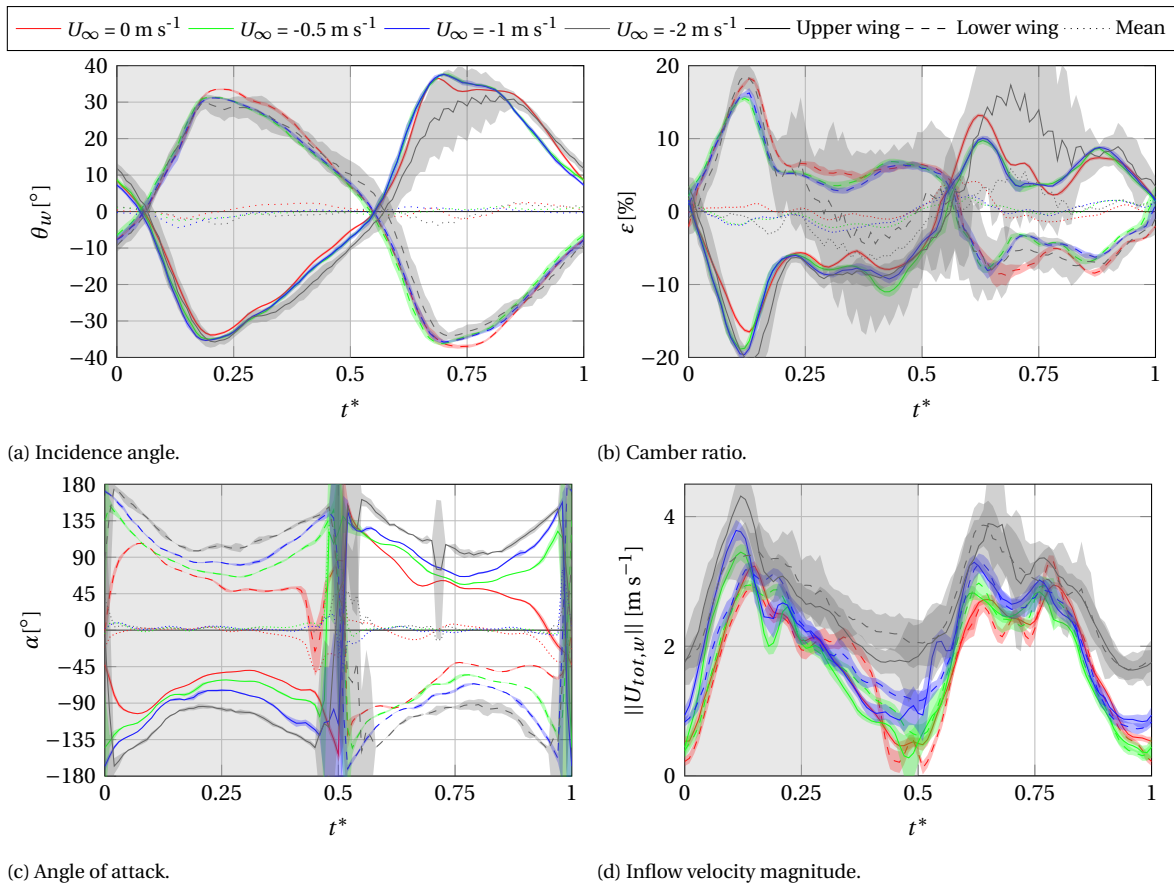
Figure 5.16: Airfoil and inflow parameters at $r_w^* = 0.71$ due to different descent velocities. The outstroke phase is shaded in grey, the instantaneous s.d. is shaded in the respective color.

Both slower descent cases are again almost identical in incidence angle and camber ratio, with

only the angle of attack showing larger variations due to the changed freestream velocity. Apart from the difference in mean values due to the reversed wings, the peaks in camber ratio and incidence angle are approximately identical to those of the hover case, the largest exception being the reduced increase in camber ratio of the upper wing at the start of the instroke. The magnitude and temporal variation are now much more similar between the wings. This also holds for the incidence angle variation, which no longer shows a distinct peak at the start of the instroke.

The large s.d. makes closer investigation of the faster descent case meaningless, however some minor points can be noted. First, the change in incidence angle lags slightly behind the other cases. This can be seen especially at the start of the outstroke, which is the most reliable phase as the least points are lost. But lag also shows in the slower reduction of incidence angles towards the stroke reversals. Apart from this lag, the general clap-and-peel duration is very similar to the hover case, suggesting that also here the phenomena functions comparably. For the remaining cycle, and in spanwise direction, no clear observations of changed deformation can be made. Only the angle of attack thereby remains considerably larger compared to the slower descent cases, in fact $|\alpha| > 90°$ at all times, meaning the wing experiences reverse flow neglecting the induced velocities.

<div style="text-align: right; font-size: 3em;">6</div>

Conclusions and recommendations

6.1. Conclusions

6.1.1. Measurement procedure

A detailed literature review of previous wing deformation studies and their approaches was carried out to find the most suitable measurement approach. The findings were used in conjunction with the outcome of three trial method assessments for a trade-off study. Based on this, it was decided to use a point tracking approach with background illumination, which allows simultaneous measurement of both wings with only a single sided setup. Furthermore, the intrusion of this approach is minimal due to very little weight added to the wings. This outweighs the relatively large development effort for a purpose build point tracking algorithm.

A measurement setup was then developed which co-aligns a camera pair together with the DelFly and the background light to maintain adequate viewing axes of the wings which undergo large stroke angles. The DelFly is thereby oriented on its side to allow easier rotation, the influence of the misalignment of the gravitational force is assumed to be negligible compared to larger flapping accelerations and aerodynamic forces. The point tracking algorithm makes use of the known topology of the 136 markers on each wing to enhance the temporal tracking, which allowed reliable tracking of overlapping points even though only two views are available. On average 3.4 % of points are lost and very few false point matches occur. The general accuracy is estimated to be around 0.25 mm or 0.18 % of the half span based on reference sphere measurements.

This setup and measurement algorithm may be useful in the future for investigating different flight conditions or other DelFly variations and may also be an important tool for improving wing designs and generating further validation data for numeric methods.

6.1.2. Wing deformation

The carried-out measurements show a considerable change in wing deformation for flight conditions with different freestream settings and flapping frequencies.

The flapping frequency was found to have the largest influence on the wing deformation. With increasing stroke velocities, movement of the leading and especially trailing edges in stroke direction is reduced while the leading edge heaving motion is increased. The clap-and-peel phase, ending at the trailing edge separation, makes up a slightly larger amount of the cycle as the flapping frequency is increased. It was noted that apart from a region close to the root trailing edge the wing surfaces do not make contact during this phase, especially at higher flapping frequencies. Previously this buffer was noted only close to the leading edges.

The maximum camber ratios during this phase is increased considerably during the clap-and-peel, but remains mostly unchanged for the remaining cycle. The incidence angle also increases with the flapping frequency. Reason for these larger deformations can be attributed to higher inertial and aerodynamic forces. The upper wing thereby has a slightly advanced peak at the higher flapping frequency case. This peak coincides with a torsional wave traveling in spanwise direction. The camber ratio also shows an increased peak at this instance, which is similar to the beneficial recoil effect often found in insects [48].

The absence of this behavior on the lower wing shows that the wing motion is asymmetric also in hovering flight. Different variations of the wing choice and orientation showed thereby that the torsional wave and recoil are indeed only present on the upper wing. This difference could be a result of the dihedral angle, which influences aerodynamics and wing tension, but may to an extent also occur due to intrusion of the support or diffusion screen. Other effects, such as asymmetric wing heave and camber production can however be linked to the specific wing, thus suggests their origin in manufacturing inaccuracies.

The climbing flight velocity represented by increasing freestream velocity has a smaller influence on the deformation. This holds especially for the clap-and-peel phase, where only minimal camber reductions were found, and the incidence angle is mostly unaffected during the entire outstroke. A more evident change in the clap-and-peel phase is the increasing wing gap, which reaches values of around 1.3 mm, while the duration reduces slightly. Outside this phase, the camber ratio and incidence angle are reduced slightly with increasing climbing rate, which is assumed to be driven by lower wing loading due to reduced angle of attack, as also measured by thrust measurements of Perçin [36]. The recoil and torsional wave are also reduced at faster freestream velocities.

While the angle of attack is closely proportional to the reduced frequency and Strouhal number, the higher influence of the flapping frequency does not result in a direct scaling of the deformation with the reduced frequency. This is especially visible for the incidence angle during the clap-and-peel, which at $f = 12\,\text{Hz}$ did not scale with U_∞, thus neither with k. Towards lower f, U_∞ does however increase its influence thus the deformation scales closer with k.

Varying the freestream direction by setting a body pitch angle introduces a large asymmetry between the upper and lower wings. During the stroke reversals the wings are aligned with the flow, which holds especially for the clap-and-peel motion. Towards the tip trailing edge, the wing gap is thereby increased considerably. In the wing camber the asymmetry is especially prominent in the fast stroke phases. During the upstroke the wings become flatter while during the downstroke the camber is increased. This behavior is commonly seen in natural fliers and partially assumed to be due to changed inflow velocity due to a stroke component in freestream direction. The upper wing thereby shows an advanced camber reversal at the end of the upstroke which leads to an S-shaped airfoil around mid-span.

To an extent the deformations in forward flight follow the trends of the isolated parameters, however as assumed they are not exactly a linear combination. The clap-and-peel deformation agrees best with a superposition of the deformations due to the individual parameters, indicating that the produced LEV has a dominant effect over the asymmetrical freestream velocity and that the motion likely remains similarly effective as in hover. Only the motion symmetry plane is changed, which is passively rotated to align more with the freestream.

Outside the clap-and-peel, the wing asymmetry goes beyond the values expected from the pitch angle study. Asymmetries are thereby largest at fast forward-flight velocities and lowest pitch angles, which shows that asymmetric deformations are not directly proportional to pitch angle but better

represented by the normal freestream component. Here, the incidence angle asymmetry extends to most of the flapping cycle, and the reduction of incidence angle delta between the wings lies above the isolated effects of flapping frequency and freestream change. The camber deformation in forward fight agrees better with the parameter study, now extended regions of reversed camber are present during the upstroke. These coincide well with the reversed angle of attack, which indicates very low wing loading during upstroke at fast forward flight. Reason for this is again seen in lower relative velocity, and potentially a reduced need for thrust production during upstroke as the produced force of the clap-and-peel motion is closely aligned with the flight direction.

The final descending flight study showed little variations in wing deformations at low velocities, with camber and incidence angle remaining mostly as in hovering flight. The clap-and-peel duration thereby decreases further which is in line with the climbing flight trend, while the wing gap behaves oppositely. At $-2\,\mathrm{m\,s^{-1}}$ descend velocity, large flapping frequency variations occur. These result in a large amount of lost points during the processing, making a detailed analysis impossible.

6.2. Recommendations

Several possibilities exist to extend the understanding of flapping-wing deformations and the general performance of flapping-wing flight after this project. Some parameters could still be analyzed, such as leading edge bending in stroke plane and wing accelerations, and potentially a modal analysis and strain measurements can be carried out. The combination with measured flow field data (instead of the rudimentary calculation of inflow velocity and angle of attack) and force data would also allow for a better understanding of force production and wing loading. Thereby it may be advisable to extend the measured reduced frequency sweep and include lower values where the wing-wing interactions become less dominant [36].

Apart from this, the large range of measured data together with the previously acquired flow data makes a complete dataset to validate a numerical model of the DelFly in forward flight. The convection of vortices with the freestream velocity away from the DelFly makes forward flight a better validation case compared to the previously measured hovering flight condition.

Both the numerical model, and a better understanding of the flapping wing phenomena will allow improvements to the design of the DelFly and other flapping-wing MAV, enabling greater performance and efficiency.

While the measurements were overall very successful, some modifications and improvements to the measurement setup could be made. First, the dataset should be extended to incorporate different wing sets to eliminate the manufacturing uncertainty. Furthermore, a different support, or true free flight measurements, could be used to investigate or eliminate its interference, including its influence on the currently absent lower wing recoil. The influence of the diffusion wall may be interesting to be investigated and corrected for. A better detection of the body coordinate system may also be helpful and could be achieved using additional fuselage markers and/or prior recordings of freestream and body aligned calibration plates. Lastly, adding further cameras to the setup could reduce the number of lost points and also allow for more complicated movements such as larger wing twisting or stroke angles, and reduce the need to fix the body position relative to the cameras, thus allowing larger body pitch angles and free flight measurements.

Some improvements to the processing algorithm could also be made. Incorporation of the leading edge stiffener to the tracking process using epipolar geometry would extend the measured wing region. The point tracking may be improved by further tweaking the velocity prediction parameters, which could include incorporating further knowledge of the typical marker motions. Considerable improvement of the tracking may also be possible by directly incorporating the marker

topology into the track prediction instead of using it only to correct the temporal prediction. An improved point center detection may thereby enable more accurate marker measurements and allow for larger overlapping of markers. Improved triangulation techniques such as incorporation of a bundle adjustment method could also allow for higher measurement accuracy.

A
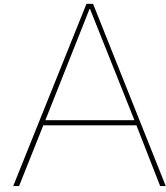
Span and timewise parameter plots

A.1. Hovering flight
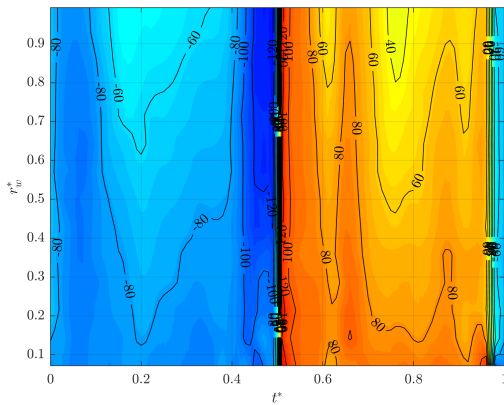
(a) $f = 7.5\,\text{Hz}$.
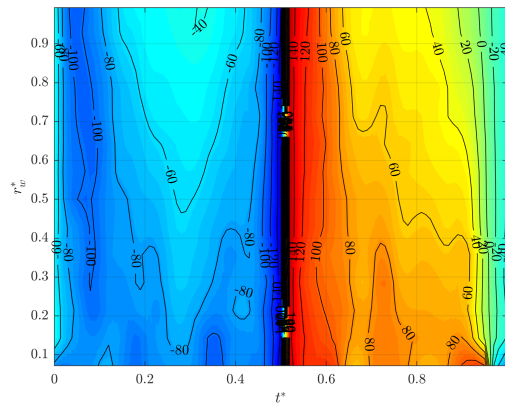
(b) $f = 12\,\text{Hz}$.

Figure A.1: Upper wing angle of attack α [°] over span and time in hover due to different flapping frequencies.
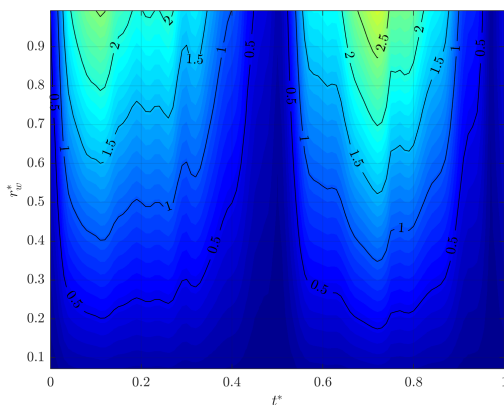
(a) $f = 7.5\,\text{Hz}$.
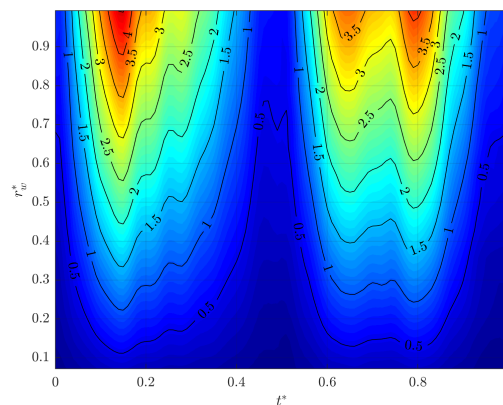
(b) $f = 12\,\text{Hz}$.

Figure A.2: Upper wing inflow velocity magnitude $||U_{tot,w}||$ [m s^{-1}] over span and time in hover due to different flapping frequencies.

A.2. Climbing flight
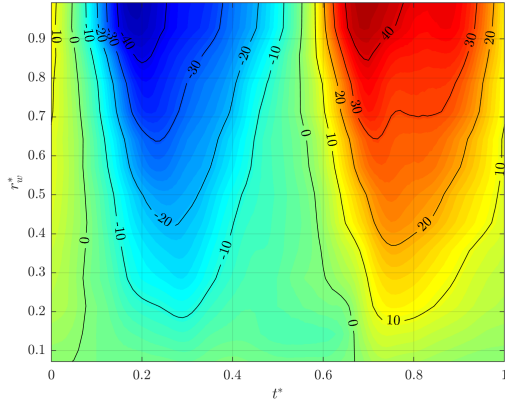
(a) $U_\infty = 1\,\mathrm{m\,s^{-1}}$.
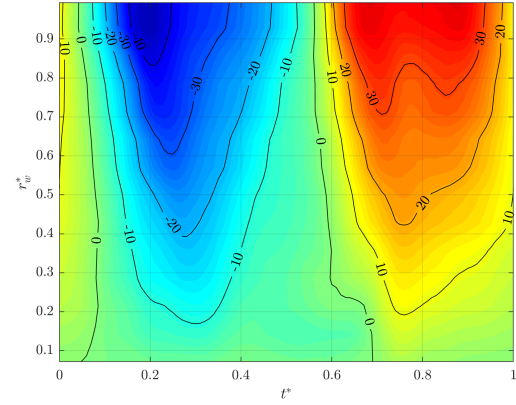
(b) $U_\infty = 2\,\mathrm{m\,s^{-1}}$.

Figure A.3: Upper wing incidence angle θ_w [°] over span and time in hover due to different freestream velocities.
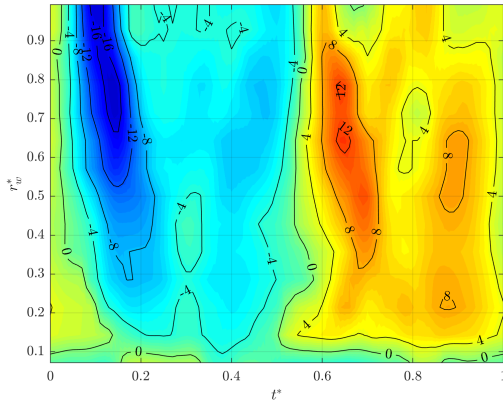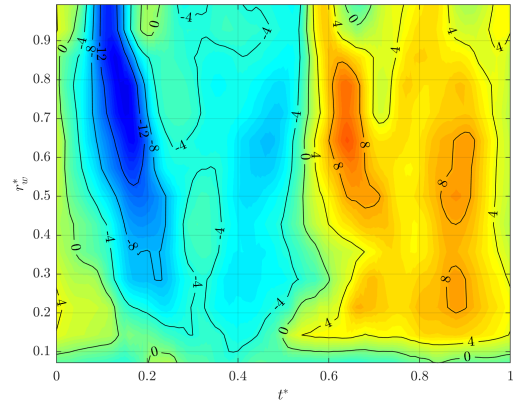
(a) $U_\infty = 1\,\mathrm{m\,s^{-1}}$.

(b) $U_\infty = 2\,\mathrm{m\,s^{-1}}$.

Figure A.4: Upper wing camber ratio ε [%] over span and time in hover due to different freestream velocities.
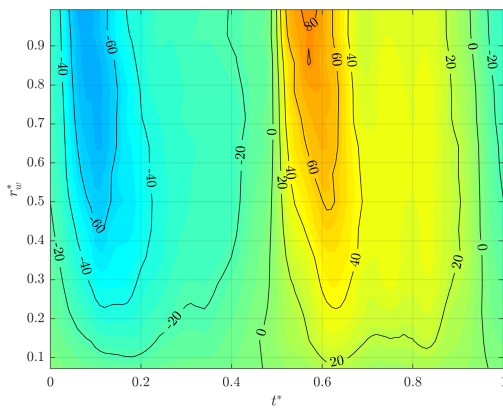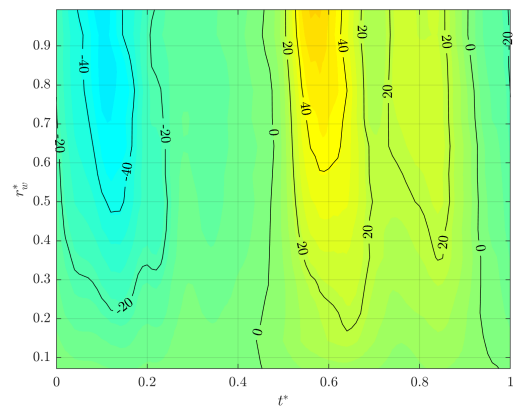
(a) $U_\infty = 1\,\mathrm{m\,s^{-1}}$.

(b) $U_\infty = 2\,\mathrm{m\,s^{-1}}$.

Figure A.5: Upper wing angle of attack α [°] over span and time due to different freestream velocities.
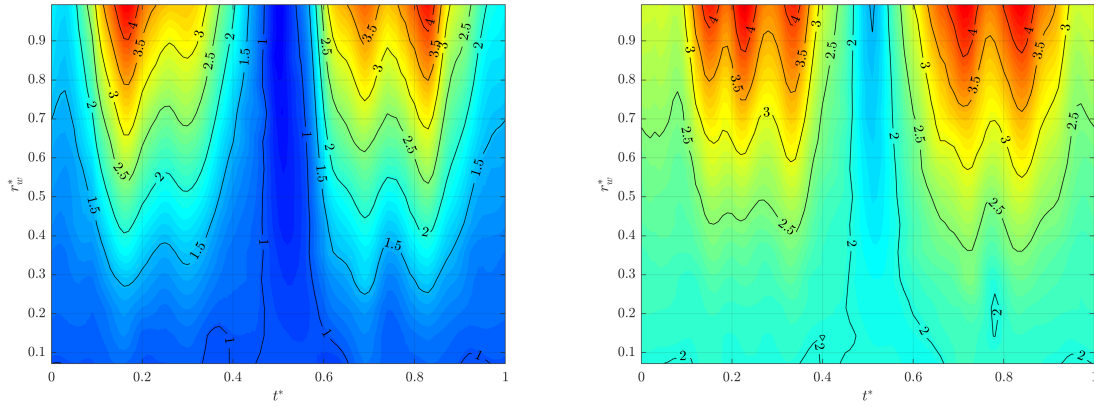
(a) $U_\infty = 1\,\mathrm{m\,s^{-1}}$.

(b) $U_\infty = 2\,\mathrm{m\,s^{-1}}$.

Figure A.6: Upper wing inflow velocity magnitude $||U_{tot,w}||$ [$\mathrm{m\,s^{-1}}$] over span and time due to different freestream velocities.

A.3. Pitch angle effects
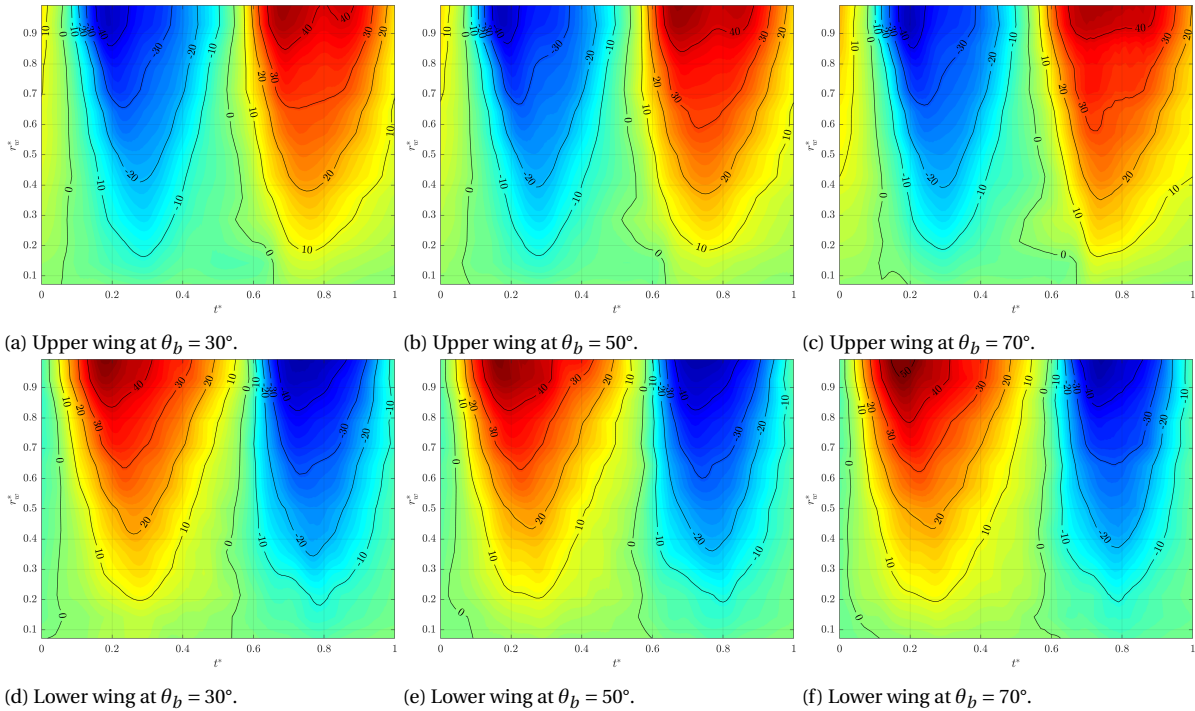
(a) Upper wing at $\theta_b = 30°$.

(b) Upper wing at $\theta_b = 50°$.

(c) Upper wing at $\theta_b = 70°$.

(d) Lower wing at $\theta_b = 30°$.

(e) Lower wing at $\theta_b = 50°$.

(f) Lower wing at $\theta_b = 70°$.

Figure A.7: Upper and lower wing incidence angle θ_w [°] over span and time due to different pitch angles.

(a) Upper wing at $\theta_b = 30°$.

(b) Upper wing at $\theta_b = 50°$.

(c) Upper wing at $\theta_b = 70°$.

(d) Lower wing at $\theta_b = 30°$.

(e) Lower wing at $\theta_b = 50°$.
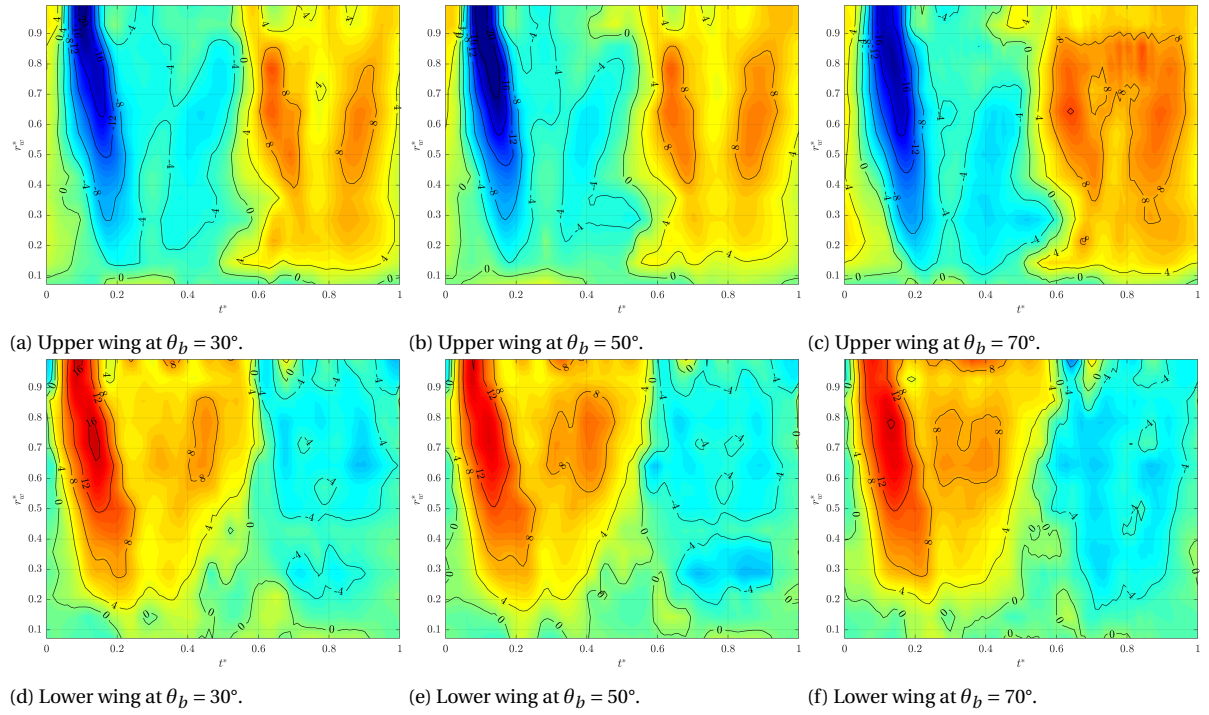
(f) Lower wing at $\theta_b = 70°$.

Figure A.8: Upper and lower wing camber ratio ε [%] over span and time due to different pitch angles.

(a) Upper wing at $\theta_b = 30°$.

(b) Upper wing at $\theta_b = 50°$.

(c) Upper wing at $\theta_b = 70°$.

(d) Lower wing at $\theta_b = 30°$.

(e) Lower wing at $\theta_b = 50°$.
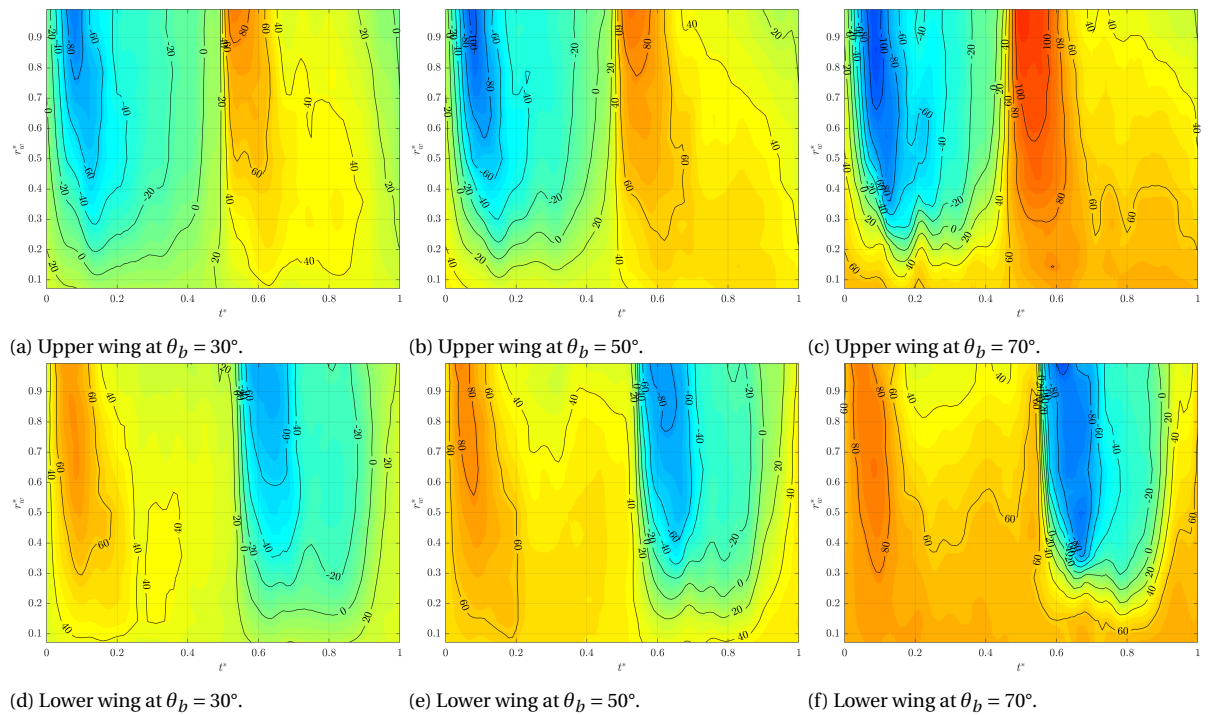
(f) Lower wing at $\theta_b = 70°$.

Figure A.9: Upper and lower wing angle of attack α [°] over span and time due to different pitch angles.

(a) Upper wing at $\theta_b = 30°$. (b) Upper wing at $\theta_b = 50°$. (c) Upper wing at $\theta_b = 70°$.

(d) Lower wing at $\theta_b = 30°$. (e) Lower wing at $\theta_b = 50°$. (f) Lower wing at $\theta_b = 70°$.
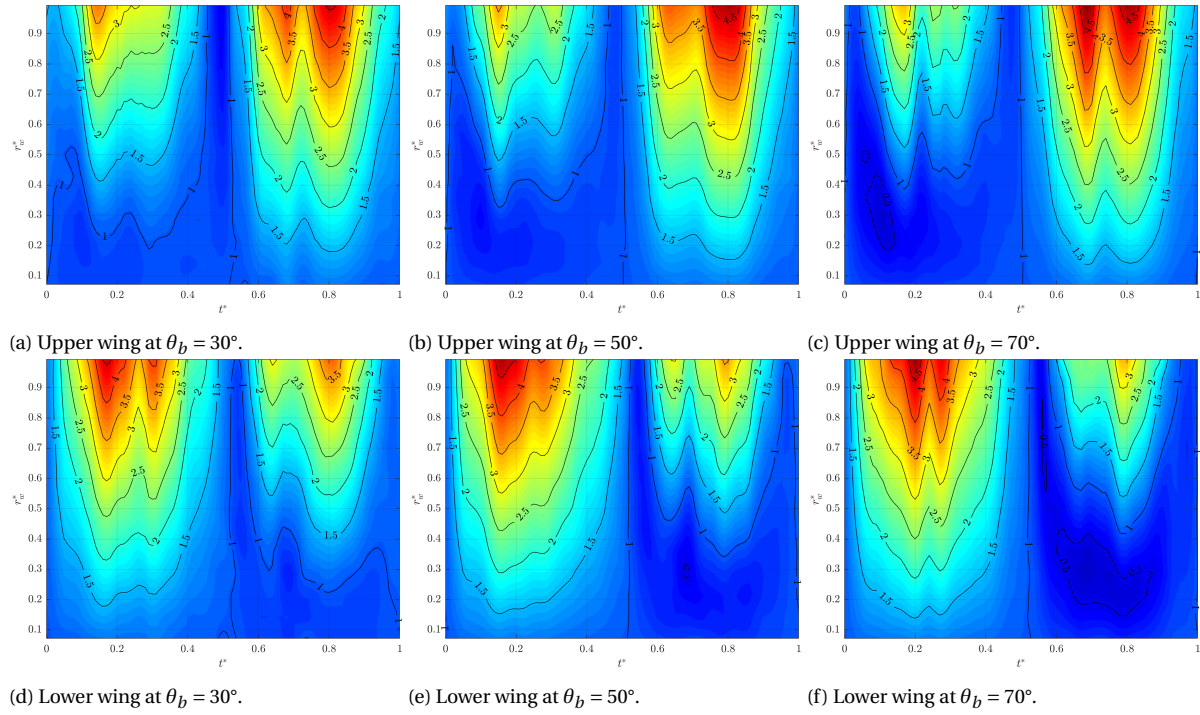
Figure A.10: Upper and lower wing inflow velocity magnitude $||U_{tot,w}||$ [m s^{-1}] over span and time due to different pitch angles.

A.4. Forward flight

The tip of the lower wing in $2.26\,\text{m s}^{-1}$ forward flight velocity was tracked unsuccessfully. The airfoil and inflow parameters during the outstroke show therefore incorrect values.

(a) Upper wing at $U_\infty = 0.5\,\text{m s}^{-1}$. (b) Upper wing at $U_\infty = 1.12\,\text{m s}^{-1}$. (c) Upper wing at $U_\infty = 2.26\,\text{m s}^{-1}$.

(d) Lower wing at $U_\infty = 0.5\,\text{m s}^{-1}$. (e) Lower wing at $U_\infty = 1.12\,\text{m s}^{-1}$. (f) Lower wing at $U_\infty = 2.26\,\text{m s}^{-1}$.
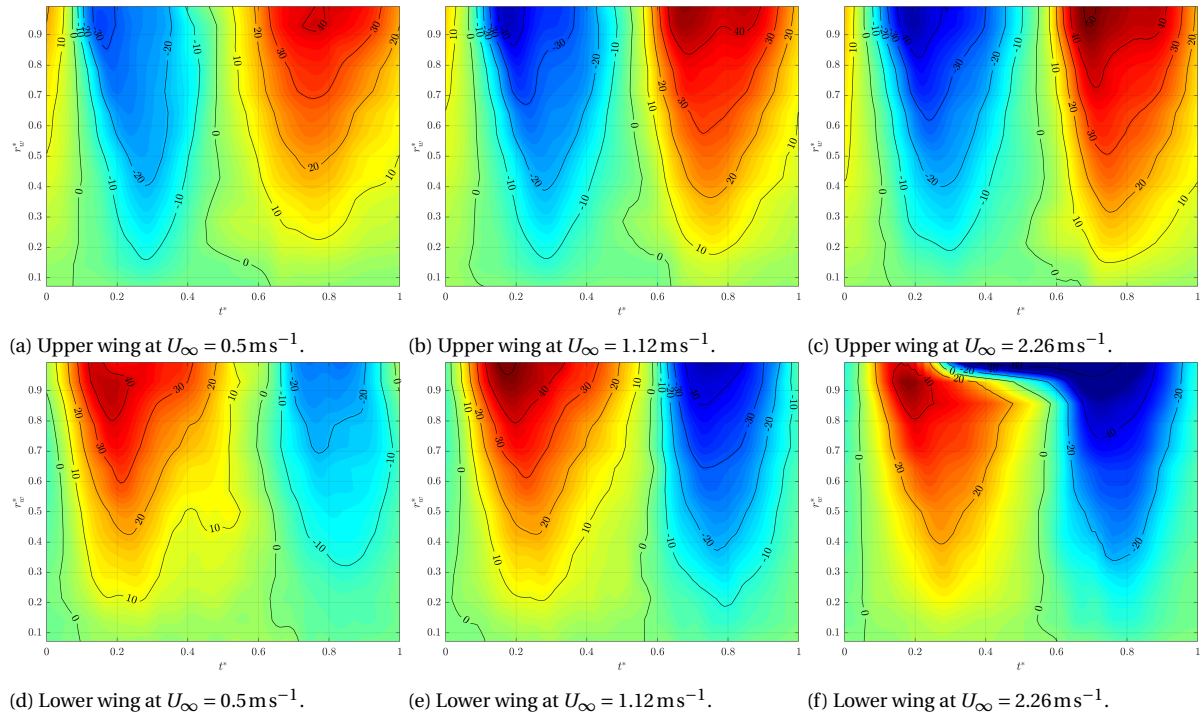
Figure A.11: Upper and lower wing incidence angle θ_w [°] over span and time due to different forward flight velocities.

(a) Upper wing at $U_\infty = 0.5\,\mathrm{m\,s^{-1}}$.   (b) Upper wing at $U_\infty = 1.12\,\mathrm{m\,s^{-1}}$.   (c) Upper wing at $U_\infty = 2.26\,\mathrm{m\,s^{-1}}$.

(d) Lower wing at $U_\infty = 0.5\,\mathrm{m\,s^{-1}}$.   (e) Lower wing at $U_\infty = 1.12\,\mathrm{m\,s^{-1}}$.   (f) Lower wing at $U_\infty = 2.26\,\mathrm{m\,s^{-1}}$.
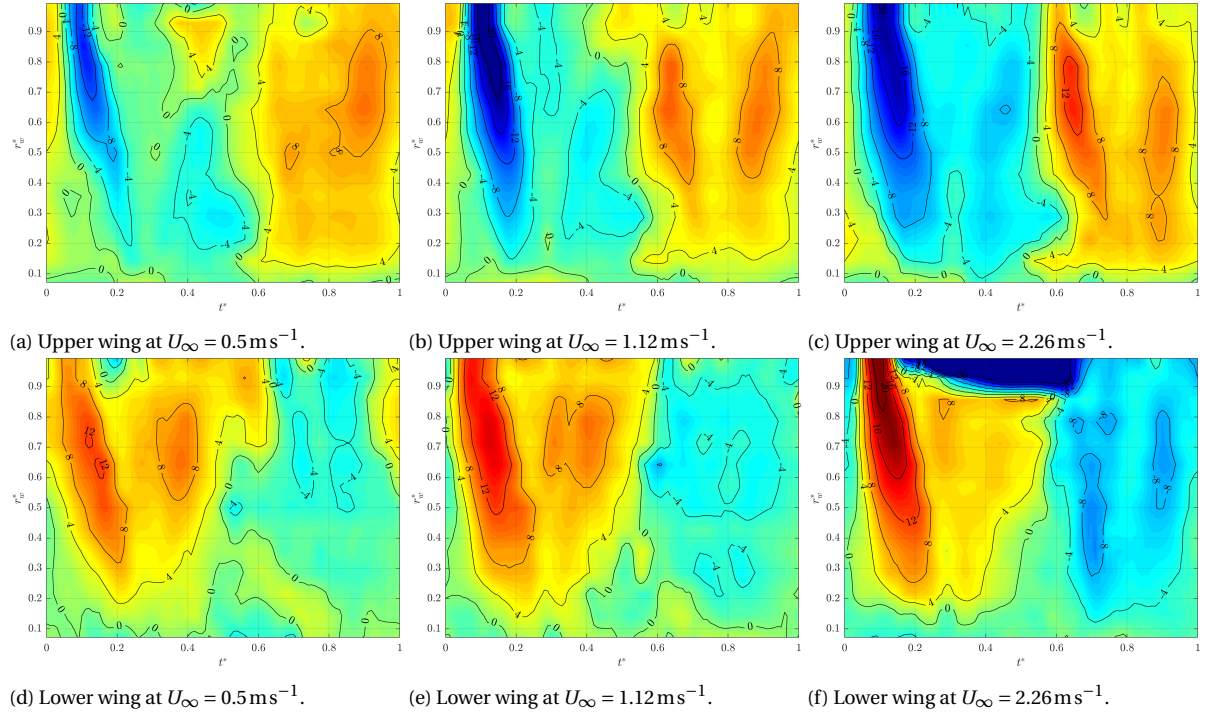
Figure A.12: Upper and lower wing camber ratio ε [%] over span and time due to different forward flight velocities.

(a) Upper wing at $U_\infty = 0.5\,\mathrm{m\,s^{-1}}$.   (b) Upper wing at $U_\infty = 1.12\,\mathrm{m\,s^{-1}}$.   (c) Upper wing at $U_\infty = 2.26\,\mathrm{m\,s^{-1}}$.

(d) Lower wing at $U_\infty = 0.5\,\mathrm{m\,s^{-1}}$.   (e) Lower wing at $U_\infty = 1.12\,\mathrm{m\,s^{-1}}$.   (f) Lower wing at $U_\infty = 2.26\,\mathrm{m\,s^{-1}}$.
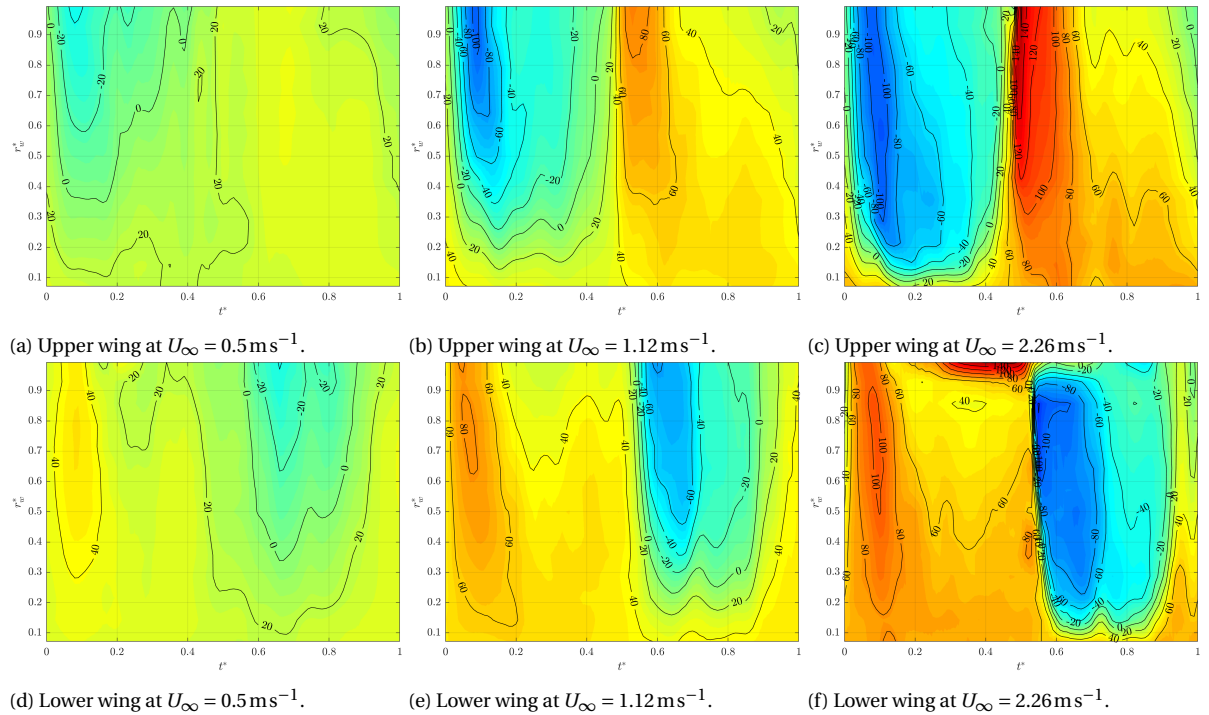
Figure A.13: Upper and lower wing angle of attack α [°] over span and time due to different forward flight velocities.

(a) Upper wing at $U_\infty = 0.5\,\mathrm{m\,s^{-1}}$.

(b) Upper wing at $U_\infty = 1.12\,\mathrm{m\,s^{-1}}$.

(c) Lower wing at $U_\infty = 2.26\,\mathrm{m\,s^{-1}}$.

(d) Lower wing at $U_\infty = 0.5\,\mathrm{m\,s^{-1}}$.

(e) Lower wing at $U_\infty = 1.12\,\mathrm{m\,s^{-1}}$.

(f) Lower wing at $U_\infty = 2.26\,\mathrm{m\,s^{-1}}$.
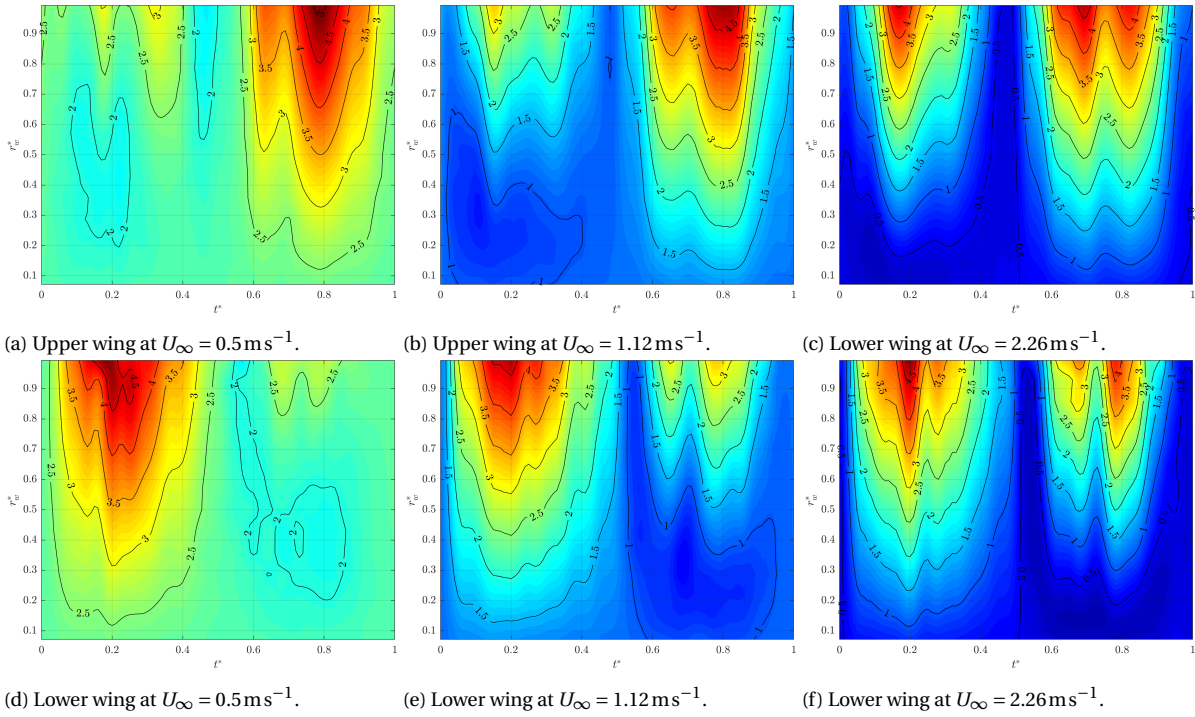
Figure A.14: Upper and lower wing inflow velocity magnitude $||U_{tot,w}||$ [$\mathrm{m\,s^{-1}}$] over span and time due to different forward flight velocities.

A.5. Descending flight
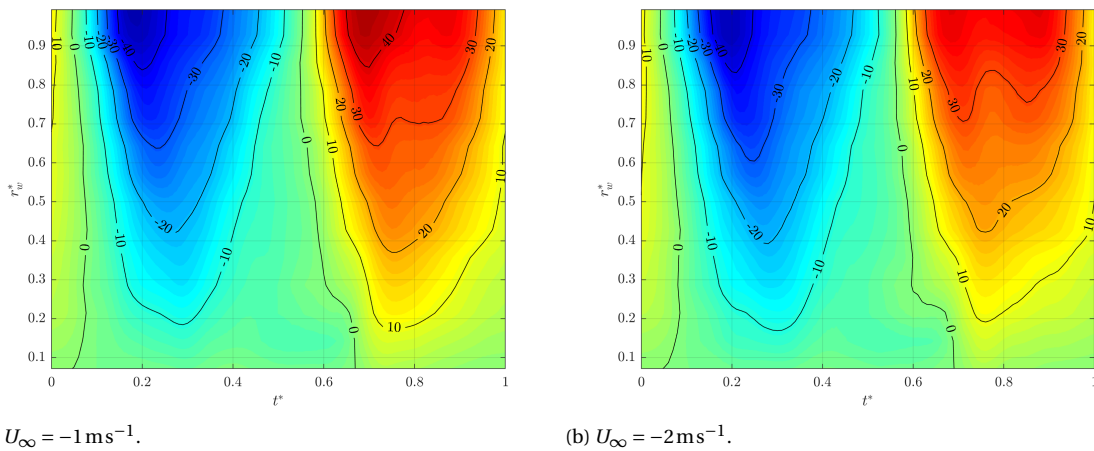
(a) $U_\infty = -1\,\mathrm{m\,s^{-1}}$.

(b) $U_\infty = -2\,\mathrm{m\,s^{-1}}$.

Figure A.15: Upper wing incidence angle θ_w [°] over span and time in hover due to different freestream velocities.
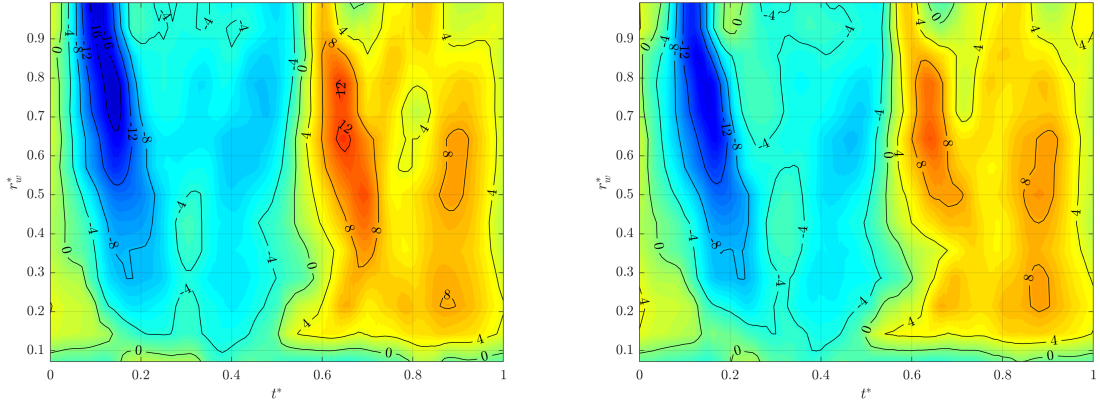
(a) $U_\infty = -1\,\mathrm{m\,s^{-1}}$.   (b) $U_\infty = -2\,\mathrm{m\,s^{-1}}$.

Figure A.16: Upper wing camber ratio ε [%] over span and time in hover due to different freestream velocities.
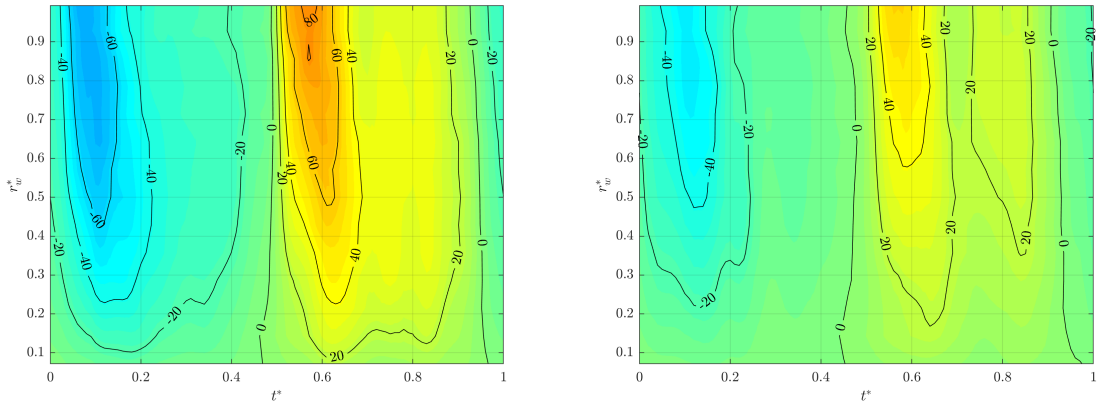
(a) $U_\infty = -1\,\mathrm{m\,s^{-1}}$.   (b) $U_\infty = -2\,\mathrm{m\,s^{-1}}$.

Figure A.17: Upper wing angle of attack α [°] over span and time due to different freestream velocities.
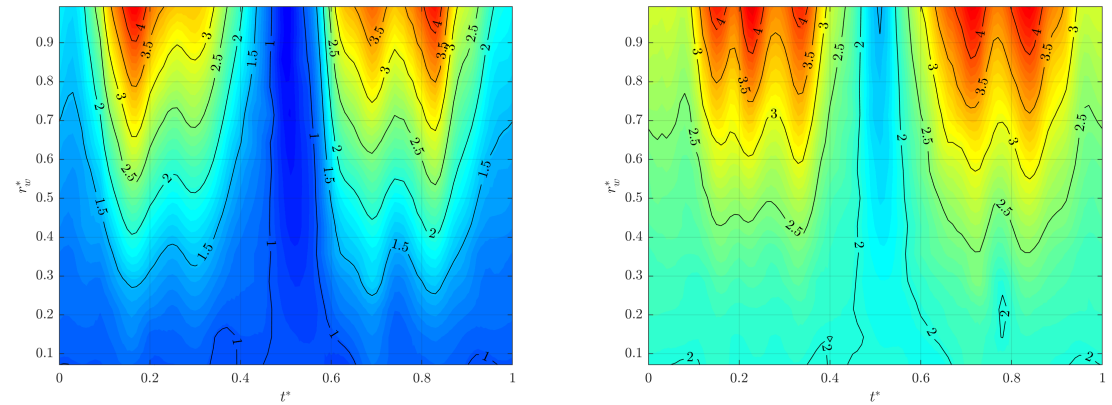
(a) $U_\infty = -1\,\mathrm{m\,s^{-1}}$.   (b) $U_\infty = -2\,\mathrm{m\,s^{-1}}$.

Figure A.18: Upper wing inflow velocity magnitude $||U_{tot,w}||$ [$\mathrm{m\,s^{-1}}$] over span and time due to different freestream velocities.

B
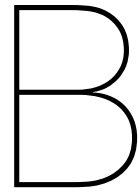
3D wing deformation

Video files of the DelFly wing deformation are embedded in the following pages. They can be played with a compatible PDF viewer using Adobe Flash Player. For the printed document four views at different phases are added.

B.1. Hovering flight
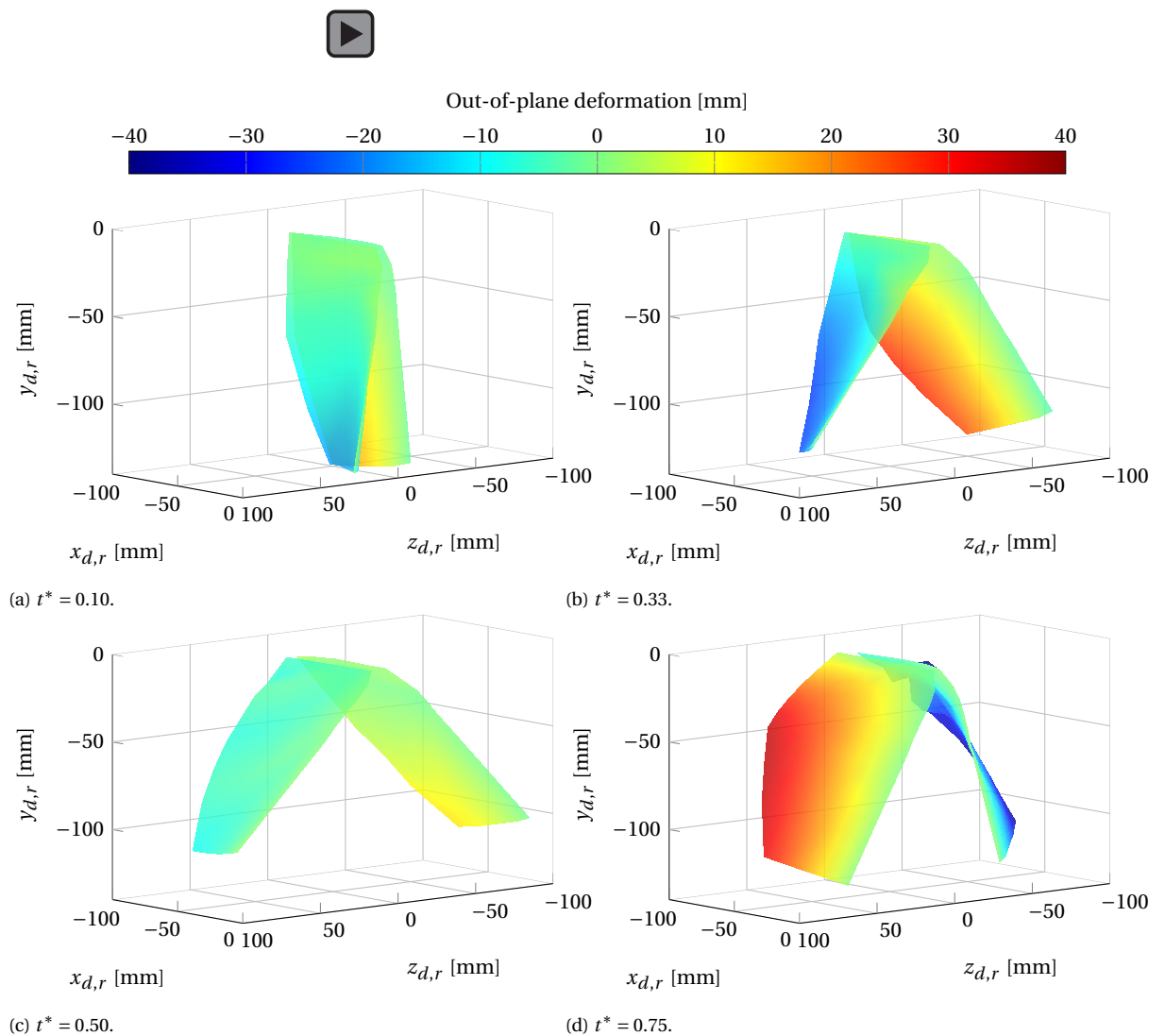
Figure B.1: 3D wing shape at hovering flight with $f = 12\,\mathrm{Hz}$. The coordinate system is aligned with the right wing dihedral angle, indicated by the subscript "$_{d,r}$". The upper wing is visible on the left. Some points near the root of the lower wing are incorrectly measured during the instroke.

B.2. Climbing flight
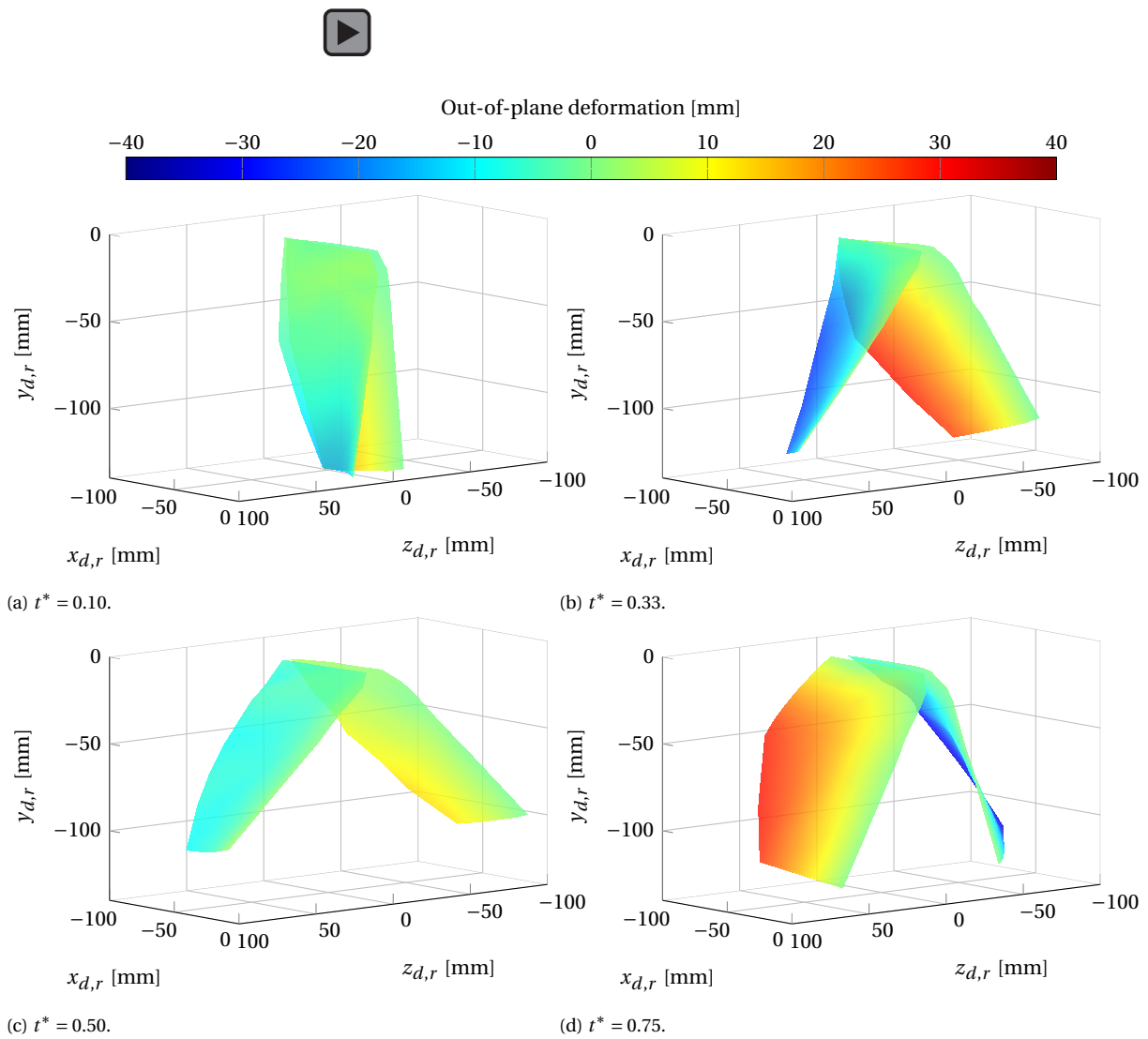
Figure B.2: 3D wing shape at $2\,\mathrm{m\,s^{-1}}$ climbing flight. The coordinate system is aligned with the right wing dihedral angle, indicated by the subscript "$_{d,r}$". The upper wing is visible on the left.

B.3. Forward flight

(a) $t^* = 0.10$.

(b) $t^* = 0.33$.

(c) $t^* = 0.50$.

(d) $t^* = 0.75$.
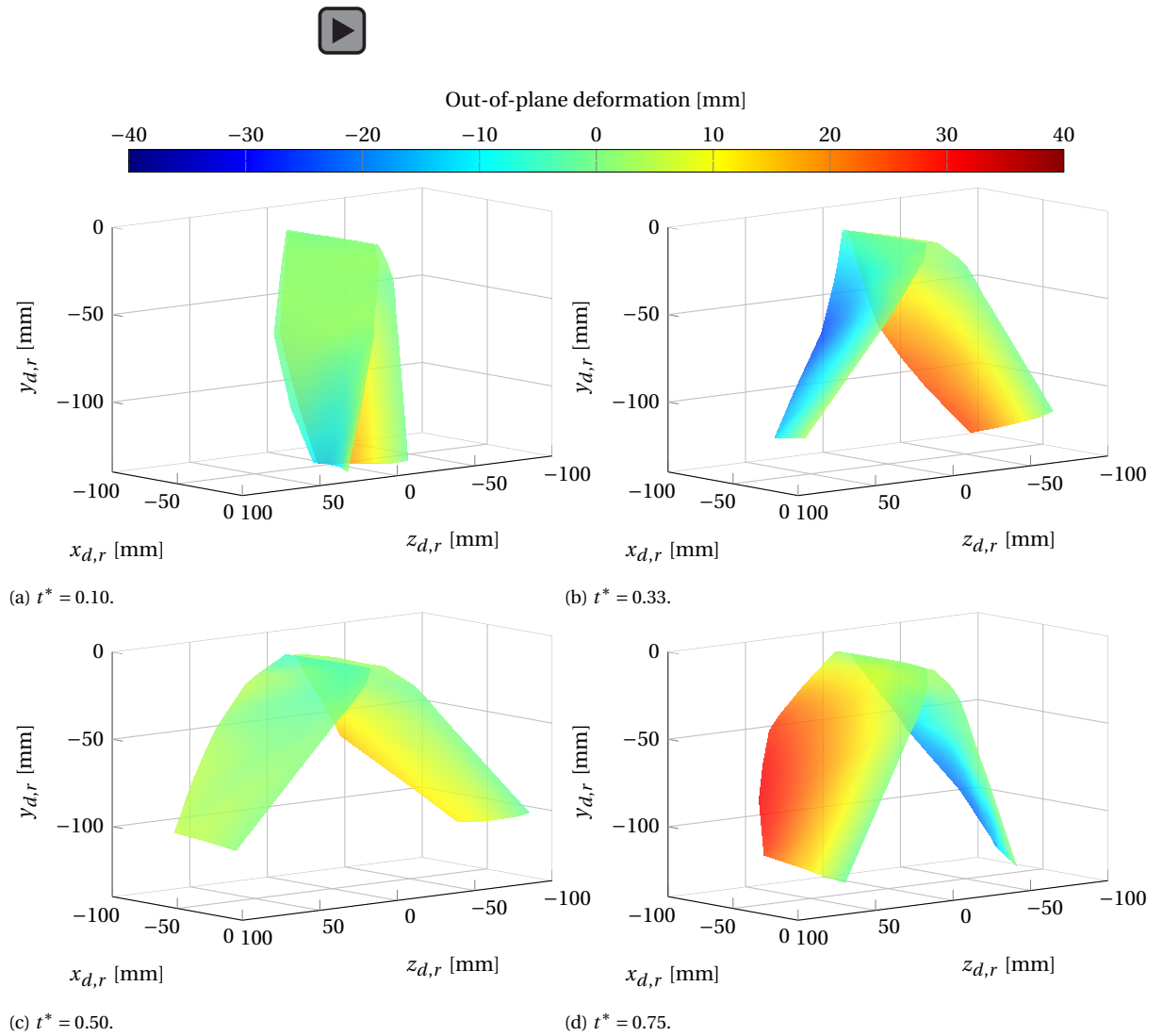
Figure B.3: 3D wing shape at $2.26\,\mathrm{m\,s^{-1}}$ forward flight. The coordinate system is aligned with the right wing dihedral angle, indicated by the subscript "$_{d,r}$". The upper wing is visible on the left.

Bibliography

[1] Y. Abdel-Aziz and H. M. Karara. Direct linear transformation from comparator coordinates into object space coordinates in close-range photogrammetry. *American Society of Photogrammetry Symposium on Close-Range Photogrammetry*, 433:1–18, 1971.

[2] D. D. Aguayo, F. Mendoza Santoyo, M. H. de La Torre-I, M. D. Salas-Araiza, C. Caloca-Mendez, and D. A. Gutierrez Hernandez. Insect wing deformation measurements using high speed digital holographic interferometry. *Optics Express*, 18(6):5661–5667, 2010.

[3] D. D. Aguayo, F. M. Santoyo, M. H. de La Torre-I, M. D. Salas-Araiza, and C. Caloca-Mendez. Comparison on different insects' wing displacements using high speed digital holographic interferometry. *Journal of biomedical optics*, 16(6):066005, 2011.

[4] R. Albertani. *Experimental aerodynamic and elastic deformation characterization of low aspect ratio flexible fixed wings applied to micro aerial vehicles*. PhD thesis, University of Florida, Florida, 2005.

[5] R. Albertani, B. Stanford, J. P. Hubner, and P. G. Ifju. Aerodynamic coefficients and deformation measurements on flexible micro air vehicle wings. *Experimental Mechanics*, 47(5):625–635, 2007.

[6] D. C. Brown. Close range camera calibration. *Photogrammetric Engineering*, 37(8):855–866, 1971.

[7] A. W. Burner, W. L. Snow, and W. K. Goad. Model deformation measurements at a cryogenic wind tunnel using photogrammetry. *Proceedings (A86-38051 17-35)*, 1985.

[8] P. Cheng, J. Hu, G. Zhang, L. Hou, B. Xu, and X. Wu. Deformation measurements of dragonfly's wings in free flight by using windowed fourier transform. *Optics and Lasers in Engineering*, 46 (2):157–161, 2008.

[9] D. Coleman, K. Gakhar, M. Benedict, J. Tran, and J. Siroh. Aeromechanics analysis of a hummingbird-like flapping wing in hover. *Journal of Aircraft*, 180(21):1–16, 2018.

[10] S. A. Combes and T. L. Daniel. Into thin air: Contributions of aerodynamic and inertial-elastic forces to wing bending in the hawkmoth manduca sexta. *J. Exp. Biol*, 206(Pt 17):2999–3006, 2003.

[11] D. Curtis, M. Reeder, C. Svanberg, and R. Cobb. Flapping wing micro air vehicle bench test set-up. *47th AIAA Aerospace Sciences Meeting Including The New Horizons Forum and Aerospace Exposition*, 2009.

[12] G. de Croon, M. Perçin, B. Remes, R. Ruijsink, and C. de Wagter. *The DelFly: Design, Aerodynamics, and Artificial Intelligence of a Flapping Wing Robot*. Springer Netherlands, Dordrecht, 2016.

[13] M. E. Deetjen, A. A. Biewener, and D. Lentink. High-speed surface reconstruction of a flying bird using structured light. *The Journal of experimental biology*, 220(Pt 11):1956–1961, 2017.

93

[14] A. del Estal Herrero, M. Percin, M. Karasek, and B. van Oudheusden. Flow visualization around a flapping-wing micro air vehicle in free flight using large-scale piv. *Aerospace*, 5(4):99, 2018.

[15] S. Deng. *Aerodynamics of Flapping-wing Micro-Air-Vehicle.* PhD thesis, Technische Universiteit Delft, Delft, 2016.

[16] G. Du and M. Sun. Effects of wing deformation on aerodynamic forces in hovering hoverflies. *The Journal of experimental biology*, 213(Pt 13):2273–2283, 2010.

[17] C. P. Ellington. The aerodynamics of hovering insect flight. iii. kinematics. *Philosophical Transactions of the Royal Society B: Biological Sciences*, 305(1122):41–78, 1984.

[18] G. A. Fleming, S. M. Bartram, M. R. Waszak, and L. N. Jenkins. Projection moire interferometry measurements of micro air vehicle wings. *Proc. of SPIE*, 4448:90, 2001.

[19] Y. Gong and S. Zhang. Ultrafast 3-d shape measurement with an off-the-shelf dlp projector. *Optics Express*, 18(19):19743–19754, 2010.

[20] P. Gopalakrishnan and D. K. Tafti. Effect of wing flexibility on lift and thrust production in flapping flight. *AIAA Journal*, 48(5):865–877, 2010.

[21] Groen, Mark and Bruggeman, Bart and Remes, Bart and Ruijsink, Rick and Van Oudheusden, BW and Bijl, Hester. Microsoft word - paper imav 2010 - delfly v5.doc. *Int. Micro Air Vehicle Conf. and Competition*, 2010.

[22] N. S. Ha, T. Jin, and N. S. Goo. Modal analysis of an artificial wing mimicking an allomyrina dichotoma beetle's hind wing for flapping-wing micro air vehicles by noncontact measurement techniques. *Optics and Lasers in Engineering*, 51(5):560–570, 2013.

[23] R. Hartley and A. Zisserman. *Multiple view geometry in computer vision.* Cambridge University Press, Cambridge UK and New York, 2nd ed. edition, 2004.

[24] R. Horaud, M. Hansard, G. Evangelidis, and C. Ménier. An overview of depth cameras and range scanners based on time-of-flight technologies. *Machine Vision and Applications*, 27(7): 1005–1020, 2016.

[25] M. Jensen. Biology and physics of locust flight. iii. the aerodynamics of locust flight. *Philosophical Transactions of the Royal Society B: Biological Sciences*, 239(667), 1956.

[26] M. Karasek, A. J. Koopmans, S. F. Armanini, B. D. Remes, and G. C. de Croon. Free flight force estimation of a 23.5 g flapping wing mav using an on-board imu. *Proceedings of the 2016 IEEE/RSJ International Conference on Intelligent Robots and Systems (IROS)*, pages 4963–4969, 2016.

[27] M. Karásek, F. T. Muijres, C. de Wagter, B. D. W. Remes, and G. C. H. E. de Croon. A tailless aerial robotic flapper reveals that flies use torque coupling in rapid banked turns. *Science (New York, N.Y.)*, 361(6407):1089–1094, 2018.

[28] C. Koehler, Z. Liang, Z. Gaston, H. Wan, and H. Dong. 3d reconstruction and analysis of wing deformation in free-flying dragonflies. *The Journal of experimental biology*, 215(Pt 17):3018–3027, 2012.

[29] B. Li and S. Zhang. Superfast high-resolution absolute 3d recovery of a stabilized flapping flight process. *Optics Express*, 25(22):27270–27282, 2017.

[30] B. Li, N. Karpinsky, and S. Zhang. Novel calibration method for structured-light system with an out-of-focus projector. *Applied optics*, 53(16):3415–3426, 2014.

[31] J. Li, X. Su, and L. Guo. Improved fourier transform profilometry for the automatic measurement of 3d object shapes. *Optical Engineering*, 29(12):1439, 1990.

[32] B. Martínez Gallar. Flapping-wing aerodynamics study on the wake of delfly ii: by means of robotic volumetric particle tracking velocimety. Master's thesis, Technische Universiteit Delft, Delft, 2019.

[33] W. Nachtigall. ie kinematik der schlagflügelbewegungen von dipteren: Methodische und analytische grundlagen zur biophysik des insektenflugs. *Zeitschrift fiir vergleichende Physiologie*, 52:155–211, 1966.

[34] T. Nakata, H. Liu, Y. Tanaka, N. Nishihashi, X. Wang, and A. Sato. Aerodynamics of a bio-inspired flexible flapping-wing micro air vehicle. *Bioinspiration & Biomimetics*, 6(4):045002, 2011.

[35] G. Pedrini, W. Osten, and M. E. Gusev. High-speed digital holographic interferometry for vibration measurement. *Applied Optics*, 45(15):3456, 2006.

[36] M. Perçin. *Aerodynamic Mechanisms of Flapping Flight*. PhD thesis, Technische Universiteit Delft, Delft, 2015.

[37] M. Perçin, B. W. van Oudheusden, G. C. H. E. de Croon, and B. Remes. Force generation and wing deformation characteristics of a flapping-wing micro air vehicle 'delfly ii' in hovering flight. *Bioinspiration & Biomimetics*, 11(3):036014, 2016.

[38] F. Scarano. Tomographic piv: principles and practice. *Measurement Science and Technology*, 24(1):012001, 2013.

[39] D. Schanz, S. Gesemann, and A. Schröder. Shake-the-box: Lagrangian particle tracking at high particle image densities. *Experiments in Fluids*, 2016.

[40] H. Schreier and Orteu, Jean-José: Sutton, Michael A. *Image Correlation for Shape, Motion and Deformation Measurements*. Springer US, Boston, MA, 2009.

[41] D. Song, H. Wang, L. Zeng, and C. Yin. Measuring the camber deformation of a dragonfly wing using projected comb fringe. *Review of Scientific Instruments*, 72(5):2450–2454, 2001.

[42] B. Stanford, P. Ifju, R. Albertani, and W. Shyy. Fixed membrane wings for micro air vehicles: Experimental characterization, numerical modeling, and tailoring. *Progress in Aerospace Sciences*, 44(4):258–294, 2008.

[43] K. Stewart and R. Albertani. Experimental elastic deformation characterization of a flapping-wing mav using visual image correlation. *Critical Technology Development for Micro Munition Vehicles*, 2007.

[44] X. Su and W. Chen. Reliability-guided phase unwrapping algorithm: a review. *Optics and Lasers in Engineering*, 42(3):245–261, 2004.

[45] M. A. Sutton, W. J. Wolters, W. H. Peters, W. F. Ranson, and McNeill. Determination of displacements using an improved digital correlation method. *Image and Vision Computing*, 1(3): 133–139, 1983.

[46] M. Takeda and K. Mutoh. Fourier transform profilometry for the automatic measurement of 3-d object shapes. *Applied Optics*, 22(24):3977, 1983.

[47] S. M. Walker, A. L. R. Thomas, and G. K. Taylor. Photogrammetric reconstruction of high-resolution surface topographies and deformable wing kinematics of tethered locusts and free-flying hoverflies. *J. R. Soc. Interface*, 6:351–366, 2009.

[48] S. M. Walker, A. L. R. Thomas, and G. K. Taylor. Deformable wing kinematics in free-flying hoverflies. *Journal of the Royal Society, Interface*, 7(42):131–142, 2010.

[49] I. D. Wallace, N. J. Lawson, A. R. Harvey, J. D. C. Jones, and A. J. Moore. High-speed photogrammetry system for measuring the kinematics of insect wings. *Applied optics*, 45(17):4165–4173, 2006.

[50] H. Wang. Measuring wing kinematics, flight trajectory and body attitude during forward flight and turning maneuvers in dragonflies. *Journal of Aircraft*, 206(4):745–757, 2003.

[51] H. Wang, L. Zeng, and C. Yin. Measuring the body position, attitude and wing deformation of a free-flight dragonfly by combining a comb fringe pattern with sign points on the wing. *Meas. Sci. Technol.*, 13:903–908, 2002.

[52] T. Weis-Fogh. Quick estimates of flight fitness in hovering animals, including novel mechanisms for lift production. *J. Exp. Biol*, 59:169–230, 1973.

[53] A. P. Willmott and C. P. Ellington. The mechanics of flight in the hawkmoth manduca sexta. i. kinematics of hovering and forward flight. *J. Exp. Biol*, 200:2727–2738, 1997.

[54] T. Wolf and R. Konrath. Avian wing geometry and kinematics of a free-flying barn owl in flapping flight. *Experiments in Fluids*, 56(28), 2015.

[55] G.-h. Wu, L.-j. Zeng, and L.-h. Ji. Measuring the wing kinematics of a moth (helicoverpa armigera) by a two-dimensional fringe projection method. *Journal of Bionic Engineering*, 5 (9):138–142, 2008.

[56] P. Wu, B. Stanford, W. Bowman, A. Schwartz, and P. Ifju. Digital image correlation techniques for full–field displacement measurements of micro air vehicle flapping wings. *Experimental Techniques*, 3:53–58, 2009.

[57] P. Wu, P. Ifju, and B. Stanford. Flapping wing structural deformation and thrust correlation study with flexible membrane wings. *AIAA Journal*, 48(9):2111–2122, 2010.

[58] L.-J. Yang, F.-Y. Hsiao, W.-T. Tang, and I.-C. Huang. 3d flapping trajectory of a micro-air-vehicle and its application to unsteady flow simulation. *International Journal of Advanced Robotic Systems*, 10(6):264, 2013.

[59] Yoshizawa, editor. *Handbook of optical metrology: Principles and Applications.* Taylor & Francis Group, LLC., Boca Raton, 2009.

[60] J. Young, S. M. Walker, R. J. Bomphrey, G. K. Taylor, and A. L. R. Thomas. Details of insect wing design and deformation enhance aerodynamic function and flight efficiency. *Science (New York, N.Y.)*, 325(5947):1549–1552, 2009.

[61] H. K. Yuen, J. Princen, J. Illingworth, and J. Kittler. Comparative study of hough transform methods for circle finding. *Image and Vision Computing*, 8(1):71–77, 1990.

[62] W. Zarnack. *Kinematik der Flügelschlagbewegungen bei Locusta migratoria L.* PhD thesis, Ludwig Maximilians Universität, Munich, 1969.

[63] L. Zeng, H. Matsumoto, and K. Kawachi. A fringe shadow method for measuring flapping angle and torsional angle of a dragonfly wing. *Meas. Sci. Technol.*, 7(5):776–781, 1996.

[64] Q. Zhang, L. Huang, Y.-W. Chin, L.-G. Keong, and A. Asundi. 4d metrology of flapping-wing micro air vehicle based on fringe projection. *Proc. of SPIE*, page 87692Y, 2013.